Gyrotron Mode Converter Mirror Shaping Based on Phase Retrieval from Intensity Measurements

by

Douglas Robert Denison

B.S.E.E., The University of Alabama (1992)
M.S.E.E., The University of Alabama (1994)

Submitted to the
Department of Electrical Engineering and Computer Science
in partial fulfillment of the requirements for the degree of

Doctor of Philosophy

at the

MASSACHUSETTS INSTITUTE OF TECHNOLOGY

June 1999

Signature of Author .....
Department of Electrical Engineering and Computer Science
April 28, 1999

Certified by .....
Richard J. Temkin
Senior Scientist, Physics Department
Thesis Supervisor

Accepted by .....
Arthur C. Smith
Chairman, Department Committee on Graduate Students

Gyrotron Mode Converter Mirror Shaping Based on Phase Retrieval from Intensity Measurements

by

Douglas Robert Denison

Submitted to the Department of Electrical Engineering and Computer Science
on April 28, 1999, in partial fulfillment of the
requirements for the degree of
Doctor of Philosophy

Abstract

We present a new approach to designing mirrors (or reflectors) for microwave transmission lines based on phase retrieval from intensity measurements of the feed field. By incorporating measured field patterns of a wave in the design process, we can account for an actual field structure that may not be accurately represented by analytic expressions or numerical computations. The formulation of phase retrieval from intensity measurements of a linearly-polarized (scalar), paraxial wave is given, and the method is extended to shaping mirrors as phase-correcting surfaces. Experimental results for two gyrotron mode converters are then presented to validate the proposed design approach. In the first experiment, a pair of mirrors were shaped from infrared camera measurements of the asymmetric microwave beam radiated by a 1 MW, 110 GHz gyrotron. The mirrors were designed to transform the gyrotron radiation into a fundamental Gaussian beam with a uniform phase and 99.6% beam power transmission at the 3.175-cm aperture of a waveguide. Measurements of the final beam show that the mirror design method accurately produces a Gaussian beam with the desired phase, and 96.5% of the beam power is incident on the waveguide aperture. A pair of mirrors were designed for a gyrotron internal mode converter in the second experiment. The mode converter transforms the $TE_{22,6}$ circular waveguide mode of a gyrotron cavity into a free space beam; a pair of mirrors in a four-mirror mode converter were shaped to produce a 1.52-cm-waist Gaussian beam at the 5-cm aperture of a diamond gyrotron window to provide 99.6% beam transmission. Low- and high-power testing of the mirrors show that the design produces a high-quality Gaussian beam in both amplitude and phase, with a waist size along the gyrotron axis of 1.6 cm and a transverse waist of 1.7 cm at the window. This waist size provides 98.5% beam power transmission efficiency through the window aperture. Our successful experimental results demonstrate the efficacy of the proposed method, and encourage application to other areas such as reflector antennas, radio astronomy, free-space transmission lines, and waveguide mirrors and miter bends.

Thesis Supervisor: Richard J. Temkin
Title: Senior Scientist, Physics Department

Acknowledgements

Many people made significant contributions to the work presented in this thesis.

Dr. Richard Temkin initially invited me to join his group at MIT and subsequently guided my work on an interesting and fulfilling project with just the right (in my opinion) proportions of theory, computation, and experiment.

Present and past members of the gyrotron group, including Drs. Ken Kreischer, Bruce Danly, Jean-Philippe Hogge, Marco Pedrozzi, Takuji Kimura, Wen Hu, and fellow students Rahul Advani and George Haldeman provided many helpful discussions. Dr. Michael Shapiro lent his insights into the phase retrieval problem and proved to be a steadfast beta tester for all the computer code written in the course of this research. Dr. Monica Blank performed much of the original mode converter design and supplied the numerical routines used to benchmark the algorithms developed as part of this work.

The experimental results reported here would not have been possible without the extensive help of colleagues in the gyrotron community. Drs. Sam Chu, Kevin Felch, and Steve Cauffman of Communications and Power Industries were responsible for machining three sets of mode converter mirrors and for providing the low-power test facilities. Prof. Ron Vernon and Brent Harper at the University of Wisconsin supplied the low-power receivers used in several sets of measurements. Dr. John Lohr and the electron cyclotron heating research staff at General Atomics performed the high-power infrared camera measurements.

Profs. Hermann Haus and Peter Hagelstein served as both my area exam committee and thesis readers.

Much moral support and occasional proding came from friends Chad and Miranda. My parents and brother have been a constant source of encouragement.

> *To attain knowledge, add things everyday. To attain wisdom, remove things every day.*
>
> — *Lao-tse, Tao Te Ching*

Contents

List of Figures

List of Tables

Chapter 1

Introduction

This thesis develops a general approach to designing mirrors (or reflectors) for microwave transmission lines based on phase retrieval from intensity measurements of the feed field. By using the measured field patterns of a wave in the design process, we can account for an actual field structure that may not be accurately represented by analytic expressions or numerical computations. Although our formulation of the design method is general and applicable to a wide class of microwave and antenna engineering problems, our motivation and subsequent experimental results are based on studies of gyrotron mode converters.

In this chapter, we give a brief introduction to gyrotrons, with an emphasis on their electrodynamic properties. We discuss the internal mode converter, which is used to couple the high-order gyrotron cavity mode to free space. We present the motivation for our mirror shaping approach based on phase retrieval from intensity measurements in the context of internal mode converter research. The specific steps of the mirror design approach are then outlined, and we note the similarities of this design problem to shaping reflectors in off-set fed, dual-reflector antennas. The chapter concludes with an outline of the remainder of the thesis.

1.1 Background

Gyrotron oscillators are efficient, fast wave, electron beam devices capable of providing megawatt power levels of electromagnetic energy in the micro- and millimeter-wave spectrum. For high-power wave generation, they bridge the frequency gap between conventional slow wave devices and lasers. Applications of gyrotrons span the range from basic science to industry, including nuclear magnetic resonance studies, RF drivers for particle accelerators, materials processing, plasma diagnostics, and

high-power, high-frequency radar. However, the primary impetus behind the development of these high-power sources has been electron cyclotron (EC) heating of plasmas in magnetic confinement fusion devices. Current demands for EC heating call for hundreds of kilowatts of electromagnetic energy in the 100 GHz range. Future fusion devices will require tens of megawatts of power at frequencies up to 170 GHz.

The gyrotron produces coherent electromagnetic radiation via the transfer of energy from an electron beam to an electromagnetic wave. An annular electron beam is emitted by a magnetron injection gun and is subsequently guided through a vacuum tube along externally-applied magnetic field lines, as shown schematically in Figure 1-1. The magnetic field also compresses the beam, thus increasing the perpendicular velocity component of the electrons. The beam enters an open-ended cavity where the perpendicular momentum of the electrons is coupled to a resonant transverse electric (TE) mode of the cavity. The annular electron beam can be considered as a current source that excites a cavity mode, and for this circular distribution of current whose radius is on the order of the cavity radius, the excited mode has a high azimuthal index. Additionally, the radius of the cavity is large compared to a wavelength and leads to a highly-over-moded structure. In contrast to conventional wave-beam devices where the interaction region has transverse dimensions on the order of a wavelength, the large, over-moded cavity in the gyrotron permits high-power operation at millimeter wavelengths without electric breakdown or thermal overload.

After the electron beam exits the cavity, it diverges and eventually impinges on the collector. The high-order electromagnetic cavity mode must be transformed into a wave that is suitable for free-space propagation. The various constraints imposed by the gyrotron and the electromagnetic wave — the presence of the electron beam, the physical size of the tube, the high field intensity, and the large modal indices — preclude the use of traditional mode transformers such as gradual tapers or stepped waveguide. An early alternative was proposed by Vlasov *et al.* [1], who used a geometrical optics argument to form a helical cut in a circular waveguide, or launcher, that would radiate the high-order mode as a bundle of rays. For the TE_{mn} circular waveguide mode (with m the azimuthal index and n the radial index), geometrical optics gives a divergence angle 2α of this beam with

$$\alpha = \cos^{-1}\left(\frac{m}{\nu_{mn}}\right), \tag{1.1}$$

and ν_{mn} the n^{th} zero of $J'_m(x)$. This radiated beam is then shaped by one or more focusing mirrors. A diagram of the Vlasov launcher and single focusing mirror is

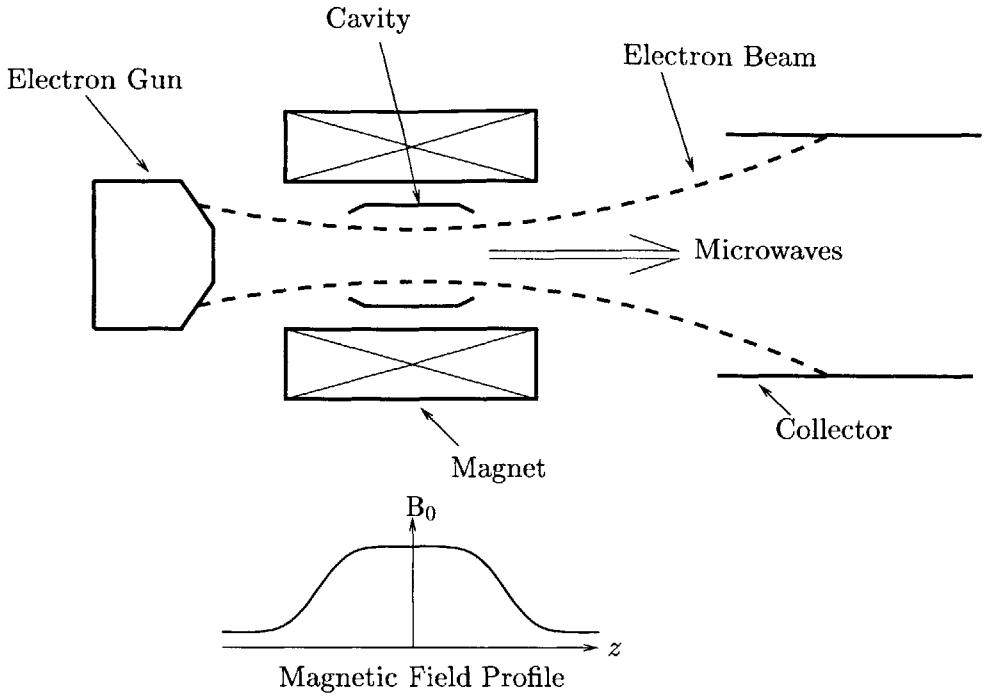

Figure 1-1: Geometry of a basic gyrotron.

shown in Figure 1-2.

For large m and $n \sim 1$, the ratio m/ν_{mn} is close to unity (see [2] for the asymptotic forms of the Bessel function zeros), and we see from expression (1.1) that in this case α is small. However, TE modes with $m, n \gg 1$ reduce the ohmic heating on the wall of the cavity and permit higher power generation in the gyrotron, and for these modes the Vlasov launcher divergence angle is prohibitively large. To circumvent this difficulty, Denisov *et al.* [3] developed a rippled-wall launcher that uses smooth perturbations on the inner wall of a circular waveguide to couple power from the main cavity mode into satellite modes. The satellite modes then beat with the main mode

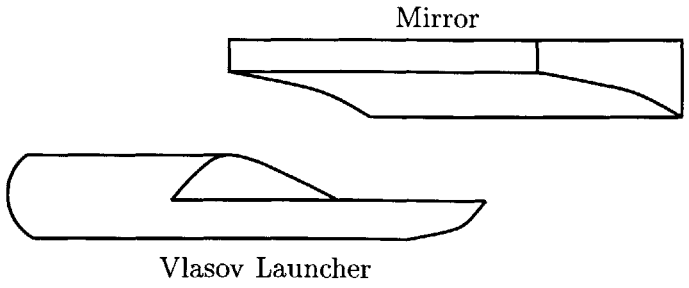

Figure 1-2: Vlasov launcher and single mirror.

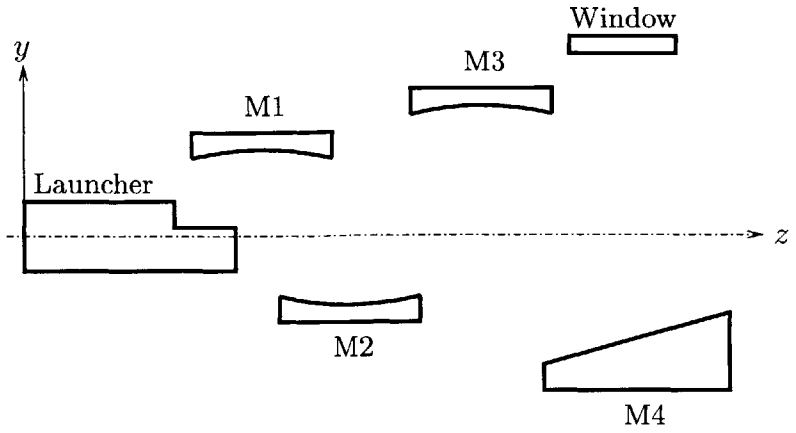

Figure 1-3: Schematic diagram of a gyrotron internal mode converter with a rippled-wall launcher and four mirrors.

to produce Gaussian-like current bundles on the inner wall of the launcher. As the wave propagates down the launcher, these current distributions become increasingly distinct. Near the end of the launcher, each compact Gaussian current distribution behaves essentially as an independent radiator. A step cut in the waveguide wall permits radiation of a Gaussian-like beam from a current bundle into free space. This beam is then focussed and guided along the length of the gyrotron tube by a set of mirrors that also serve to direct the electromagnetic energy through a vacuum window. An internal gyrotron mode converter consisting of a rippled-wall launcher with a step-cut aperture and four mirrors is shown in Figure 1-3.

The last element of the microwave transmission line in the gyrotron is the gyrotron vacuum window. The microwave beam must be matched at the free space/dielectric interface of the window to minimize reflections, and it must have a suitable power distribution over the aperture to accommodate the window's power handling capabilities. For gyrotrons operating at low average power, a passively-cooled window made of a low loss material such as quartz is adequate. For long-pulse, high-power gyrotrons, an actively-cooled window is necessary. Typical window configurations include the face-cooled double-disk (Figure 1-4(a)) and edge-cooled single-disk (Figure 1-4(b)) designs. Figure 1-5 shows the arrangement of the internal mode converter and window in a high-power gyrotron; the height of the gyrotron is approximately 2 m.

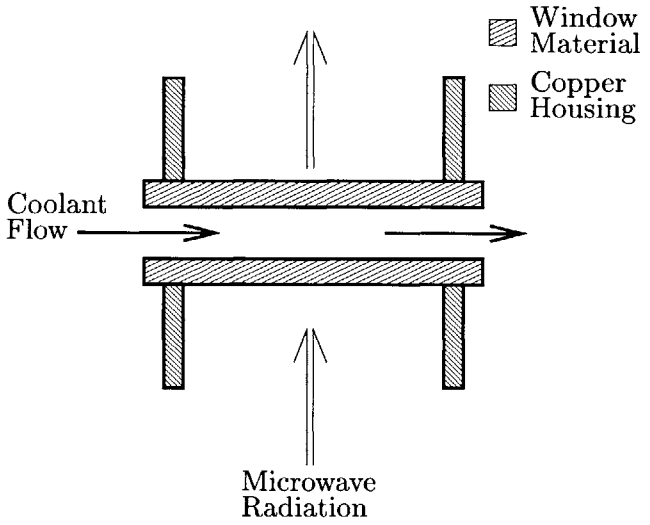

(a) Double-disk, face-cooled window.

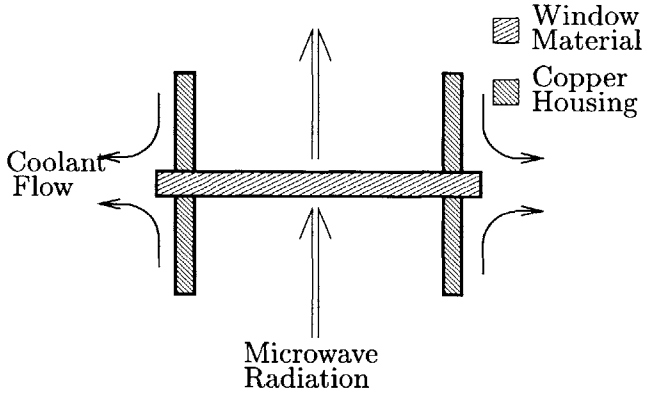

(b) Single-disk, edge-cooled window.

Figure 1-4: Two high-power gyrotron window configurations: the double-disk, face-cooled window and the single-disk, edge-cooled window.

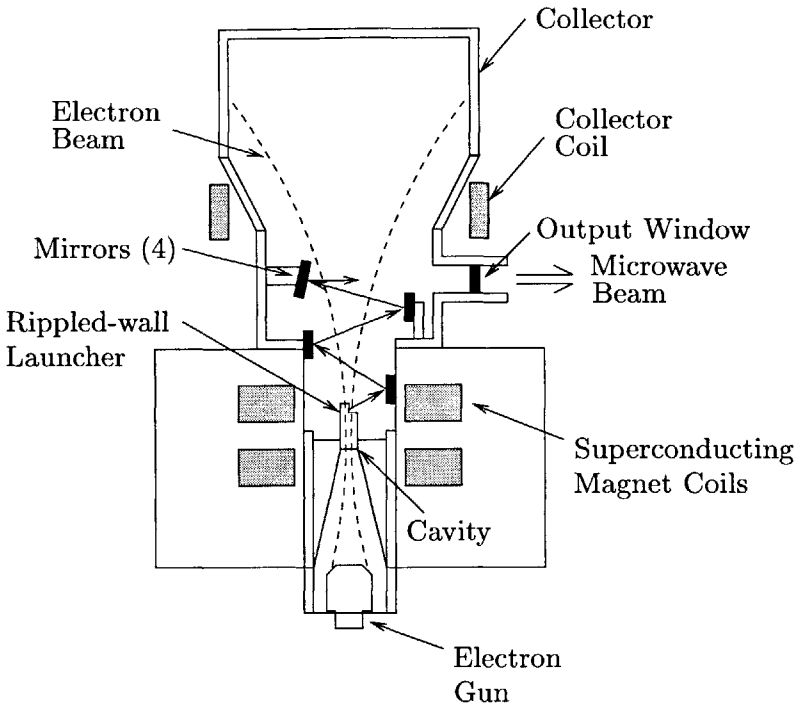

Figure 1-5: Schematic diagram of a typical high-power gyrotron with an internal mode converter. The height of the gyrotron is approximately 2 m.

1.2 Motivation

In the previous section, we mentioned that internal mode converters not only transform the high-order gyrotron cavity mode into a low-order free-space mode, but they also shape the beam for efficient transmission through the gyrotron output window. This is a critical function of mode converters because for the power levels of microwave radiation produced by high-power ($\sim$ 1 MW) gyrotrons (Figure 1-5), the electric field intensity profile over the window aperture proves to be the limiting factor in the overall power handling capability of the gyrotron for long-pulse and CW operation. The microwave beam shape on the window is constrained by the thermal characteristics of the window material and cooling configuration, as well as by edge diffraction losses at the window aperture. The internal mode converter mirrors must be shaped to provide a field profile at the window that accommodates the thermal properties of the window material and minimizes edge losses.

Past mode converter mirror designs have relied on numerical simulations of the fields radiated by the launcher. For instance, the rippled-wall launcher can be modeled using coupled mode theory, which leads to a set of simultaneous differential equations that are solved numerically for the fields inside the guide [4]. The radiated field,

computed from a vector diffraction integral, behaves as a quasi-Gaussian beam that can be focussed into a nearly-ideal Gaussian beam at the window by using doubly-curved mirrors designed from analytic expressions [4, 5]. For more complicated final beam shapes, such as a flat power profile over the window aperture, mirror synthesis methods that incorporate the simulated launcher fields in the mirror shaping are used [6]. Experimental results have demonstrated, however, that the field intensity on the gyrotron window often does not agree with the design profile [7]. This deviation from design results in a lower power handling capability of the window, limiting the overall performance of the gyrotron.

For example, consider a 110 GHz gyrotron internal mode converter that uses a rippled-wall launcher and four mirrors (Figure 1-3) to transform the $TE_{22,6}$ cylindrical mode into a flat-top beam at a 10-cm-diameter double-disk sapphire window (see Figure 1-4(a)). The theoretically-predicted field intensity profile at the plane of the window is shown in Figure 1-6. In the figure, the z-axis origin is at the beginning of the launcher, as depicted in Figure 1-3, and the window is centered at $x = 0$ cm, $z =$ 37.4 cm. The power is distributed uniformly over the bulk of the window, with slightly higher power deposition near the circumference of the window to take advantage of the window's thermal properties. We can quantify the power loading on the window by defining a peaking factor as the ratio of the peak intensity to the average intensity over the aperture. For the case of uniform power distribution the peaking factor would be 1; in this application the higher intensity near the circumference of the aperture raises the peaking factor to 2.

Cold-test (or low-power) measurements of this mode converter show that the actual intensity profile produced at the window aperture is not the desired uniform distribution, but rather has a region of high intensity that encircles the center of the aperture as a crescent-shaped profile (Figure 1-7). These cold test measurements agree with the high-power results reported in [7]. The peaking factor for this beam rises to 2.6 because of the high-intensity region, and we see that this uneven loading on the gyrotron window will necessarily limit its power-handling capabilities.

To understand the source of this discrepancy between theory and measurement, the field profiles at several positions inside the mode converter were measured in cold test. Figure 1-8 shows the theoretically-predicted field intensity at the plane of the third mirror surface (M3 in Figure 1-3), while Figure 1-9 gives the measured field intensity over the same plane. Although the two patterns are similar, there are significant differences in the size and shape of the individual intensity contours that ultimately result in the observed differences between theoretical and experimental

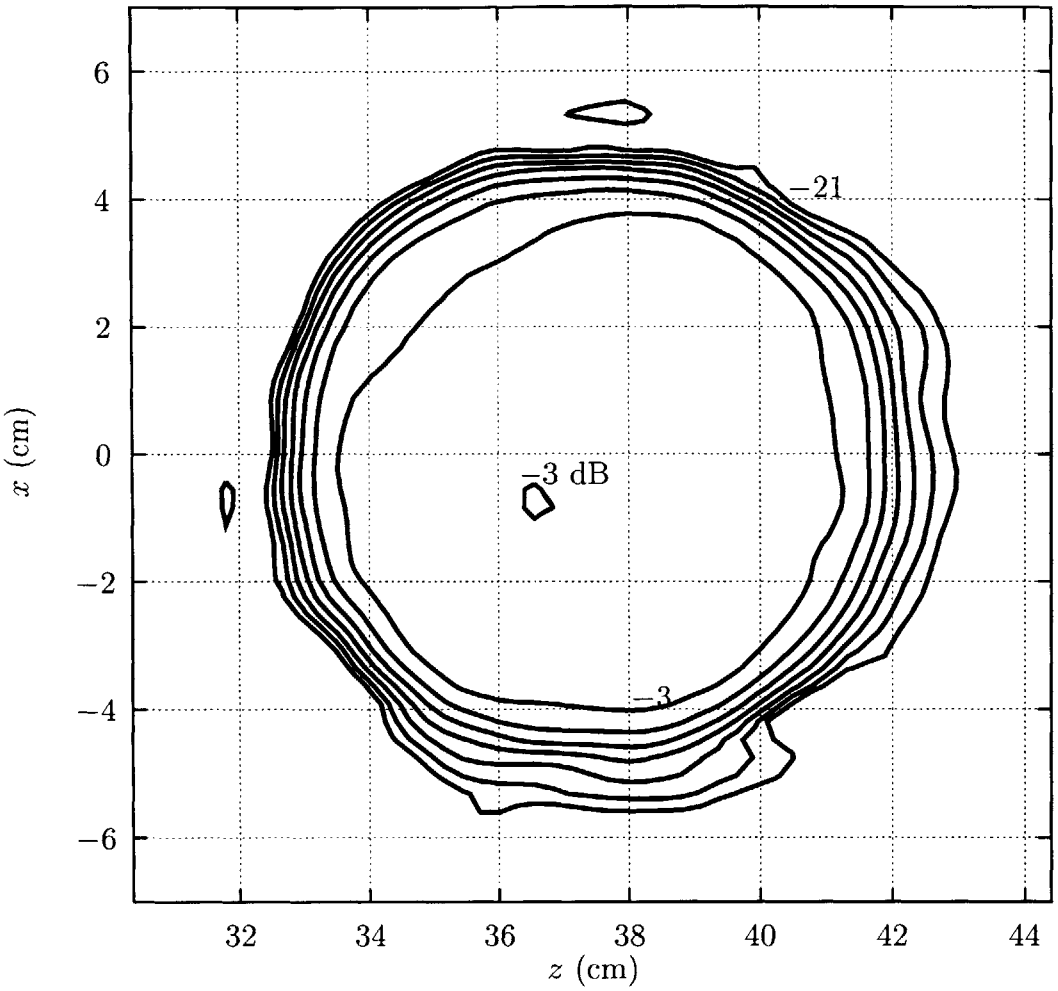

Figure 1-6: Theoretically-predicted field intensity pattern at the plane of the 10-cm-aperture window. Contours of constant $|E_x|^2$ are at 3 dB intervals from peak; the -3 dB and -21 dB curves are labeled.

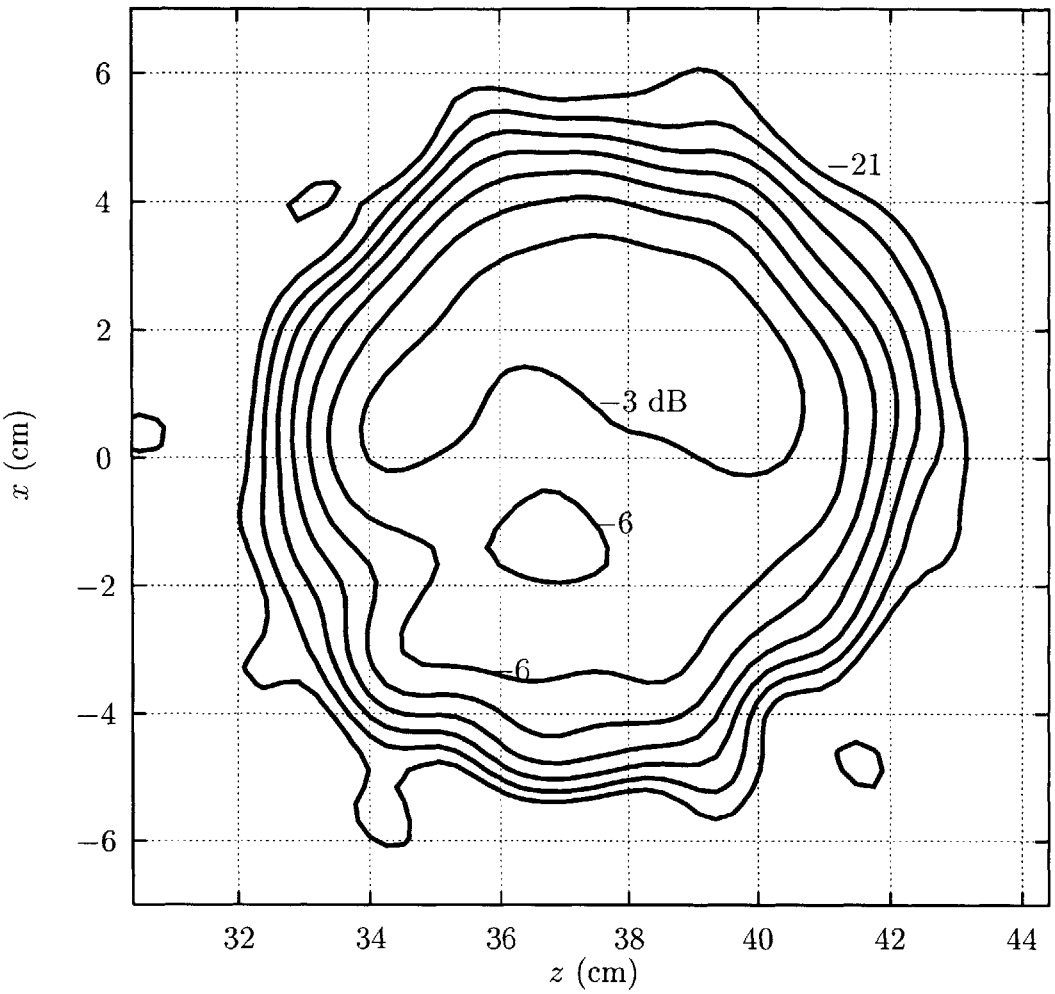

Figure 1-7: Measured field intensity pattern at the plane of the 10-cm-aperture window. Contours of constant $|E_x|^2$ are at 3 dB intervals from peak; the -3 dB and -21 dB curves are labeled.

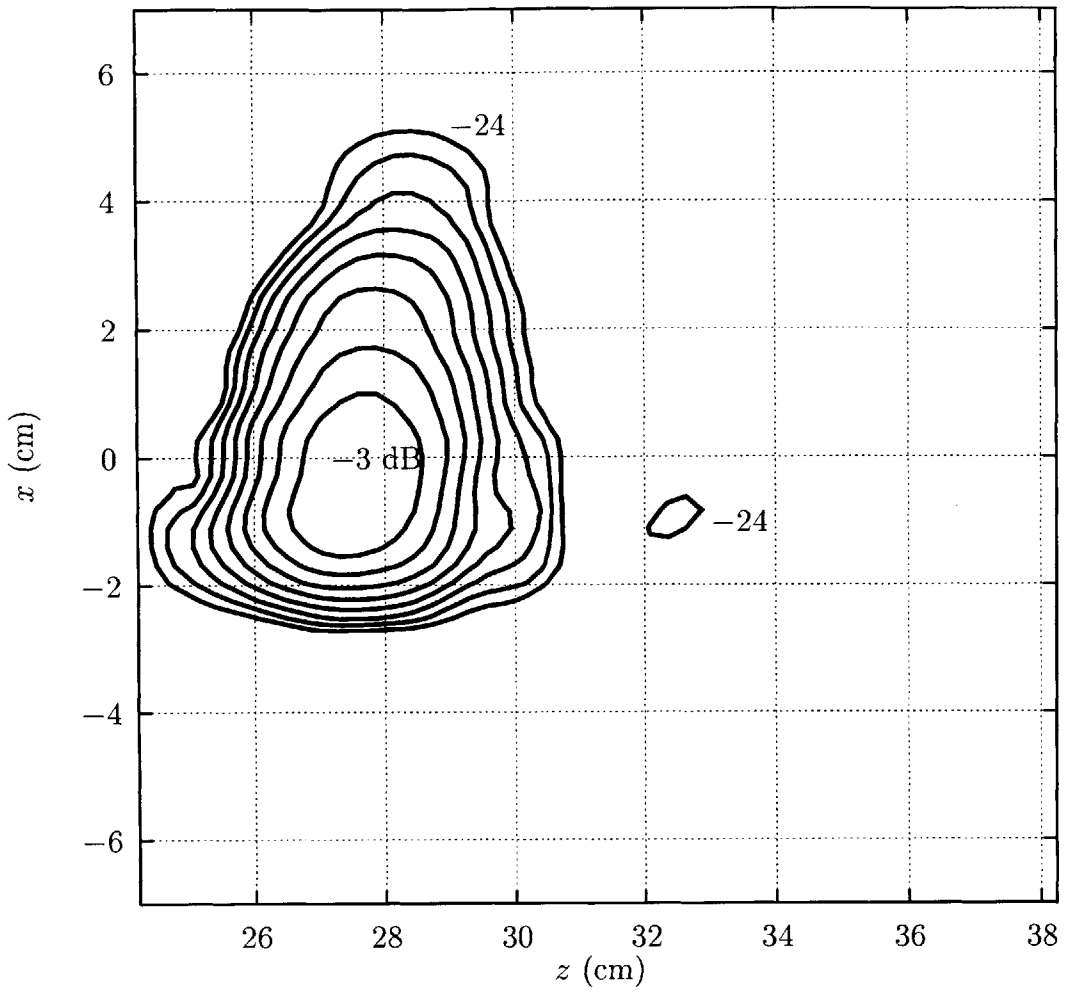

Figure 1-8: Theoretically-predicted field intensity over a plane at the mirror three position. Contours of constant $|E_x|^2$ are at 3 dB intervals from peak; the -3 dB and -24 dB curves are labeled.

window electric field intensity profiles.

These differences may arise from machining errors in the launcher, misalignment of the launcher with respect to the mirrors, or an incomplete theory for the launcher. Such variations from the ideal, theoretical situation then suggest that any mirror design based on simulated fields will not produce the desired output field in actual operation. In order to overcome the observed difficulties in forming the desired microwave beam shape in a gyrotron, we propose a new approach to mirror design that incorporates measured field intensities in the design process.

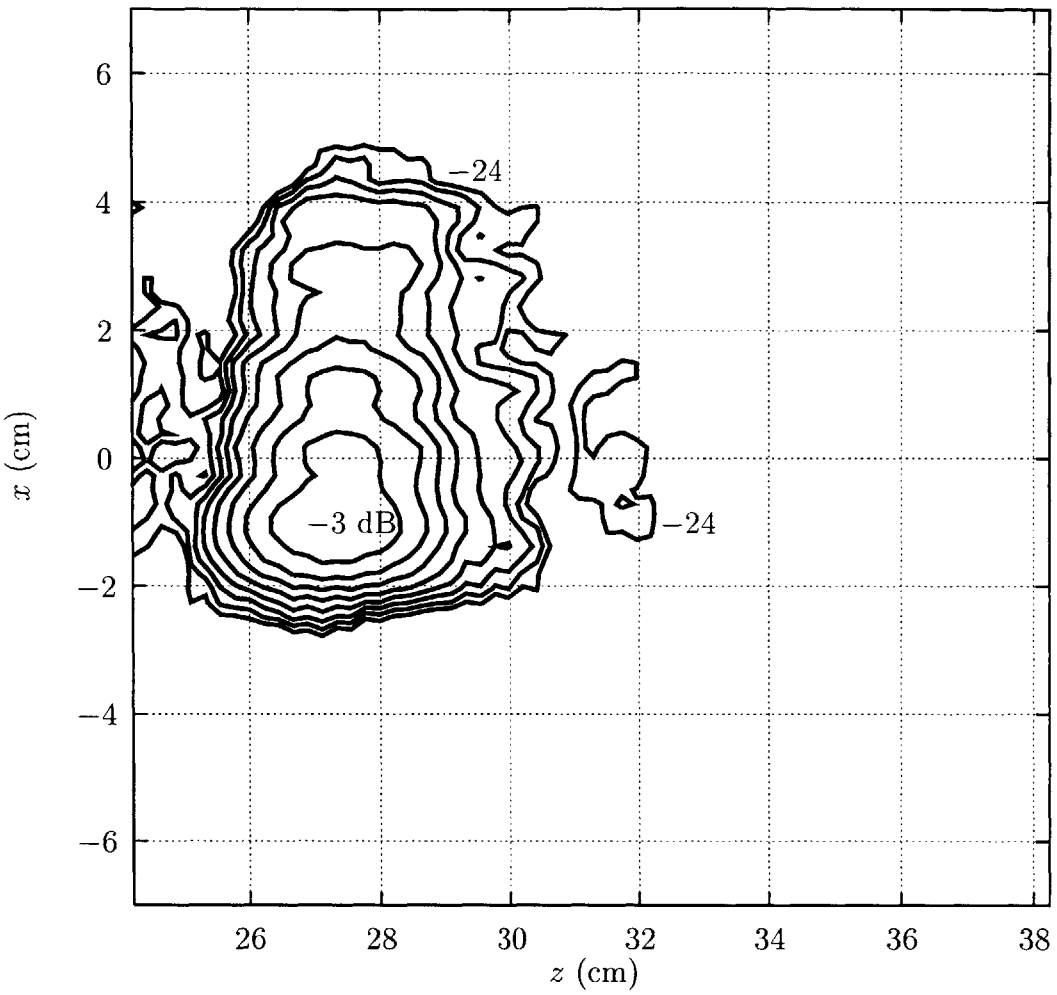

Figure 1-9: Measured field intensity over a plane at the mirror three position. Contours of constant $|E_x|^2$ are at 3 dB intervals from peak; the -3 dB and -24 dB curves are labeled.

1.3 Outline of Mirror Design Approach

The inherent challenge in designing mirrors based on field measurements arises from the difficulty of measuring phase at high frequencies ($f > 100$ GHz). Commercial phase measurement equipment is currently available for frequencies up to 100 GHz, but we are interested in designing components for gyrotrons (and other devices) that operate at frequencies in the 200 GHz region. Additionally, phase measurements at high powers are not possible with the available solid-state receivers.

An alternative to measuring phase is to recover the phase of a wave from a knowledge of its intensity over a series of measurement planes. To account for the actual fields in the mode converter, we offer the following procedure for designing the mirrors based on intensity-only measurements [8, 9]:

1. Design and build the launcher to produce a Gaussian-like beam.
2. Measure the field radiated by the launcher and design the first doubly-curved mirror (M1 in Figure 1-3) by fitting an elliptical Gaussian beam to the measured pattern.
3. Measure the field intensity following the first mirror and design the second mirror (M2) based on a best-fit Gaussian.
4. Measure the field intensity following the second mirror and retrieve the phase of the beam to reconstruct the full field structure of the wave.
5. Use the reconstructed field after the second mirror and the desired field structure on the window as input to a mirror shaping procedure to determine the surface profiles for mirrors three and four (M3 and M4, respectively).
6. Simulate mirrors three and four in a numerical electromagnetics code to verify the design.

From the above outline we see that the launcher and first two mirrors can be considered as the feed in an off-set fed, dual reflector antenna, where mirrors three and four are shaped reflectors that transform the feed field into a desired radiated field. Typically, mode converter mirrors are large reflectors with aperture widths in the range of 20λ to 50λ. Traditional analysis methods such as the physical optics approximation then apply to the mode converter problem, and by reciprocity we expect our design method to apply to reflector antennas. This generality of formulation then extends the proposed design procedure to areas such as reflector antenna synthesis, radio astronomy, and free-space transmission lines.

1.4 Thesis Outline

This thesis presents a systematic development of the components necessary to implement the mirror shaping approach described in Section 1.3 and provides experimental validation of the design procedure.

A method for determining the phase from a set of intensity measurements over consecutive planes is formulated in Chapter 2. We briefly summarize the relevant literature and then introduce an iterative algorithm for retrieving phase from intensity information. This algorithm is implemented numerically, and we discuss several representative computational examples.

Chapter 3 describes a method for shaping a pair of mirrors to transform an incident wave into a desired radiated wave. The mirrors are treated as phase correctors, which allows us to use the phase retrieval algorithm developed in Chapter 2 for defining the mirror surfaces. We then present an example mirror design based on simulated fields in a mode converter as a first test of the procedure.

An external mode converter, referred to as a matching optics unit (MOU), provides the first experimental study of the proposed mirror design approach, and the results are detailed in Chapter 4. Beginning with infrared camera measurements of the microwave beam radiated by a gyrotron, we retrieve the phase and construct a pair of mirrors to transform the gyrotron beam into a Gaussian beam. The design process and the radiation from the MOU are fully discussed in Chapter 4.

Chapter 5 presents the design and measurements of mirrors for an internal mode converter. The mirrors transform the field inside the mode converter into a Gaussian beam suitable for transmission through a 5-cm-aperture diamond window that is capable of handling power levels of over 1 MW. Analysis of the field intensity measurements, design of the mirrors, and low- and high-power experimental results for the internal mode converter are presented.

Chapter 6 concludes the thesis with a summary of results and a discussion of future work.

Chapter 2

Phase Retrieval from Intensity Measurements

The mirror design approach outlined in Section 1.3 requires a technique for recovering the phase of a wave from measurements of its field intensity. This chapter begins with a review of essential wave nomenclature and conventions, and then presents the formulation of an iterative algorithm for retrieving phase from intensity measurements. Following the general analytic treatment of phase retrieval, we discuss the numerical implementation of the algorithm and present several examples that illustrate the capabilities and limitations of this implementation.

2.1 Preliminaries

We begin our discussion by presenting the wave nomenclature and conventions used throughout this work. The time-dependent scalar wave function $\tilde{\psi}(x, y, z, t)$ can be expressed as a time-harmonic field with angular frequency ω by writing

$$\tilde{\psi}(x, y, z, t) = \Re\left\{\psi(x, y, z)e^{-i\omega t}\right\}. \tag{2.1}$$

The function $\psi(x, y, z)$ satisfies the time-independent, source-free Helmholtz equation:

$$(\nabla^2 + k^2)\psi(x, y, z) = 0, \tag{2.2}$$

where $k = \omega/c$ is the free-space wave number and the time-harmonic factor $\exp(-i\omega t)$ has now been suppressed. The wave number k is related to the individual wave vectors

in Cartesian coordinates by the dispersion relation

$$k^2 = {k_x}^2 + {k_y}^2 + {k_z}^2. \tag{2.3}$$

The wave function $\psi(x, y, z)$ can be represented as a weighted superposition of plane waves via the Fourier integral [5, 10]

$$\psi(x, y, z) = \int_{-\infty}^{\infty} dk_x \int_{-\infty}^{\infty} dk_y \, \Psi_0(k_x, k_y) e^{ik_x x} e^{ik_y y} e^{ik_z z}, \tag{2.4}$$

where

$$\Psi_0(k_x, k_y) = \left(\frac{1}{2\pi}\right)^2 \int_{-\infty}^{\infty} dx \int_{-\infty}^{\infty} dy \, \psi(x, y, z = 0) e^{-ik_x x} e^{-ik_y y} \tag{2.5}$$

is the plane wave amplitude spectrum. We recognize (2.5) as the Fourier transform of $\psi(x, y, z = 0)$, and we can rewrite (2.5) more compactly using the notation

$$\Psi_0(k_x, k_y) = \mathcal{F}\left\{\psi(x, y, z = 0)\right\}. \tag{2.6}$$

Similarly, (2.4) becomes

$$\psi(x, y, z) = \mathcal{F}^{-1}\left\{\Psi_0(k_x, k_y) \cdot e^{iz\sqrt{k^2 - {k_x}^2 - {k_y}^2}}\right\} \tag{2.7}$$

where $\mathcal{F}^{-1}$ is shorthand for the inverse Fourier transform. Here we have made use of the dispersion relation (2.3) to write k_z explicitly in terms of the transform variables k_x and k_y.

This choice of plane wave expansion in terms of Fourier integrals then allows us to compactly express the relationship between fields over two planes. Substituting (2.5) into (2.4) and making use of (2.6) and (2.7) yields

$$\psi(x, y, z) = \mathcal{F}^{-1}\left\{\mathcal{F}\{\psi(x, y, z = 0)\} \cdot e^{iz\sqrt{k^2 - {k_x}^2 - {k_y}^2}}\right\}. \tag{2.8}$$

We will also find it useful to consider the paraxial limit of (2.2), where we write $\psi(x, y, z) = u(x, y, z)e^{ikz}$ and make the paraxial approximation that (see e.g. [5] or [11]):

$$\frac{\partial^2 u}{\partial z^2} \ll ik\frac{\partial u}{\partial z.} \tag{2.9}$$

This approximation states that a paraxial wave propagating along the z-axis is a slowly-varying function of z. A further consequence of (2.9) is that the divergence of the wave is small, implying $k \approx k_z$. Therefore, we can write an analogous relation

to (2.9) for the paraxial limit in k-space as

$$k_x, k_y \ll k. \tag{2.10}$$

We can find wave solutions that satisfy (2.9) and (2.10) by expanding ∇^2 in (2.2) in Cartesian coordinates and making use of (2.9) to yield the paraxial wave equation:

$$\left(\frac{\partial^2}{\partial x^2} + \frac{\partial^2}{\partial y^2} + i2k\frac{\partial}{\partial z}\right) u(x, y, z) = 0. \tag{2.11}$$

A first-order solution to this equation is the fundamental Gaussian beam expressed as

$$\psi_{00}(x, y, z) = \sqrt{\frac{2}{\pi w^2(z)}} e^{-i\tan\varphi} e^{-(x^2+y^2)/w^2(z)} e^{\frac{ik}{2R}(x^2+y^2)} e^{ikz}, \tag{2.12}$$

where

$$w^2(z) = {w_0}^2 \left(1 + \left(\frac{\lambda z}{\pi {w_0}^2}\right)^2\right), \tag{2.13}$$

$$\frac{1}{R} = \frac{z}{z^2 + (\pi {w_0}^2/\lambda)^2}, \tag{2.14}$$

$$\tan\varphi = \frac{z}{\pi {w_0}^2/\lambda}, \tag{2.15}$$

and w_0 is the minimum waist size at the beam focus. Higher-order solutions are given by products of Hermite polynomials and Gaussian functions in Cartesian coordinates [5], or Laguerre polynomials and Gaussian functions in cylindrical coordinates [12].

2.2 Formulation of the Iterative Phase Retrieval Algorithm

2.2.1 General Formulation

Consider the geometry shown in Figure 2-1 for determining the phase from given field intensity (or amplitude, where $A = \sqrt{I}$) values over two planes. We want to find the two phase functions $\phi_1(x, y)$ and $\phi_2(x, y)$ from a knowledge of the amplitude functions $A_1(x, y)$ and $A_2(x, y)$. In 1967, Katsenelenbaum and Semenov [13] proposed an iterative method to solve this problem in terms of synthesizing phase correctors in microwave transmission lines. A similar iterative procedure was introduced (evidently

independently) by Gerchberg and Saxton [14] for the more restrictive case of retrieving phase from an object function and its Fourier transform with application to electron microscopy. Their approach has, in the West, since been referred to as the Gerchberg-Saxton algorithm. The general case of two or more arbitrary measurement planes is presented as a modified Gerchberg-Saxton algorithm by Anderson and Sali [15], and we outline a similar method below. Although the formulation is in terms of scalar fields, we can always decompose the beam in free space as a sum of three linear field vectors.

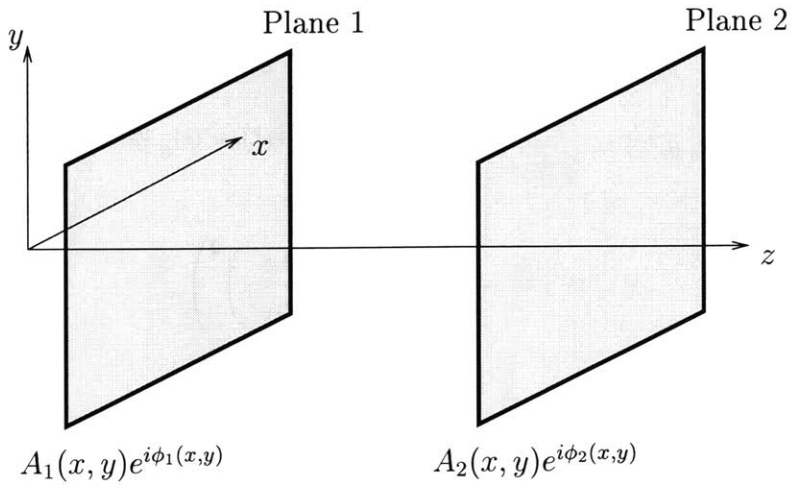

Figure 2-1: Geometry for phase retrieval from intensity measurements.

Suppose we have two measurement planes, perpendicular to the z-axis in a Cartesian coordinate system, with a wave propagating roughly paraxially, or quasi-optically, along the z-axis. The measurement planes are located at z_1 and z_2 with $z_1 < z_2$, and the (for now continuous) measured amplitudes over each plane are denoted $A_1(x,y)$ and $A_2(x,y)$, respectively.

The total scalar fields on the two measurement planes are then written as

$$\psi(x,y,z_1) = \psi_1(x,y) = A_1(x,y)e^{i\phi_1(x,y)} \tag{2.16}$$

$$\psi(x,y,z_2) = \psi_2(x,y) = A_2(x,y)e^{i\phi_2(x,y)}, \tag{2.17}$$

where $\phi_1(x,y)$ and $\phi_2(x,y)$ are the exact phases on their respective planes. We can relate the two field functions above by defining a propagation operator $\mathcal{P}_{12}$ in terms of (2.8):

$$\psi_2(x,y) = \mathcal{P}_{12}\left\{\psi_1(x,y)\right\} \equiv \mathcal{F}^{-1}\left\{\mathcal{F}\{\psi_1(x,y)\} \cdot e^{i(z_2-z_1)\sqrt{k^2-{k_x}^2-{k_y}^2}}\right\}. \tag{2.18}$$

Now suppose that the phase functions $\phi_1(x,y)$ and $\phi_2(x,y)$ are unknown. We can iteratively determine the phase from the measured amplitudes with the following algorithm. Construct a field profile over the first plane from the known amplitude function $A_1(x,y)$ as

$$\psi_1{}^{(0)}(x,y) = A_1(x,y)e^{i\phi_1{}^{(0)}(x,y)}, \tag{2.19}$$

where $\phi_1{}^{(0)}$ is our initial phase guess on the first plane. We then propagate this field distribution to the second plane via the propagation operator $\mathcal{P}_{12}$:

$$\psi_2{}^{(0)}(x,y) = A_2{}^{(0)}(x,y)e^{i\phi_2{}^{(0)}(x,y)} = \mathcal{P}_{12}\left\{\psi_1{}^{(0)}\right\}. \tag{2.20}$$

In order to move the field solution $\psi_2{}^{(0)}(x,y)$ closer to the actual fields on plane 2, we use the known amplitude to form a new function

$$\psi_2'{}^{(0)}(x,y) = A_2(x,y)e^{i\phi_2{}^{(0)}(x,y)}, \tag{2.21}$$

where we have replaced the computed amplitude function $A_2{}^{(0)}(x,y)$ with the given amplitude while retaining the computed phase. We again apply the propagation operator to determine the fields on plane 1:

$$\psi_1'{}^{(0)}(x,y) = A_1'{}^{(0)}(x,y)e^{i\phi_1'{}^{(0)}(x,y)} = \mathcal{P}_{21}\left\{\psi_2'{}^{(0)}\right\}. \tag{2.22}$$

The next step brings the routine full-circle by forming a field on plane 1 from the known amplitude $A_1(x,y)$ and the recently-computed phase $\phi_1'{}^{(0)}$ as

$$\psi_1{}^{(1)}(x,y) = A_1(x,y)e^{i\phi_1'{}^{(0)}(x,y)} \equiv A_1(x,y)e^{i\phi_1{}^{(1)}(x,y)} \tag{2.23}$$

Figure 2-2 gives a summary of the above steps for the mth iteration stage, and the algorithm continues for a total of M iterations.

The process is repeated until (ideally) the computed amplitude on each plane matches the measured amplitude on that plane. We show in the next section that the iterative algorithm is essentially an error reduction algorithm that moves the computed amplitude values closer to those of the measured amplitude at each pass.

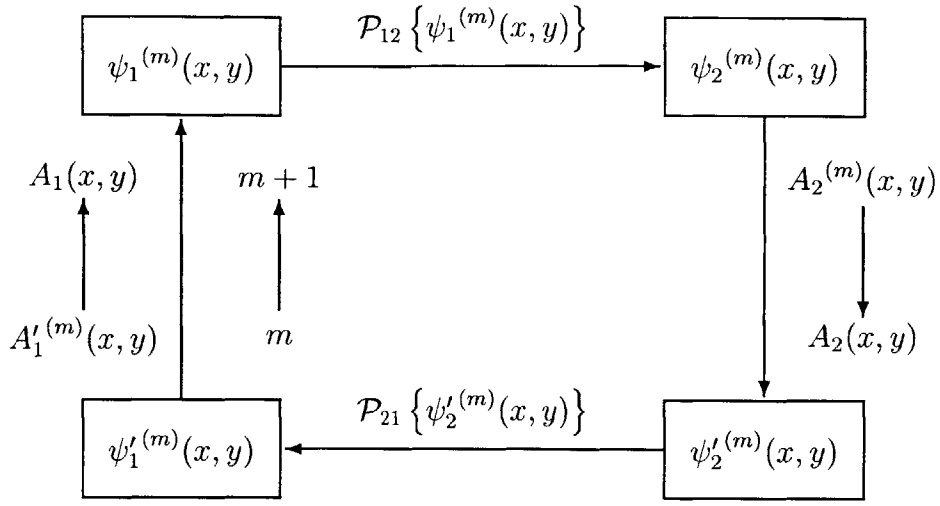

Figure 2-2: Flow chart for the mth stage of the iterative phase retrieval algorithm.

2.2.2 Convergence for the Case of Functions Related by the Fourier Transform

Although the above formulation is in terms of two arbitrary measurement planes, we can gain some insight into the convergence of the algorithm by specifying that the fields on each plane are related through the Fourier transform. By working with a Fourier transform pair, we can simplify the computation (propagation from one plane to the other requires only one Fourier transform) and we can appeal to Parseval's relation to find an explicit correspondence between the object and Fourier domains. Using this tactic, we show that the iterative algorithm is an error-reduction algorithm [16].

Consider the two functions defined as

$$\psi(x) = A_0(x)e^{i\theta(x)} \tag{2.24}$$

$$\Psi(k) = A_F(k)e^{i\eta(k)}, \tag{2.25}$$

where $\Psi(k) = \mathcal{F}\{\psi(x)\}$, and we have introduced the notation $x \equiv (x,y), k \equiv (k_x, k_y)$. We want to iteratively determine $\eta(k)$ and $\theta(x)$ in a manner analogous to the procedure formulated in Section 2.2.1. We can write a series of expressions (similar to

(2.19) – (2.23)) for these functions after the mth iteration:

$$\Psi^{(m)}(k) = |\Psi^{(m)}(k)|e^{i\eta^{(m)}(k)} = \mathcal{F}\{\psi^{(m)}(x)\} \tag{2.26}$$

$$\Psi'^{(m)}(k) = A_F(k)e^{i\eta^{(m)}(k)} \tag{2.27}$$

$$\psi'^{(m)}(x) = |\psi'^{(m)}(x)|e^{i\theta'^{(m)}(x)} = \mathcal{F}^{-1}\{\Psi'^{(m)}(k)\} \tag{2.28}$$

$$\psi^{(m+1)}(k) = A_0(x)e^{i\theta^{(m+1)}(x)} = A_0(x)e^{i\theta'^{(m)}} \tag{2.29}$$

We want to show that the difference between the computed amplitudes and given (measured) amplitudes at iteration $m+1$ is less than the difference at iteration m; i.e., that the computed amplitude values at each point in x (or k) are approaching the given values. In the Fourier domain, this difference at the mth iteration is defined by the squared error

$$E_F{}^{(m)} = \frac{1}{N^2}\sum_k |\Psi'^{(m)}(k) - \Psi^{(m)}(k)|^2 \tag{2.30}$$

We can factor the common phase terms from $\Psi'^{(m)}$ and $\Psi^{(m)}$ and use (2.27) to re-write (2.30) as

$$E_F{}^{(m)} = \frac{1}{N^2}\sum_k [A_F(k) - |\Psi^{(m)}(k)|]^2. \tag{2.31}$$

Following the same argument, the error in the object domain is

$$E_0{}^{(m)} = \sum_x |\psi^{(m+1)}(x) - \psi'^{(m)}(x)|^2. \tag{2.32}$$

Factoring the phase and making the substitution for $\psi^{(m+1)}(x)$ in (2.29) gives

$$E_0{}^{(m)} = \sum_x [A_0(x) - |\psi'^{(m)}(x)|]^2. \tag{2.33}$$

We can now use Parseval's relation [17] to associate the error in the Fourier domain with the error in the object domain. In the Fourier domain, Parseval's relation yields

$$E_F{}^{(m)} = \frac{1}{N^2}\sum_k |\Psi'^{(m)}(k) - \Psi^{(m)}(k)|^2 = \sum_x |\psi'^{(m)}(x) - \psi^{(m)}(x)|^2. \tag{2.34}$$

We recall that by construction, $\psi^{(m+1)}(x)$ is made to be as close to $\psi'^{(m)}(x)$ as possible

via (2.29) for all x. Then it follows that

$$|\psi'^{(m)}(x) - \psi^{(m+1)}(x)| \leq |\psi'^{(m)}(x) - \psi^{(m)}(x)|. \tag{2.35}$$

Replacing the left and right hand sides of (2.35) by the quantities (2.32) and (2.30) yields the inequality

$${E_0}^{(m)} \leq {E_F}^{(m)}. \tag{2.36}$$

We can use Parseval's relation to write the error in the object domain as

$${E_0}^{(m)} = \sum_x |\psi^{(m+1)}(x) - \psi'^{(m)}(x)|^2 = \frac{1}{N^2} \sum_k |\Psi^{(m+1)}(k) - \Psi'^{(m)}(k)|^2, \tag{2.37}$$

As in the object domain, the function $\Psi'^{(m+1)}(k)$ in the Fourier domain is constructed via (2.27) to be the nearest function to $\Psi^{(m+1)}(k)$ for all k. Then we can form the relation

$$|\Psi^{(m+1)}(k) - \Psi'^{(m+1)}(k)| \leq |\Psi^{(m+1)}(k) - \Psi'^{(m)}(k)| \tag{2.38}$$

Making use of (2.30) and (2.37) with the above inequality gives

$${E_F}^{(m+1)} \leq {E_0}^{(m)} \tag{2.39}$$

Finally, we combine (2.36) and (2.39) to form the desired result that in progressing from iteration m to $m+1$ the error is reduced:

$${E_F}^{(m+1)} \leq {E_0}^{(m)} \leq {E_F}^{(m)} \tag{2.40}$$

2.3 Numerical Implementation

One advantage of the iterative phase retrieval algorithm — and particularly our choice of using the plane wave expansion (2.4) to represent the fields — lies in evaluating (2.18) for the case of discretely-sampled amplitudes. Each plane-to-plane propagation involves two discrete Fourier transforms and one complex multiply. The Fourier transforms are readily accomplished using a two-dimensional Fast Fourier transform [18]. When translating the continuous exponential function in (2.8) to the discrete domain, the wavenumbers k_x and k_y have a finite range limited by the sampling period:

$$\frac{-\pi(N-1)}{L} \leq k_x, k_y \leq \frac{\pi(N-1)}{L}, \tag{2.41}$$

where L is the length of a side of a measurement plane (assumed square), and N is the number of sample points in one-dimension. The only restriction on N, neglecting the practical consideration of computational resources, is that the FFT requires N be a power of 2.

The nature of this numerical implementation imposes two constraints on the wave to be reconstructed from the phase retrieval algorithm. Firstly, the finite range in k-space necessarily limits the expansion of the wave. A rapidly expanding wave has large k_x and k_y values that may not be adequately represented; this effect is tantamount to the familiar aliasing problem in under-sampled signals. A sufficiently-high sampling rate where N/L is large will help avoid this effect, although we specified in our original formulation that the wave of interest is usually paraxial. This stipulation allows us to make N/L modest and in practice a half-wavelength sampling grid is usually more than sufficient to represent the measured wave.

The second constraint turns out to be the real practical limitation: the effect of finite-measurement plane size. In using the two-dimensional discrete Fourier transform, we have implicitly assumed that our signal has a two-dimensional periodicity. If the amplitude at the edge of the measurement plane is not negligible, then the non-zero amplitude will spill over onto the (imagined) adjacent planes and cause aliasing effects. As with the finite k-space constraint, the finite measurement plane effect can be mitigated by specifying that we retrieve the phase of paraxial waves, which are in fact beams with an amplitude profile of interest only over a finite range.

In the next section we provide results from runs of the computer code used to perform the iterative phase retrieval. The code is written in FORTRAN, with all relevant computation done in double-precision arithmetic. The FFT is indeed fast: a single iteration for phase retrieval from two intensity measurements takes approximately 0.7s using the computational resources given in Table 2.1.

2.4 Computational Examples

In this section we present several sample runs of the code used to perform the iterative phase retrieval algorithm. Our goal here is twofold: 1) To assess the integrity of the code and show that the algorithm produces accurate solutions; and 2) To gain insight into the capabilities and limitations of this particular numerical approach.

A useful quantity for the purpose of comparison is a normalized squared error that is a function of the iteration number m. We define this error in a way similar to the

Parameter	Value
CPU	AMD-K6 32-bit
CPU Clock	233 MHz
Bus Clock	66 MHz
RAM	64 MB
Language	FORTRAN
Compiler	g77
O/S	Linux
# Planes	2
N	128
M	100
Total CPU Time	72 s

Table 2.1: Computational parameters for a representative run of the phase retrieval code.

object domain error (2.32):

$$E_{\text{norm}}^{(m)} = \frac{\sum_{(x,y)}[A_1(x,y) - |\psi_1{}^{(m)}(x,y)|]^2}{\sum_{(x,y)} A_1{}^2(x,y)}. \tag{2.42}$$

Convergence implies that this error will monotonically decrease (or at worst remain the same) for increasing m.

2.4.1 Gaussian Beam: A Nominal Example

For our first example, we choose two 14 cm $\times$ 14 cm measurement planes located at $z = 20$ cm and $z = 50$ cm to intercept a (theoretical) Gaussian beam with $w_0 = 2$ cm and $\lambda = 0.273$ cm. Equation (2.12) is used to compute the beam intensity and phase on the two measurement planes, discretized over a 128-point $\times$ 128-point grid. We then retrieve the phase of the wave from these two intensity profiles with a uniform distribution for the initial phase guess; i.e., $\phi_1{}^{(0)}(x,y) = 0$ for all x, y.

Figure 2-3 shows the normalized squared error (2.42), and we see that the algorithm rapidly converges to a solution, as evidenced by the zero-slope in the error after $m = 10$. This convergence is not surprising; the uniform initial phase is a natural phase function for an ideal Gaussian beam, and the process of retrieving the phase amounts to shifting this initial phase guess to the position of the beam waist.

To better characterize the performance of the algorithm, we can form a field from the reconstructed amplitude and phase after $M = 20$ iterations and propagate that

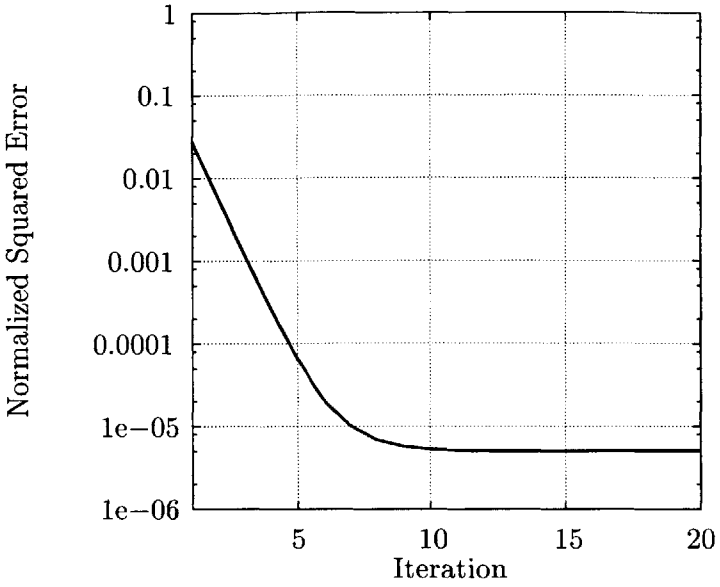

Figure 2-3: Normalized squared error for retrieving phase from Gaussian beam field intensities at $z = 20$ cm and $z = 50$ cm, where the beam focus is at $z = 0$. The measurement plane dimension $L = 14$ cm.

field to a plane outside of the phase retrieval space. That is, we choose some z_{obs} position for an observation plane that lies outside of the range $z_1 < z < z_2$ to form an independent check of the recovered solution by propagating the reconstructed field to the observation plane via (2.18):

$$\psi_{\text{obs}}(x, y) = \mathcal{P}_{1,\text{obs}} \left\{ \psi_1{}^{(M)}(x, y) \right\}. \tag{2.43}$$

Agreement between given and reconstructed fields on this independent plane along with convergence of the error (2.42) — which gives a measure of agreement between the given and reconstructed fields on the reconstruction planes themselves — implies that we have attained the solution.

Figure 2-4 shows the field intensity and phase of $\psi_{\text{obs}}(x, y)$, where $z_{\text{obs}} = -30$ cm. The field patterns are symmetric about $(x, y) = (0, 0)$ on the observation plane, so Figure 2-4 gives cuts in the intensity and phase data along the x-axis. For comparison, the ideal Gaussian intensity and phase are also shown, and we see that there is excellent agreement between the ideal and reconstructed curves for both intensity and phase. Particularly, we note that the intensity curves agree exactly for values greater than -40 dB (Figure 2-4(a)). The deviation of the reconstructed curve from the ideal curve for intensities less that -40 dB results from the finite measurement plane size. As discussed in Section 2.3, our use of the discrete Fourier transform

(or FFT) implies periodicity in x and y. The distortion in the intensity curve near the edges of the observation plane results from aliasing of the neighboring periodic distributions into our observation space. We see a similar behavior in the phase (Figure 2-4(b)) if we ignore the 2π phase discontinuity.

This simple example has produced some important results. We see that our phase retrieval code accurately reconstructs the amplitude and phase of a Gaussian beam from two intensity profiles, validating both the concept of the iterative phase retrieval algorithm and its current numerical implementation. We have also identified a limitation in the ability of the method to adequately reconstruct the fields near the edge of an observation plane; we explore this property of the algorithm in the next section.

2.4.2 Gaussian Beam: Small Measurement Plane

In the previous example, the measurement planes were 14 cm $\times$ 14 cm square. At the $z = 50$ cm position, where the Gaussian beam has its largest waist (relative to the planes at $z = -30$ cm and $z = 20$ cm), the -50 dB curve falls entirely inside the plane, indicating that the measurement plane collects 99.999% of the beam power. We saw in that case the phase retrieval algorithm produces an accurate solution to -40 dB.

In order to gain insight into the influence of measurement plane size on the accuracy of the phase retrieval algorithm, we repeat the above reconstruction for the case of measurement planes with $L = 10$ cm. This smaller plane size intercepts beam intensity contour values > -25 dB at $z = 50$ cm, and truncates all the lower-intensity curves. Performing the reconstruction with the same parameters used in Section 2.4.1 allows us to compare the results for different plane sizes.

Figure 2-5 shows the normalized squared error for this smaller-plane size case. We see that the algorithm again rapidly converges, but the value of the final normalized squared error after 20 iterations is significantly higher than that in Figure 2-3 for the larger plane dimensions. The physical manifestation of this weaker convergence is shown in Figure 2-6, which gives the intensity and phase on the observation plane located at $z = -30$ cm, and we see that the reconstructed fields begin to deviate from the ideal for intensity values < -15 dB. This result arises because we have truncated the fields on the second ($z = 50$ cm plane) at -25 dB, and the overall field structure must be perturbed from the ideal Gaussian in order to compensate for this discontinuity.

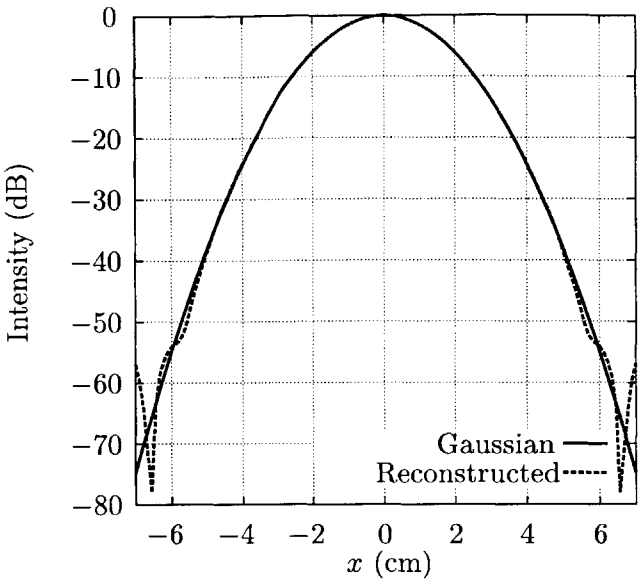

(a) Ideal Gaussian (solid) and reconstructed (dashed) intensities.

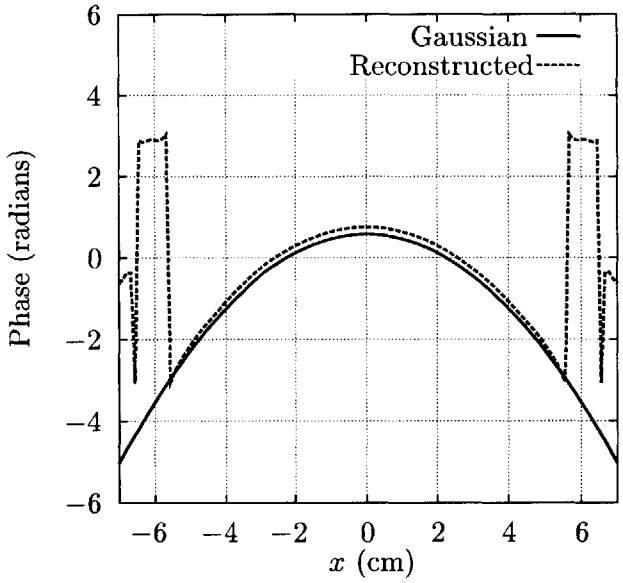

(b) Ideal Gaussian (solid) and reconstructed (dashed) phases.

Figure 2-4: Intensity and phase along the x-axis on the $z = -30$ cm plane, where $z = 0$ is the location of the Gaussian beam focus. Ideal Gaussian amplitudes at $z = 20$ cm and $z = 50$ cm with plane dimension $L = 14$ cm were used in the phase retrieval algorithm with $M = 20$.

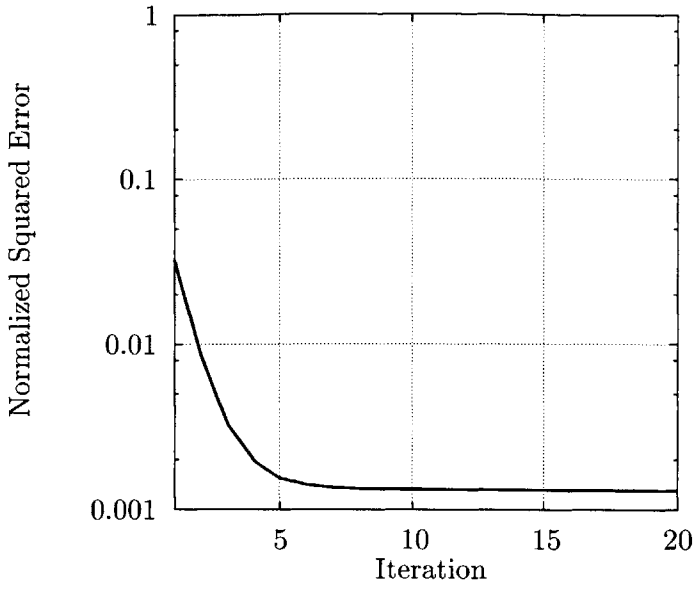

Figure 2-5: Normalized squared error for retrieving phase from Gaussian beam field intensities at $z = 20$ cm and $z = 50$ cm, where the beam focus is at $z = 0$. The measurement plane dimension $L = 10$ cm.

2.4.3 Gaussian Beam: Three Measurement Planes and an Offset Plane

Our formulation of the phase retrieval algorithm has, for simplicity, been limited to the case of defining the field intensity over two measurement planes. The method is very general and can be extended to an arbitrary number of planes. By increasing the number of planes, we in principle increase the amount of information available to the phase retrieval algorithm.

Figure 2-7 shows the convergence of the algorithm for three measurement planes located at $z = 20$ cm, $z = 35$ cm, and $z = 50$ cm, with the ideal Gaussian beam parameters used in Section 2.4.1. Comparing this result to the convergence in Figure 2-3 we see that the convergence is not as rapid for the three-plane case, nor does it reach the same minimum in the three-plane case. We note however that the convergence factor is merely a measure of the agreement between measured and computed amplitudes on a measurement surface. Examining the field on an observation plane reveals that the three-plane case actually produces a slightly more accurate result.

Comparing the observation plane intensity and phase for the three-plane case in Figure 2-8 to those in the two-plane case shown in Figure 2-4, we see in Figure 2-8(a) the agreement between ideal and reconstructed intensity is closer in the -50 dB region than for the two-plane case of Figure 2-4(a). The addition of a measurement

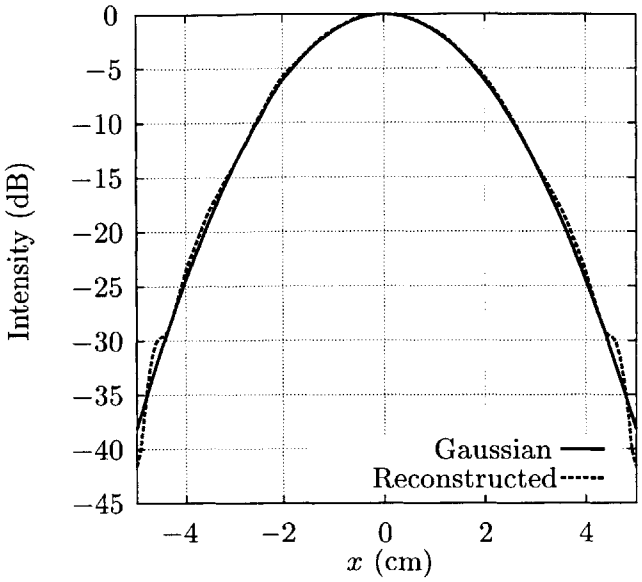

(a) Ideal Gaussian (solid) and reconstructed (dashed) intensities.

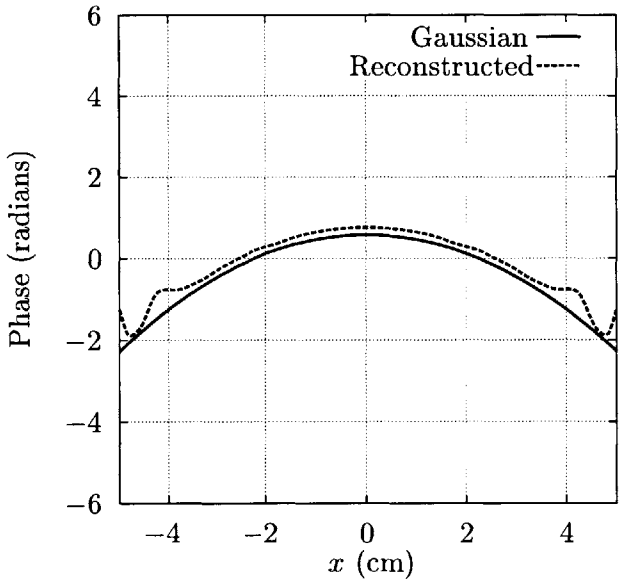

(b) Ideal Gaussian (solid) and reconstructed (dashed) phases.

Figure 2-6: Intensity and phase along the x-axis on the $z = -30$ cm plane, where $z = 0$ is the location of the Gaussian beam focus. Ideal Gaussian amplitudes at $z = 20$ cm and $z = 50$ cm with plane dimension $L = 10$ cm were used in the phase retrieval algorithm with $M = 20$.

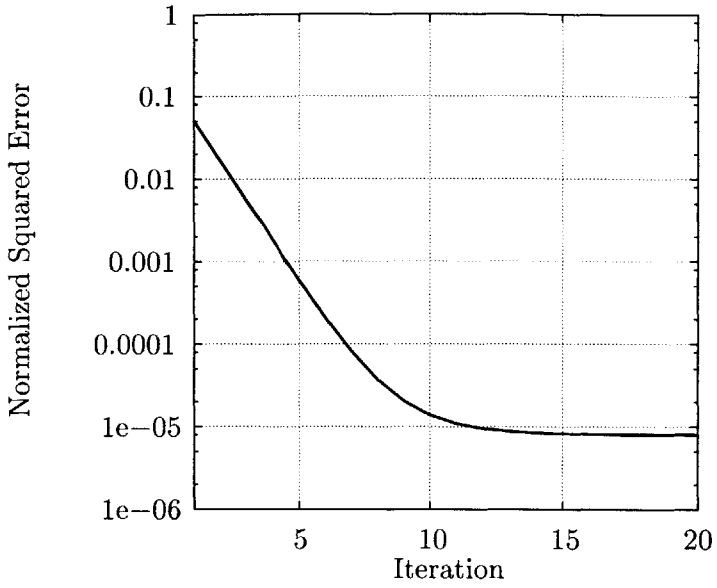

Figure 2-7: Normalized squared error as a function of iteration number for the case of retrieving the phase of an ideal Gaussian beam with measurement planes at $z = 20$ cm, $z = 35$ cm, and $z = 50$ cm. The plane dimension $L = 14$ cm.

plane has provided extra information that the algorithm uses to overcome some of the effects of the discontinuous truncation in field intensities, particularly the truncation at the $z = 50$ cm plane.

We can conceive, however, of a case where more than two planes may be a hindrance. Suppose we make measurements of field intensity over two planes, and suppose further than the centers of the two measurements become displaced through some error. Then the phase retrieval algorithm will overcome this displacement by simply adding an overall tilt to the phase, thus accounting for any (albeit artificial) off-axis beam propagation. If we take three planes and similarly displace them, then we can imagine that the phase retrieval algorithm will not converge on a solution. For instance, if the center plane is displaced with respect to the outer planes in the three-plane system, then the beam is required to swerve in space; this is obviously a non-physical situation.

To examine the error introduced by such a displacement, consider the case of imposing a 0.3 cm (approximately 1λ) offset to the intensity profile on the center $z = 35$ cm plane from the above three-plane example. Figure 2-9 shows the convergence of the algorithm in this case for 100 iterations. We see that the algorithm at first converges, then diverges, then reaches a steady-state.

The initial convergence of the algorithm occurs because we are moving from a gross

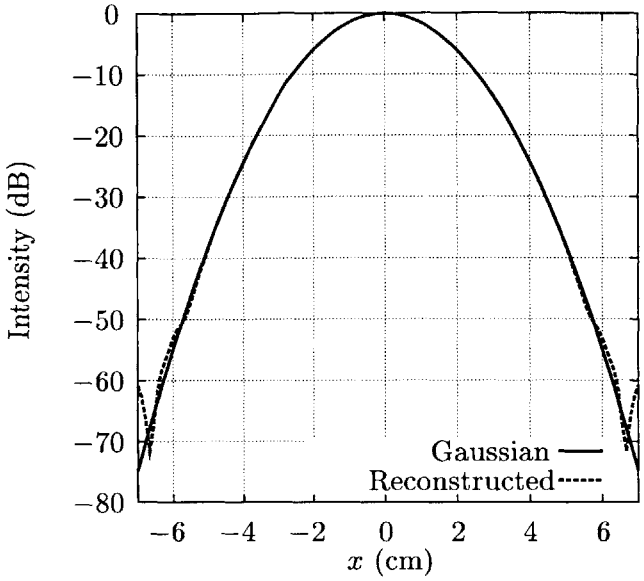

(a) Ideal Gaussian (solid) and reconstructed (dashed) intensities.

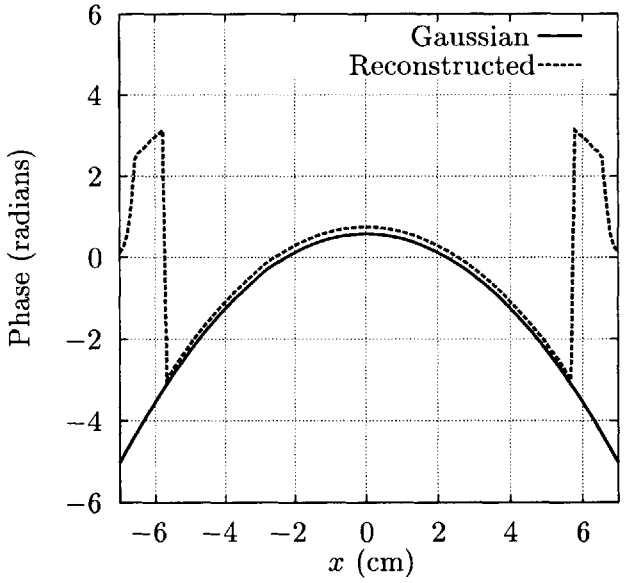

(b) Ideal Gaussian (solid) and reconstructed (dashed) phases.

Figure 2-8: Intensity and phase along the x-axis on the $z = -30$ cm plane, where $z = 0$ is the location of the Gaussian beam focus. Ideal Gaussian amplitudes at $z = 20$ cm, $z = 35$ cm, and $z = 50$ cm with plane dimension $L = 14$ cm were used in the phase retrieval algorithm with $M = 20$.

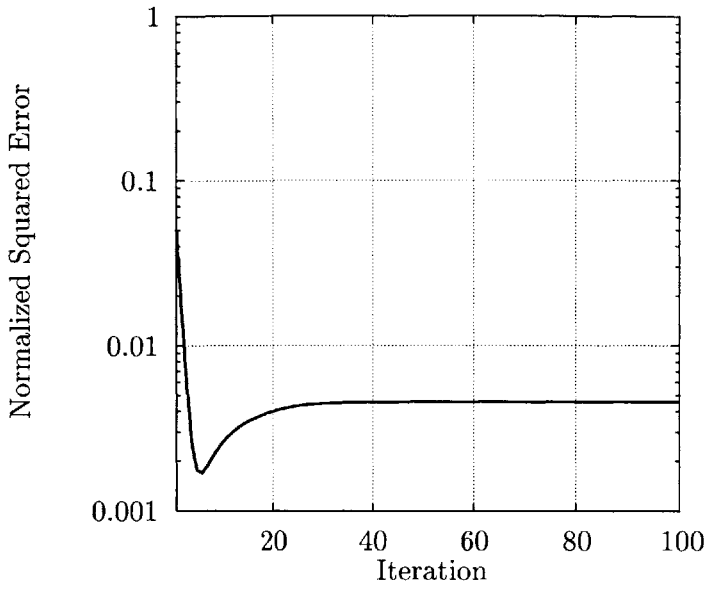

Figure 2-9: Normalized squared error as a function of iteration number for the case of retrieving the phase of an ideal Gaussian beam with measurement planes at $z = 20$ cm, $z = 35$ cm, and $z = 50$ cm. The intensity profile on the $z = 35$ cm plane is offset in x by 0.3 cm ($\sim \lambda$). The plane dimension $L = 14$ cm.

error (our flat initial phase guess) to a more reasonable phase profile. The algorithm then diverges because the amplitude replacement on the center plane actually moves the reconstructed solution *away* from the true solution, thus violating the underlying assumption in our convergence proof of Section 2.2.2. Essentially, the algorithm is forced to choose (in a sense) between satisfying the offset — which amounts to off-axis beam propagation — and satisfying the intensity restrictions on the outer two planes. The final result is a compromise, as shown in Figure 2-10. We see that overall the beam is shifted in x to agree with the off-axis propagation implied by the off-axis center of the middle measurement plane, and also the beam is distorted for lower-intensity values to reflect the optical ellipticity seen by viewing the superposition of two weakly-non-concentric circles.

A cut along the x-axis of this non-symmetric field pattern is shown in Figure 2-11. Both the intensity and the phase of the wave are clearly distorted by the offset plane at $z = 35$ cm (compare Figure 2-8), but interestingly the results are not bad. We see that the reconstructed intensity in Figure 2-11(a), if we neglect the constant shift in x, is reasonably close to the ideal intensity for values as low as -30 dB. A corresponding relationship is also evident for the phase in Figure 2-11(b).

Figure 2-12 shows the intensity and phase along the y-axis for this offset-plane ex-

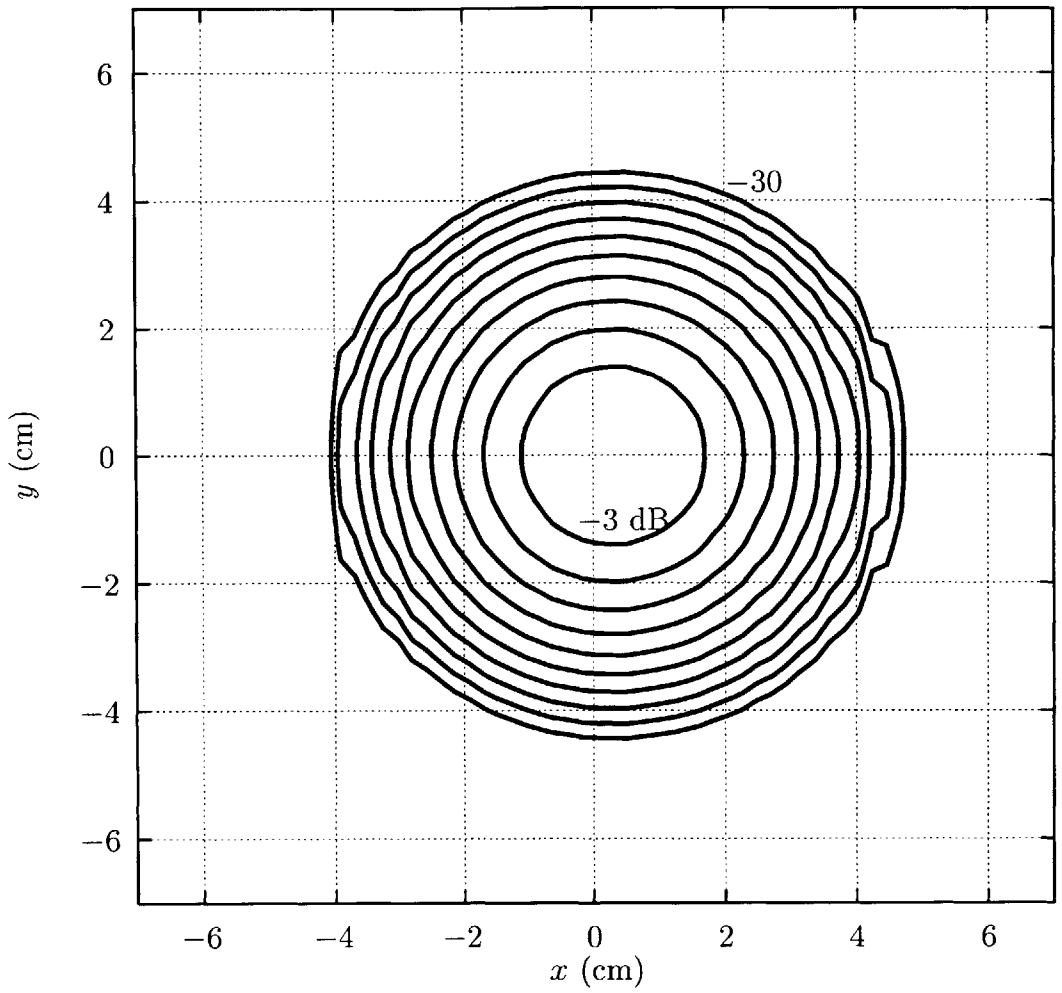

Figure 2-10: Reconstructed field intensity at the $z = -30$ plane. Planes with ideal Gaussian intensity at $z = 20$ cm, $z = 35$ cm, and $z = 50$ cm with plane dimension $L = 14$ cm were used in the phase retrieval algorithm with $M = 100$. The intensity profile at $z = 35$ cm was offset in x by 0.3 cm ($\sim \lambda$). Contours of constant $|E_x|^2$ are at 3 dB intervals from peak; the -3 dB and -30 dB curves are labeled.

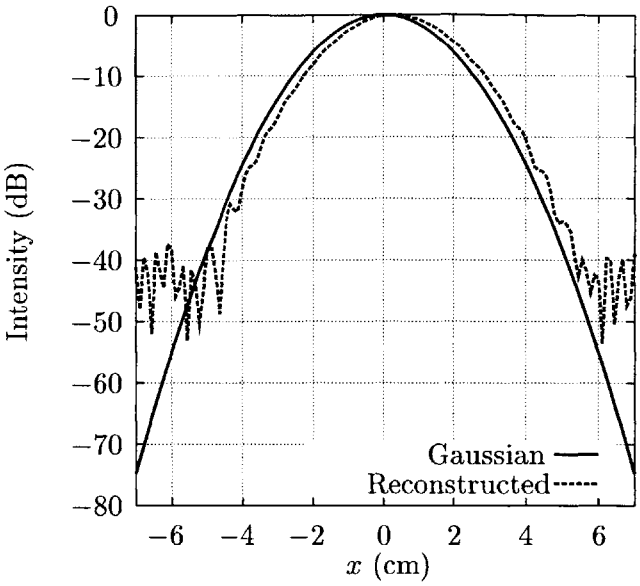

(a) Ideal Gaussian (solid) and reconstructed (dashed) intensities.

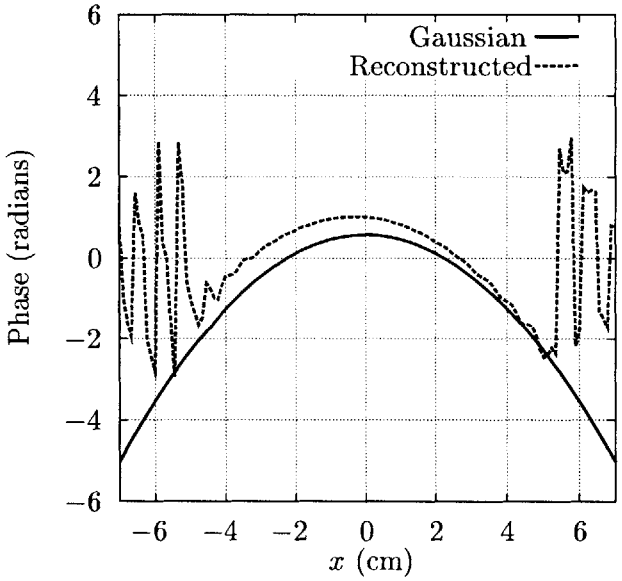

(b) Ideal Gaussian (solid) and reconstructed (dashed) phases.

Figure 2-11: Intensity and phase along the x-axis on the $z = -30$ cm plane, where $z = 0$ is the location of the Gaussian beam focus. Ideal Gaussian amplitudes at $z = 20$ cm, $z = 35$ cm, and $z = 50$ cm with plane dimension $L = 14$ cm were used in the phase retrieval algorithm with $M = 100$. The $z = 35$ cm plane is offset in x by 0.3 cm ($\sim \lambda$).

ample. As we could anticipate from the non-symmetric nature of the contour pattern of Figure 2-10, the reconstructed field pattern in y — as opposed to the pattern in x — is very close to the ideal pattern; in fact, this cut along y is indistinguishable from the nominal three-plane case of Figure 2-8. We would expect that the beam along the y-axis is undistorted because it is essentially decoupled, in terms of plane wave vectors, from the beam behavior in x.

Another important observation about the x-offset result is the nature of the displacement along x of the final beam. In doing the three plane reconstruction, the algorithm is arranged such that the beam propagates from plane 1 to plane 2 to plane 3 back to plane 1. In going from plane 3 to plane 1 in the final step of the iteration, we add an extra bit of information by introducing a new dimension — the distance from plane 1 to plane 3. Our particular choice of plane-to-plane orientation affects the final result. We see in Figure 2-11(a) that the beam is offset to the right in the $+x$-direction. We can understand this result by following the beam propagating during an iteration, as shown in Figure 2-13. The offset pattern on plane 2 initially pulls the beam to the right ($+x$), then it shifts to the left in going to the centered pattern on plane 3. In doing so, the phase shifts accordingly. When the beam propagates from plane 3 to plane 1, that phase behavior remains and the beam has the final angle represented in Figure 2-13. Thus we see why, for our choice of iteration scheme, the final beam on the observation plane at $z = -30$ is offset slightly to the right ($+x$).

2.4.4 Quasi-Gaussian Beam

As a final example, consider the electromagnetic fields inside the internal mode converter shown in Figure 1-3. In anticipation of using the phase retrieval algorithm to design mirrors for this mode converter, we want to first attempt a field reconstruction of simulated data to gain further insight into the phase retrieval procedure and to tackle a problem of greater complexity than the fundamental Gaussian beam treated above.

To understand the computational simulations presented here and in the following chapters, we digress briefly to discuss the numerical routines used to compute the wave structure inside the mode converter. The field inside the rippled-wall launcher is evaluated from a set of coupled mode equations, and the final field in the aperture is radiated into free space through a vector diffraction integral [4]. The incident surface for this radiated wave is the first mirror (M1 in Figure 1-3), and the subse-

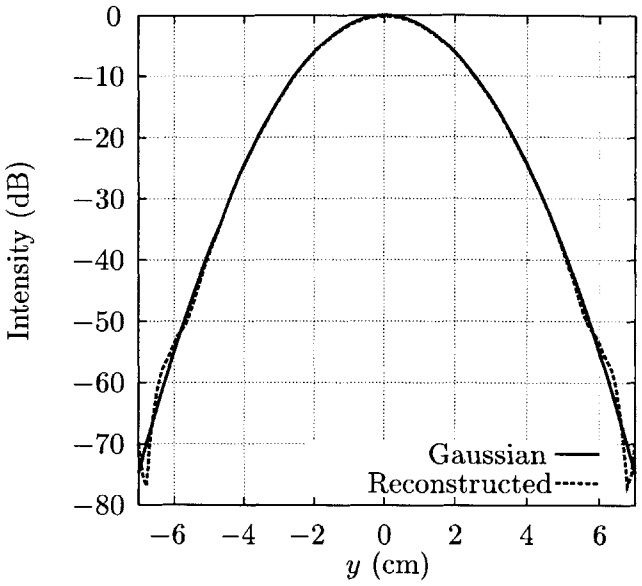

(a) Ideal Gaussian (solid) and reconstructed (dashed) intensities.

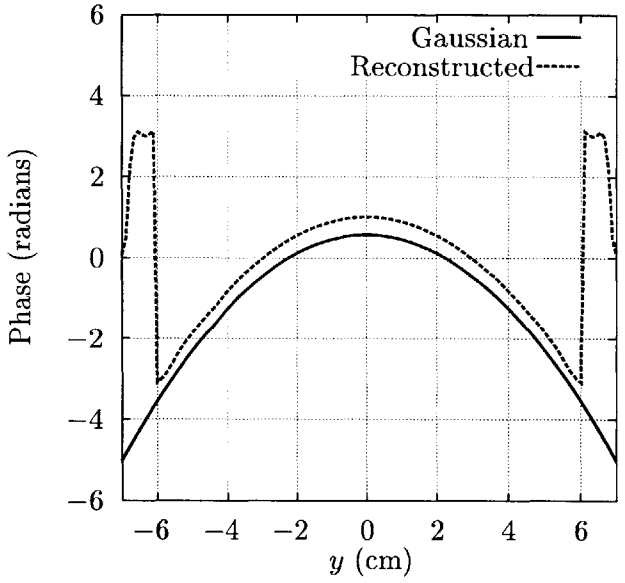

(b) Ideal Gaussian (solid) and reconstructed (dashed) phases.

Figure 2-12: Intensity and phase along the y-axis on the $z = -30$ cm plane, where $z = 0$ is the location of the Gaussian beam focus. Ideal Gaussian amplitudes at $z = 20$ cm, $z = 35$ cm, and $z = 50$ cm with plane dimension $L = 14$ cm were used in the phase retrieval algorithm with $M = 100$. The $z = 35$ cm plane is offset in x by 0.3 cm ($\sim \lambda$).

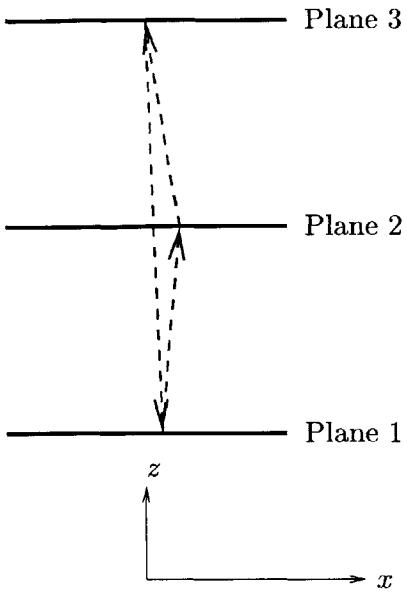

Figure 2-13: Geometry for three plane phase retrieval with the pattern on the second plane offset in the $+x$ direction.

quent mirror-to-mirror propagation is computed using physical optics. The physical optics code evaluates a radiation integral where the integrand is a weighted spherical wave, with the weighting given by surface electric current $\vec{J}_s = 2(\hat{n} \times \vec{H})$, where $\hat{n}$ is the surface normal and $\vec{H}$ is the magnetic field at the perfectly-conducting surface. Under the physical optics approximation, the surface is assumed infinitely flat; this approximation holds, however, for weakly-curved surfaces of finite extent if diffraction can be neglected (i.e. the field intensity at the surface edges are small). This vector-based, spherical-wave integral and its numerical implementation are distinct from the scalar, plane wave expansion approach used in the phase retrieval algorithm and thus provide an independent method for field evaluation.

The physical optics code was used in to compute the theoretical field intensity at the surface of the third mirror (M3) in Figure 1-8. In the mode converter coordinate system, this mirror is located at $y = 11$ cm, with the beam propagating at an angle in the $y - z$ plane ($\vec{k} = \hat{y}k_y + \hat{z}k_z$). We can attempt to retrieve the phase of this wave from simulated intensities at the mirror three plane and at following planes, where the orientation of these measurement planes with respect to the mode converter is shown in Figure 2-14. This exercise has two new elements not present in the numerical examples given above; *viz.*, the beam is not Gaussian and it is propagating at an angle with respect to the measurement planes.

Following an approach similar to that employed in our previous examples, we

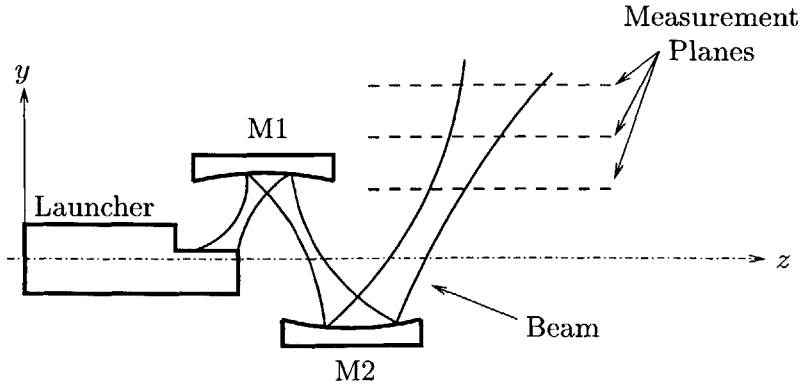

Figure 2-14: Geometry for retrieving the phase from simulated field intensities inside the internal mode converter.

generate given field intensities at the planes $y = 11$ cm, $y = 16$ cm, and $y = 21$ cm (Figure 2-15), and we use these intensities to retrieve the phase. Beginning with a uniform initial phase guess, Figure 2-16 shows that the algorithm takes significantly more iterations to converge than for the earlier Gaussian beam cases. The slow convergence is a result of both a more complicated phase structure and the off-axis beam propagation. We also see in this figure a commonly-observed property of the iterative phase retrieval algorithm (see e.g. [16]) — that the convergence encounters a number of plateaus before finally reaching a quiescent value.

We can understand the meaning of these plateaus by examining the field structure on an independent observation plane, as we did with the Gaussian beam examples. Figure 2-17 shows the simulated field intensity contours on the plane located at $y =$ 6 cm, which is 5 cm before the first measurement plane used in the reconstruction. For comparison, Figure 2-18 gives the field intensity profile on this observation plane due to the reconstructed fields after 100 iterations (100 iterations is the location of the most prominent plateau in Figure 2-16). We see that the larger-intensity values are well reconstructed, but the low intensity contours in the region of -10 dB and below are inaccurate. In contrast, the curves after 500 iterations, as shown in Figure 2-19, exhibit excellent agreement with the given fields for intensities as low as -30 dB. We can conclude from these results that increasing the number of iterations effectively improves the resolution of the phase retrieval.

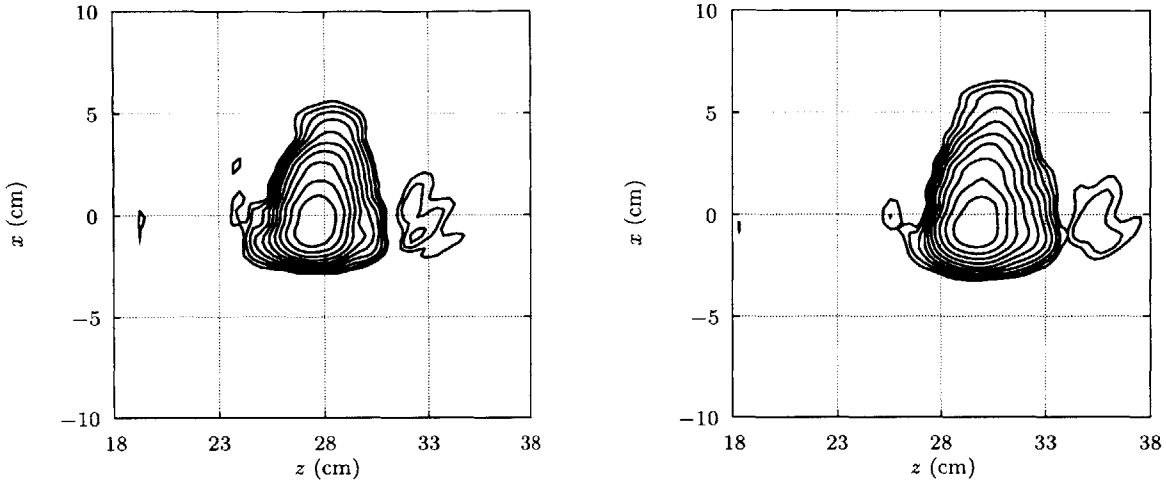

(a) $y = 11$ cm

(b) $y = 16$ cm

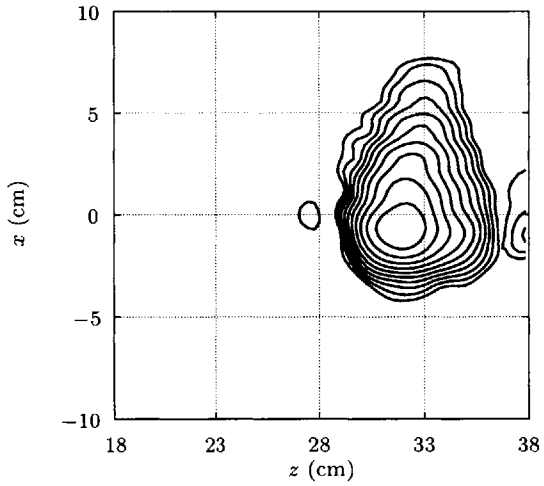

(c) $y = 21$ cm

Figure 2-15: Simulated field intensity at $y = 11$ cm, $y = 16$ cm, and $y = 21$ cm used to reconstruct the field inside the mode converter. Contours of constant $|E_x|^2$ are at 3 dB intervals from peak.

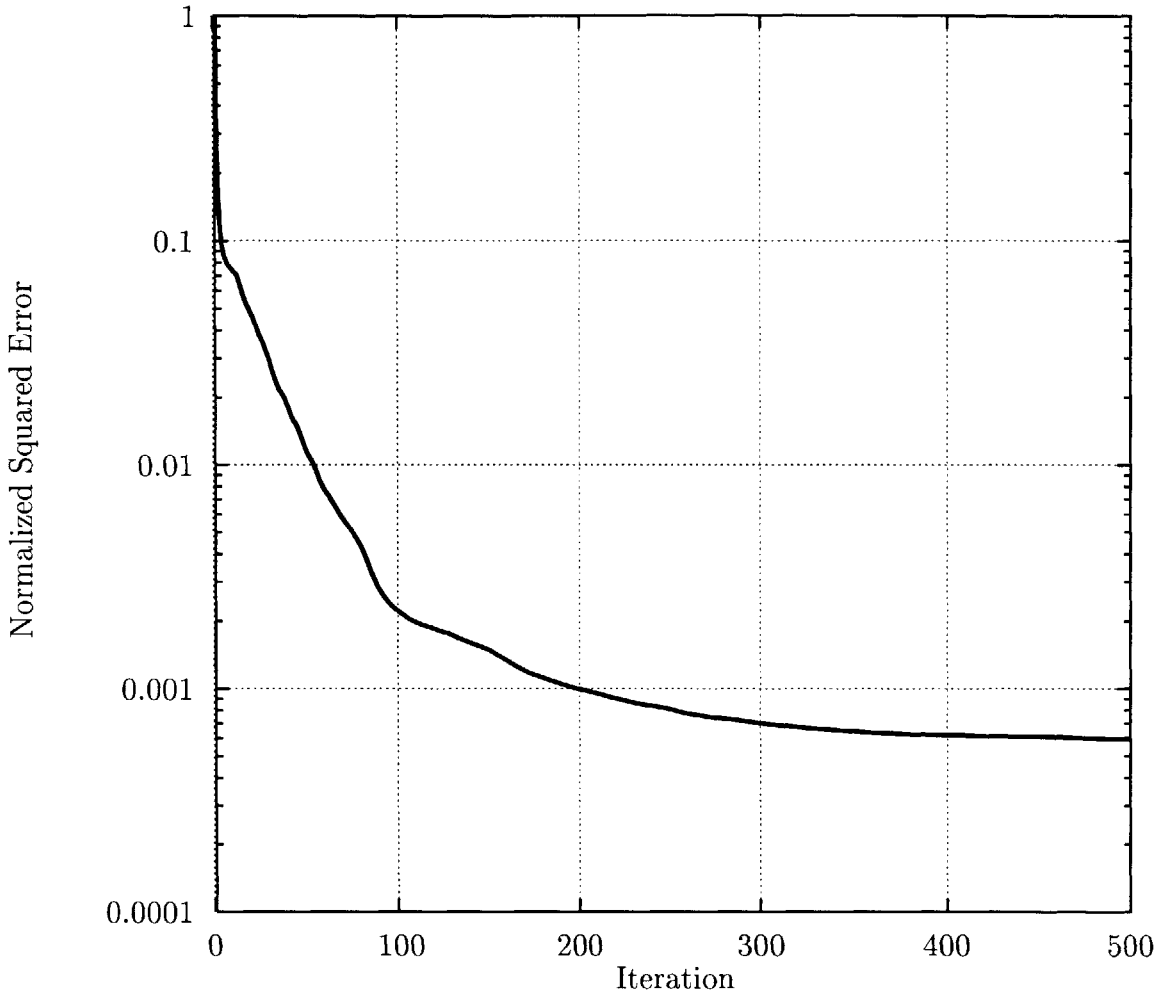

Figure 2-16: Normalized squared error as a function of iteration number for the case of retrieving phase from three simulated intensities at $y = 11$ cm, $y = 16$ cm, and $y = 21$ cm.

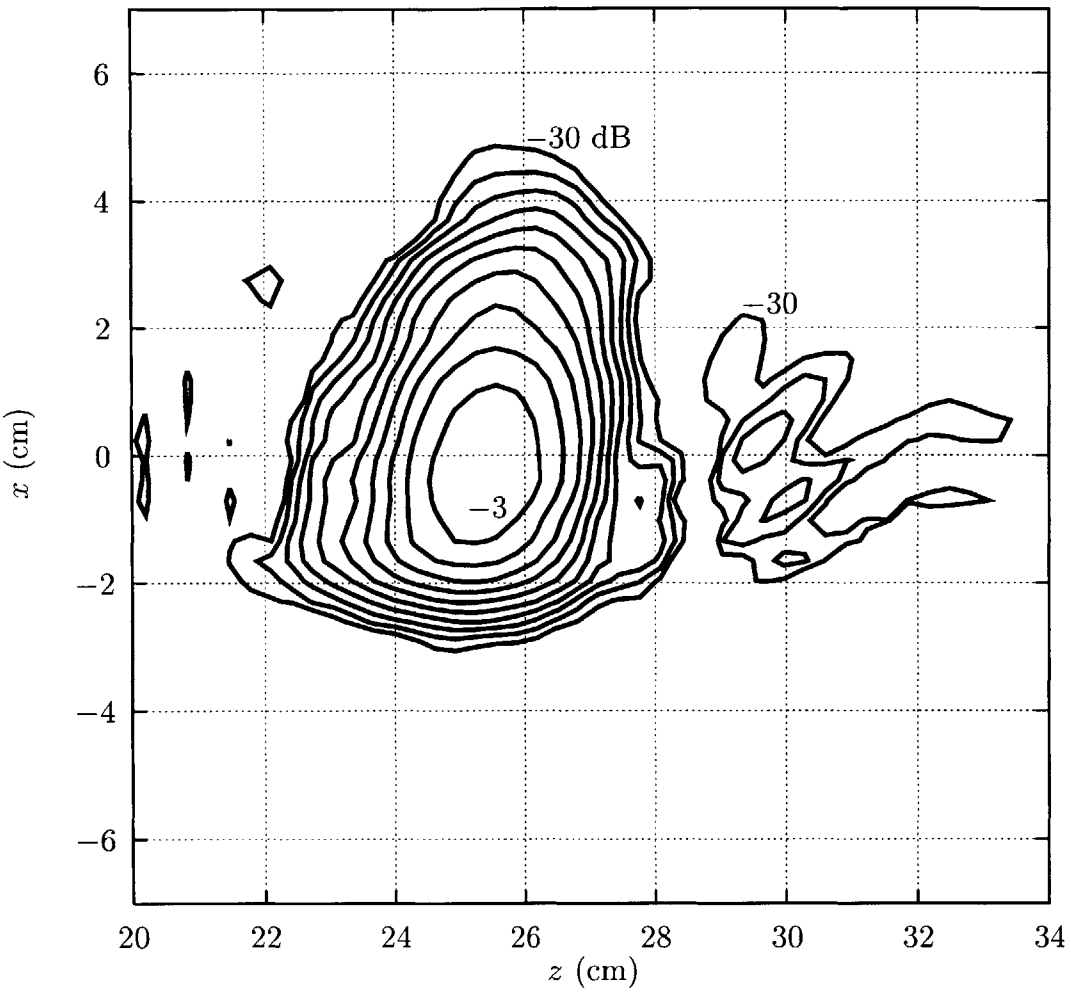

Figure 2-17: Given field intensity profile at $y = 6$ cm. Contours of constant $|E_x|^2$ are at 3 dB intervals from peak; the -3 dB and -30 dB curves are labeled.

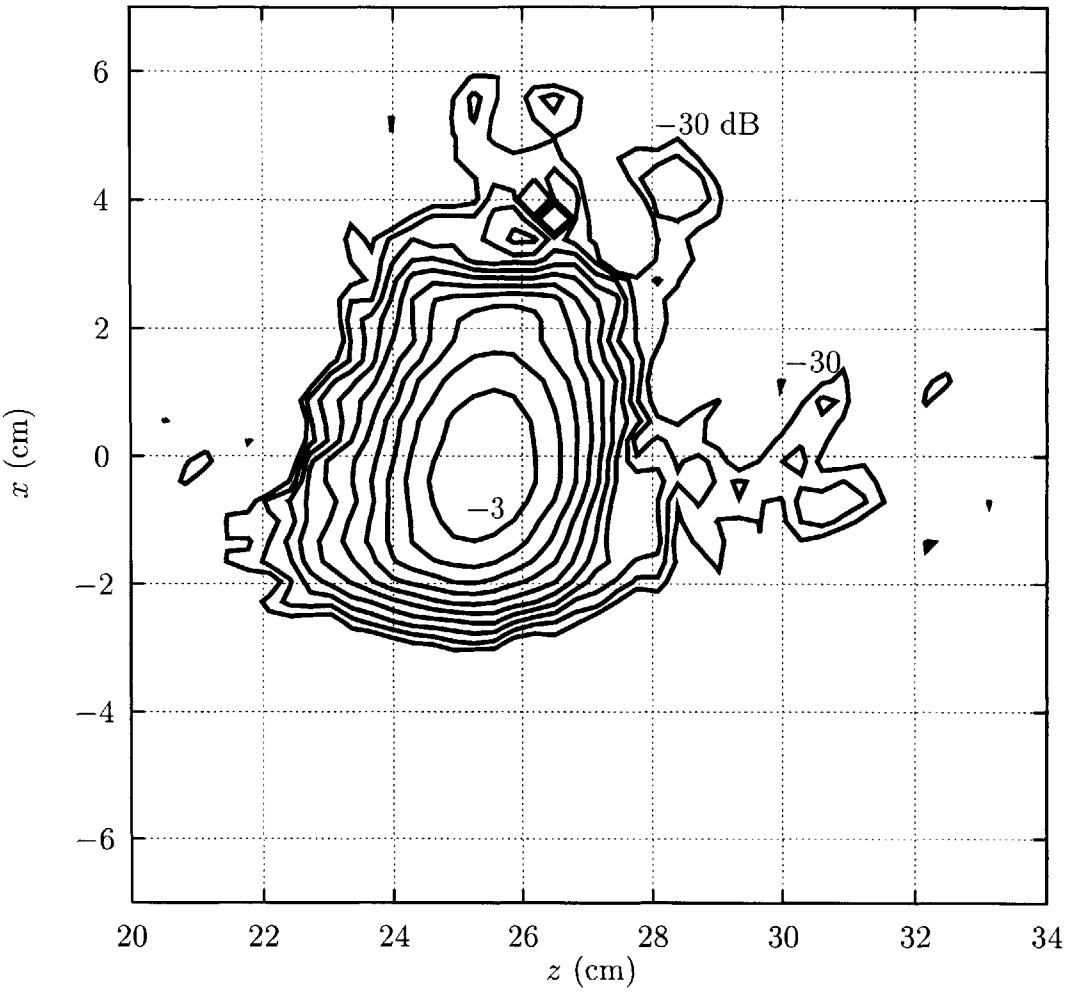

Figure 2-18: Reconstructed field intensity profile at $y = 6$ cm from given intensities at $y = 11$ cm, $y = 16$ cm, and $y = 21$ cm after 100 iterations. Contours of constant $|E_x|^2$ are at 3 dB intervals from peak; the -3 dB and -30 dB curves are labeled.

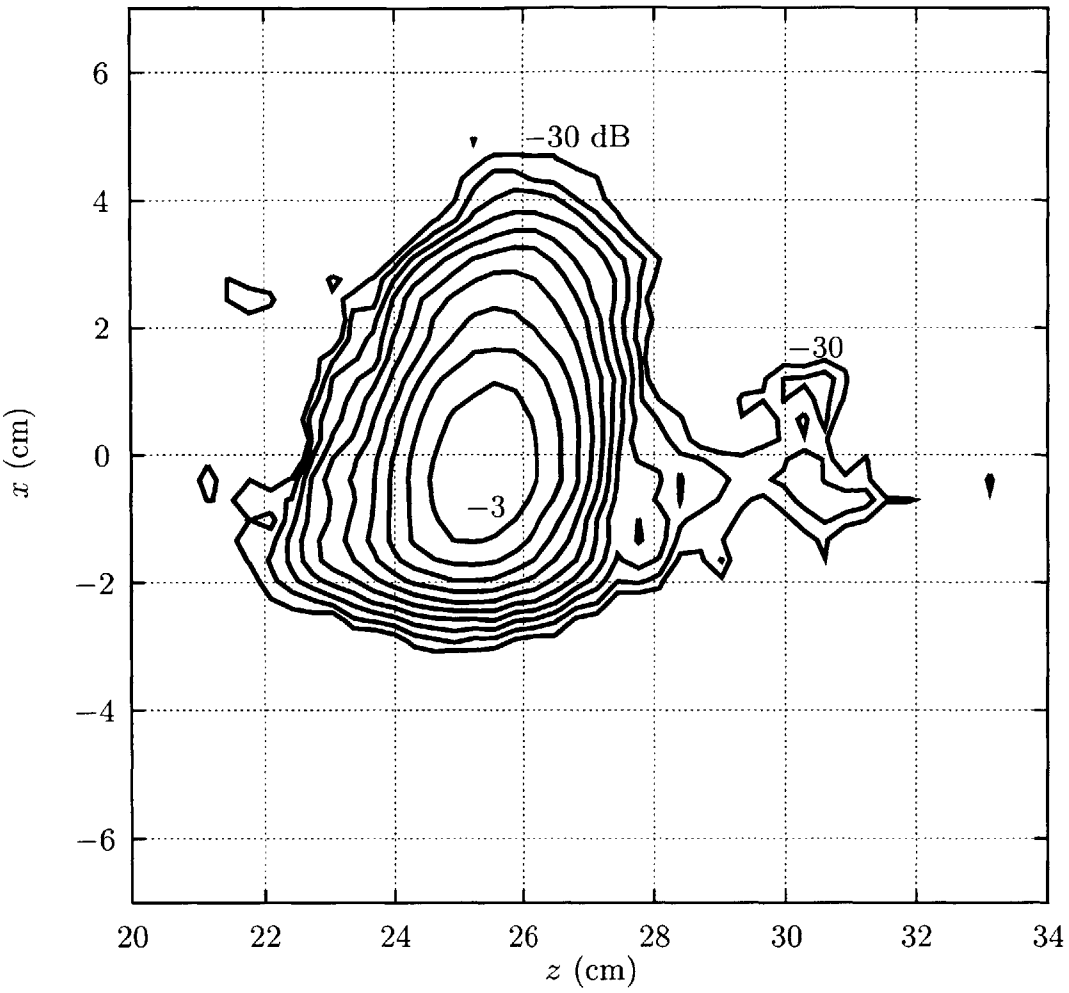

Figure 2-19: Reconstructed field intensity profile at $y = 6$ cm from given intensities at $y = 11$ cm, $y = 16$ cm, and $y = 21$ cm after 500 iterations. Contours of constant $|E_x|^2$ are at 3 dB intervals from peak; the -3 dB and -30 dB curves are labeled.

2.5 Discussion

In developing the phase retrieval algorithm and its numerical implementation, this chapter has formed the foundation for all of the work that follows. The mechanics of the algorithm involving amplitude replacement and wave propagation via plane wave expansion are reasonably straightforward, but these operations also have wide implications on the understanding and applicability of the algorithm. We can gain greater insights into the phase retrieval algorithm by examining the computational examples given above in terms of the amplitude replacement and plane wave expansion.

One interpretation of the amplitude replacement at each iteration step is that of a weighting. This process is clearly evident from the discussion in Section 2.2.2, where we observed that the amplitude replacement moves the computed wave solution towards the actual solution. In essence, the measured amplitude values are used to weight the computed solution such that the computed phase and measured amplitude on the different measurement planes together form a solution to the wave equation.

An implication of this weighting along with the imposition of the plane wave expansion (i.e., forcing the amplitude and phase to satisfy the wave equation) is that the phase retrieval algorithm will always attempt to find a solution such that the computed amplitude values match the measured amplitude values and that satisfies the wave equation. This property is equivalent to the error minimization discussed in Section 2.2.2 and means that even in the case of non-physical amplitude values (for instance, where the measurements have been corrupted by noise), the algorithm will find a solution that satisfies the wave equation while having an amplitude as close as possible to the measured values. We can see that this behavior of the algorithm permits a solution while raising questions about the meaning and uniqueness of that solution.

The uniqueness and attainment issues are poorly-understood aspects of the iterative phase retrieval algorithm. The lack of a closed-form expression makes it difficult to apply analytic arguments to this inherently-numerical procedure, and the addition of noise further obscures any general statements about the analytic properties of the algorithm. We can also see immediately from a thought example that our choice of initial phase can influence the solution. Consider for instance two planes with Gaussian intensity distributions of different waist sizes. One beam that yields these two intensity distributions will have a focus that lies beyond the two planes, while the other beam has a focus between the two planes. (Two solutions are not always possible since one may be entirely non-physical, such as where the beam waist is

required to be on the order of a wavelength, but there is certainly a very broad class of intensity distributions that will admit two meaningful solutions.) This ambiguity is a consequence of the quadratic nature of the Gaussian waist, (2.13), and the final beam produced by the phase retrieval algorithm will depend on the choice of initial phase. We can, of course, distinguish between the two solutions with the addition of another measurement plane.

The only solid conclusion we can draw about the numerical iterative phase retrieval from real measurements, with their discrete representation and noise restrictions, is that the algorithm will try to solve the wave equation with the given amplitudes. We can infer then that the final solution may not be the exact wave that exists in our experiment, but it will be a wave that is perturbed from the actual wave by an amount dependent on the severity of measurement error. Our proposal to use an independent plane at a location z_{obs} to check the solution is the only way to guarantee to some extent that the reconstructed wave behaves as the actual wave.

We can empirically understand the weighting, wave solution, and measurement error concepts from the results of Section 2.4.3. There we had an offset measurement plane where the algorithm first appears to converge but then diverges because we have offset the center measurement plane. At the beginning of the iteration cycle, the initial flat phase is roughly adjusted to a spherical phase in order to provide a beam expansion consistent with the increasing radius of the beam as a function of z. Once this initial, gross adjustment is made, the algorithm then starts to fail as it tries to align the (erroneous) center pattern with the two outer planes. At each iteration, the deviation of the center pattern forces a weighting on the propagating beam that is not consistent with the patterns at either end of the measurement space. This weighting, while valid on the center plane, essentially violates the assumptions in the convergence proof of Section 2.2.2 by forcing the measured amplitudes on the end planes to not be the closest values of the consistent solution.

The inability of the algorithm to converge on a solution for severely corrupted data, as we showed in Section 2.4.3 for the case of a uniform displacement, does not necessarily mean that we do not arrive at a solution, and in fact we showed that the solution may even be acceptable. This observation amounts to noting the basic robustness property of the iterative phase retrieval algorithm that arises because at each iteration we replace the computed amplitudes with the measured values. In doing so, we prevent the algorithm from running away or producing a nonsense solution. In fact, as discussed above, we find *a* solution that tries to get as close to the measured amplitudes while still satisfying the wave equation.

In addition its conceptual importance, the plane wave expansion affords rapid and efficient computation with the FFT. Our studies of simulated data indicate that overcoming the plateaus in the convergence corresponds to improving the resolution of fine details of the field structure, particularly at low intensity. Additionally, the convergence of the solution depends on the distance between measurement planes, with larger plane separations improving the rate of convergence. However, if the beam changes significantly over a relatively short distance, as in our mode converter example, then the measurement data still contain sufficient information for the phase retrieval, at the expense of needing more iterations. Given these factors, the ability to perform many (100 – 1000) iterations, made feasible by our implementation of the phase retrieval algorithm, is crucial to obtaining an accurate field reconstruction.

Chapter 3

Mirror Surface Shaping

In Section 1.3 we introduced the concept that the launcher and first two reflectors in the mode converter constitute a feed in a conventional offset-fed, dual-reflector antenna. Extending this analogy, we can view the shaping of reflectors three and four as the general problem of beam synthesis in antenna design — given a specified feed, shape the reflectors to produce the desired output beam. In this chapter, we treat the problem of forming mirrors in terms of phase correcting surfaces as an extension of the phase retrieval technique from Chapter 2. The necessary transformations from a phase surface to a real surface are derived, and an internal mode converter example is presented that verifies the mirror shaping approach.

3.1 Formulation

The concept of using a pair of shaped reflectors (or mirrors) to transform an arbitrary incident field into a given radiated field was first analyzed by Kinber [19] and Galindo [20]. They treated this synthesis problem in terms of wave propagation path length and energy conservation, and they showed that an exact solution for the case of circularly symmetric reflectors exists as a set of non-linear ordinary differential equations. Later, Galindo-Israel, *et al.* [21] showed that, for a very wide class of problems, solutions also exist for the off-set fed geometry. These ray optic methods of reflector synthesis have since found application in a broad range of fields, including shaping techniques for gyrotron mode converter mirrors [6].

An alternate approach to shaping the mirrors is to treat them as phase-correcting surfaces; that is, the polarization and amplitude of the incident wave is assumed to remain unchanged upon reflection while the phase is modified. This approximation holds for a wide class of quasi-optical microwave engineering problems — the design of

mirrors, lenses, and resonators in Gaussian optics relies heavily on modeling elements as phase correctors (e.g. [5]). An advantage of this treatment is that we can use the phase retrieval algorithm described in Chapter 2 to define the phase correcting surfaces [22, 23, 24], unifying our design approach under a single construct.

To see the relationship between phase retrieval and mirror shaping, consider the geometry of Figure 3-1. The two phase-correcting surfaces are cast as equivalent thin lenses with phase-correcting functions $\Delta_1(x,y)$ and $\Delta_2(x,y)$. The beam is propagating along the z-axis, perpendicularly to each lens surface. The incident beam is denoted as $A_1(x,y)e^{i\phi_1(x,y)}$ and the desired output beam is $A_2(x,y)e^{i\phi_2}$. We see that the amplitudes $A_1(x,y)$ and $A_2(x,y)$ may be associated through the pair of self-consistent phases $\phi_1^{sc}(x,y)$ and $\phi_2^{sc}(x,y)$, which are determined by applying the phase retrieval algorithm to $A_1(x,y)$ and $A_2(x,y)$. Then the phase correcting function required to transform the incident phase, $\phi_1(x,y)$, into the first self-consistent phase, $\phi_1^{sc}(x,y)$, is given by

$$\Delta_1(x,y) = \phi_1^{sc}(x,y) - \phi_1(x,y). \tag{3.1}$$

Similarly for the second phase-correcting function we have

$$\Delta_2(x,y) = \phi_2(x,y) - \phi_2^{sc}(x,y). \tag{3.2}$$

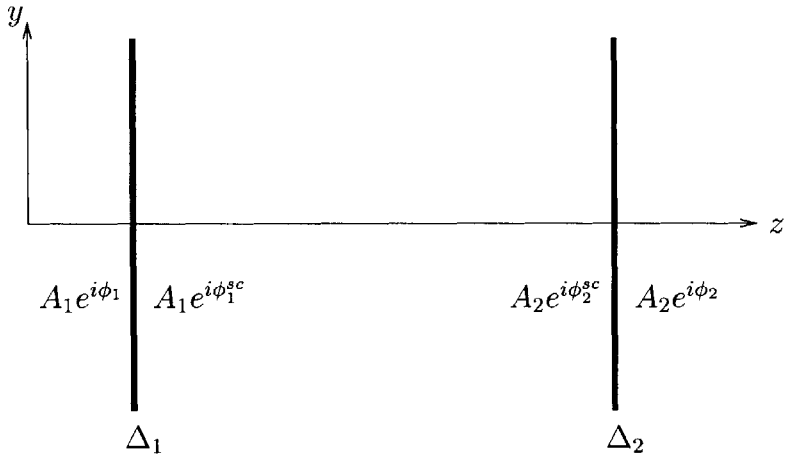

Figure 3-1: Geometry for the mirror shaping procedure.

In the above procedure we see that the first phase corrector transforms the incident phase such that the beam amplitude at the second phase corrector will be the desired output amplitude, $A_2(x,y)$, and the second corrector synthesizes the desired output phase. An interesting consequence of this observation is that we can produce

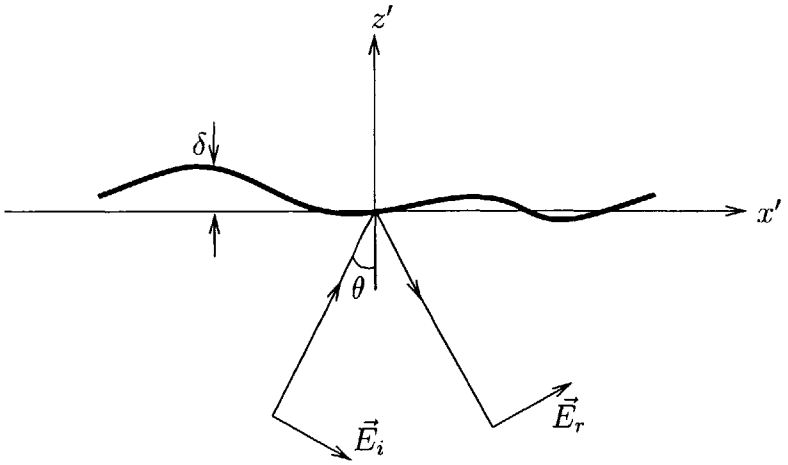

Figure 3-2: Wave incident on a weakly-perturbed surface.

a specified beam intensity, but not phase, using only one mirror. This situation is related to basic Gaussian optics where we can use a single spherical mirror or lens to transform a Gaussian beam into either a beam with a specified waist size or with a specified minimum waist position (focal length), but not both.

3.2 Transforming Phase to a Real Surface

The phase corrector function $\Delta(x, y)$ derived above must be transformed into a real mirror surface to complete the mirror shaping procedure. Before attempting to define the mirror profile, we first need to unwrap the phase to remove 2π discontinuities. We use a routine that reads the phase difference data file along each coordinate, detects phase changes greater than π, and adjusts the phase based on the previous value if a jump in the phase is detected. This approach works well, but it does fail in regions where the phase variation is essentially random; i.e., where the amplitude of the wave is small enough to render the phase indeterminate.

To see how we can define the mirror surface shape in terms of the phase corrector function $\Delta(x, y)$, consider the geometry shown in Figure 3-2. A wave is propagating in the $+z'$ direction and is incident on a conducting surface whose profile is weakly-perturbed from a perfectly flat surface by the amount $\delta(x', y)$. (Our introduction of primed coordinates serves to distinguish the current Cartesian geometry from that where the z-axis is oriented parallel to the beam propagation direction.) The incident

and reflected electric fields can be written

$$\vec{E}_i(x', z') = E_0 \left(\hat{x}' \cos\theta - \hat{z}' \sin\theta\right) e^{ikx' \sin\theta} e^{ikz' \cos\theta} \tag{3.3}$$

$$\vec{E}_r(x', z') = RE_0 \left(\hat{x}' \cos\theta + \hat{z}' \sin\theta\right) e^{ikx' \cos\theta} e^{-ikz' \cos\theta}, \tag{3.4}$$

where R is the reflection coefficient. Continuity of tangential electric field on the conducting surface at $z' = \delta(x', y)$ requires

$$E_0 \hat{x}' \cos\theta e^{ik\delta \cos\theta} e^{ikx' \sin\theta} = -RE_0 \hat{x}' \cos\theta e^{-ik\delta \cos\theta} e^{ikx' \sin\theta}, \tag{3.5}$$

which gives $R = -\exp(i2k\delta\cos\theta)$. Physically, this result arises because the incident wave undergoes a phase shift that is proportional to the total distance traveled by the wave. We can then immediately write our phase-corrector function in terms of the mirror depth δ:

$$\Delta = 2k\delta\cos\theta. \tag{3.6}$$

At this point, however, the above expression is partly heuristic; we have not accounted for the fact that in deriving our phase difference function Δ we assumed normal incidence. A complete expression for transforming the phase corrector function to real space must include a coordinate rotation. Manipulating (3.6) and adding the appropriate rotation around the y-axis (into the page in Figure 3-2) gives the mirror surface profile depth as

$$\delta(x', y) = \frac{\Delta(x'\cos\theta, y)}{2k\cos\theta}. \tag{3.7}$$

Using this expression, we can define a real mirror surface from the phase corrector function. For a preliminary test of this mirror shaping routine, we present next a design study based on simulated data.

3.3 A Mirror Shaping Example: 110 GHz Gyrotron Internal Mode Converter

Consider the gyrotron internal mode converter shown in Figure 1-3. We want to shape mirrors three and four (M3 and M4 in Figure 1-3) to transform the wave incident on mirror three into a Gaussian beam at the gyrotron window. Once we have generated our mirror surfaces, we can use the physical optics code described in Section 2.4.4 to validate the design.

The simulated field intensity at the surface of mirror three was previously shown

in Figure 1-8, and we presented a detailed discussion of these theoretically-predicted fields in Section 2.4.4. We note that the fields incident on mirror three are strongly polarized in the x-direction (into the page in Figure 1-3), with a cross-polarization term that is two orders of magnitude smaller than the main polarization. This dominant linear polarization is thus consistent with our scalar formulation. To shape the mirrors according to the procedure described in Section 3.1, we use this simulated field intensity as our incident intensity, A_1, on the first phase-correcting surface. Here we have dropped the explicit variable dependence in the function A_1; to avoid confusion between the three possible coordinate systems (the wave, the mirror plane, and the mode converter coordinate systems) we will only use the mode converter coordinate system in presenting the results.

For the intensity profile A_2 on the second corrector (mirror four), we first specify that the radiated field on the gyrotron window should be a Gaussian beam with a minimum waist radius w_0 of 1.5 cm, and that the waist should occur at the window plane. Given this waist size and position, we can find the desired intensity and phase at the surface of the fourth mirror (located approximately 40 cm from the output window) with the analytic expression for a Gaussian beam (2.12).

With the given field intensity profiles A_1 and A_2, the self-consistent phases can be determined using the phase retrieval algorithm, and each phase correcting surface is derived from (3.1) and (3.2). Expression (3.7) then transforms the phase differences into actual mirror surfaces, where the incidence angle θ for the first shaped mirror (mirror three) is 23° and for the second shaped mirror (mirror four) is 13°. The final surface profiles are shown in Figure 3-3.

Figure 3-3(a) shows the surface profile of the first shaped mirror (mirror three) with the wave is incident from below. (The rough edges are inconsequential and result from an indeterminate phase in that low-intensity region.) We see that this mirror has a nearly-flat surface with curvature at the $+x$ end of the mirror to focus the oblong beam of Figure 1-8 into a circular Gaussian beam. The wave is incident from above in Figure 3-3(b), and it sees the largely spherical surface of the second shaped mirror that transforms the wave from the first shaped mirror into the desired Gaussian beam with a spherical phase front.

These mirror profiles were simulated in the physical optics code described in Section 2.4.4 to independently verify the design. The fields on mirror two in the mode converter were radiated to the surface of mirror three, and the resulting surface currents were then used to radiate the field from mirror three to mirror four. The resulting simulated electric field intensity on mirror four is shown in Figure 3-4. We

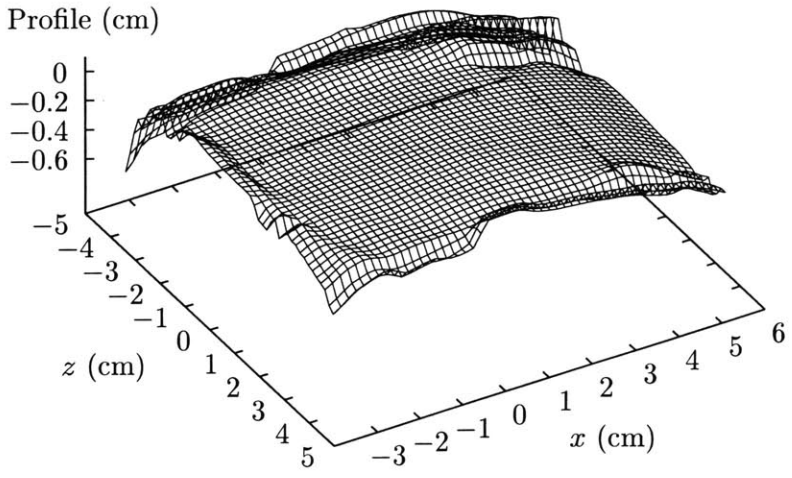

(a) First shaped mirror (mirror 3) surface profile.

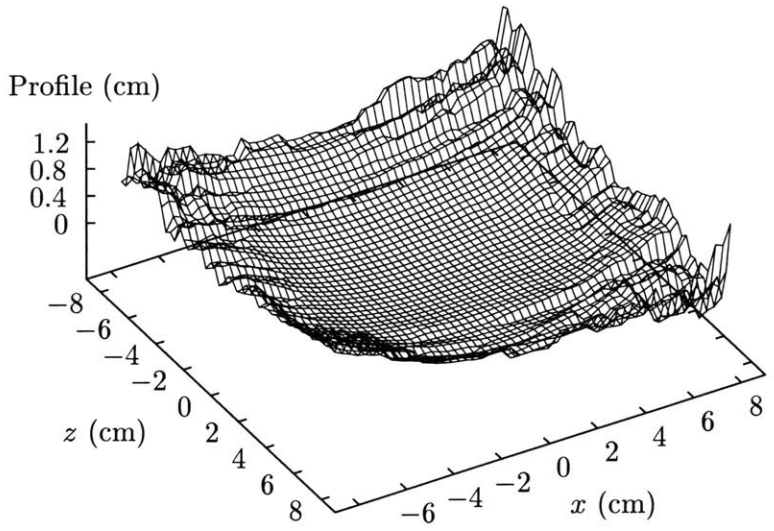

(b) Second shaped mirror (mirror 4) surface profile.

Figure 3-3: Shaped mirror profiles for the internal mode converter designed from simulated fields. The profile depth scale has been exaggerated for contrast.

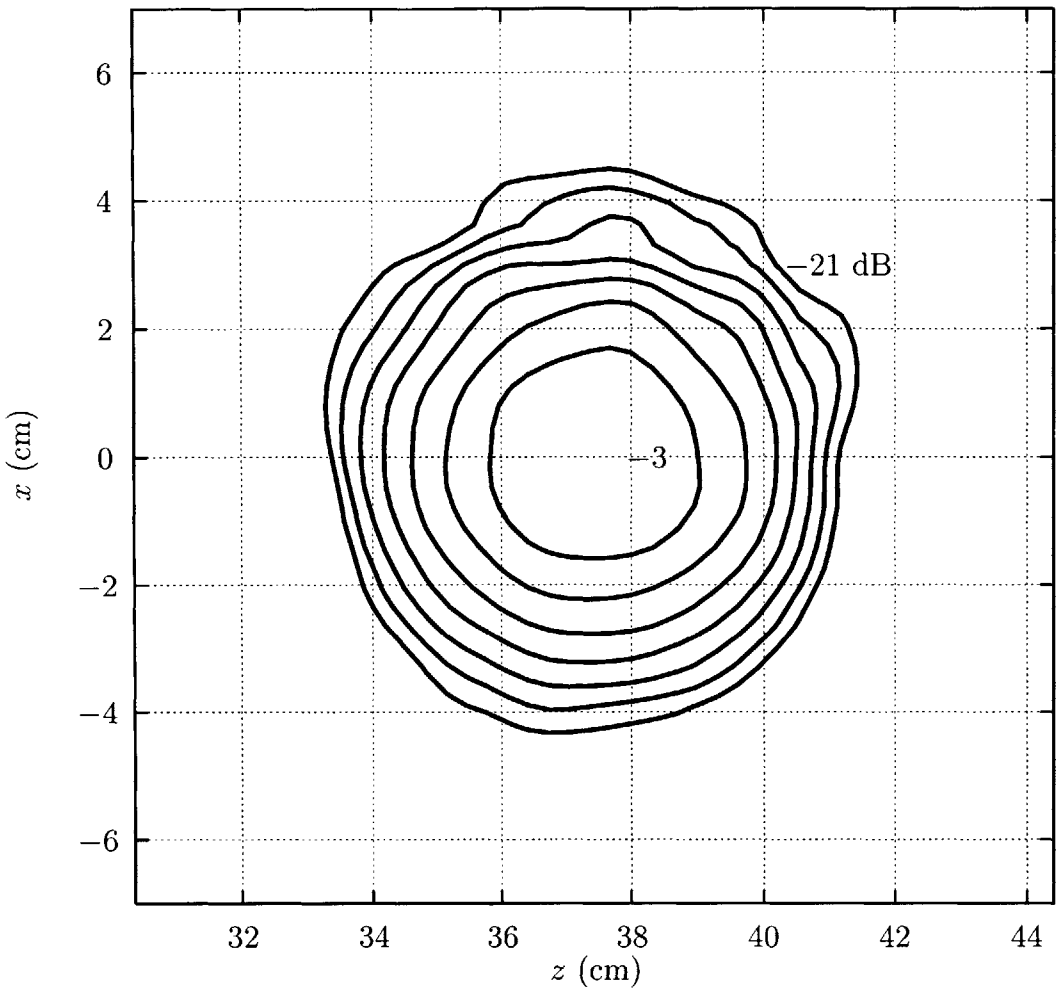

Figure 3-4: Simulated field intensity on the surface of the second shaped mirror (mirror four). Contours of constant $|E_x|^2$ are at 3 dB intervals from peak; the -3 dB and -21 dB curves are labeled.

see that, as discussed at the end of Section 3.1, the first shaped mirror (mirror three) has produced a beam with a Gaussian-like intensity profile at the surface of the second shaped mirror (mirror four). The phase of this field is then modified by the mirror four surface to produce a Gaussian beam at the output window as shown in Figure 3-5.

The beam intensity at the window has a Gaussian profile whose waist size agrees with the design waist size of 1.5 cm. Figure 3-6 shows a cut through the simulated field intensity along the z-axis and compares the simulated intensity to the ideal Gaussian. The phase of the output wave over the 5-cm aperture is given in Figure 3-7, and we see it is flat as designed.

Figures 3-5, 3-6, and 3-7 clearly show that the shaped mirrors produce the desired

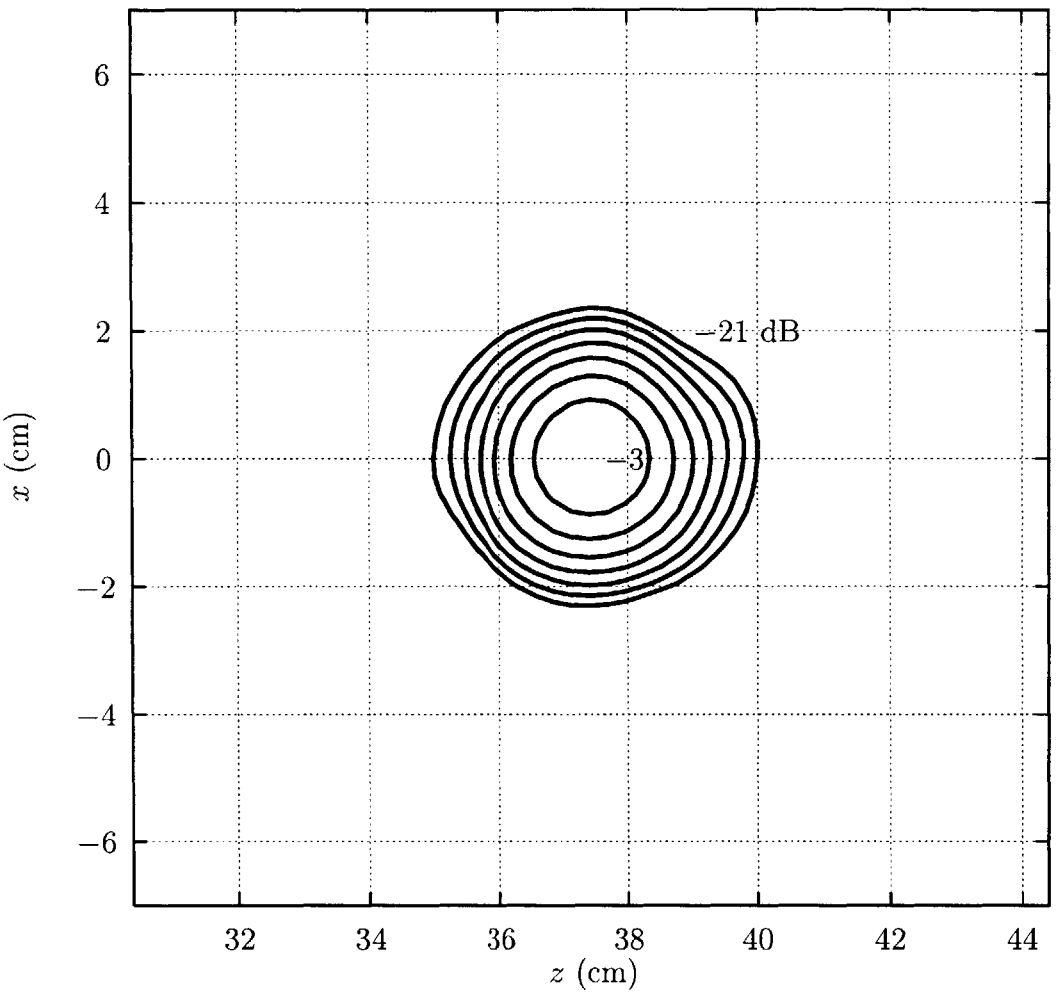

Figure 3-5: Simulated field intensity at the output window plane. Contours of constant $|E_x|^2$ are at 3 dB intervals from peak; the -3 dB and -21 dB curves are labeled.

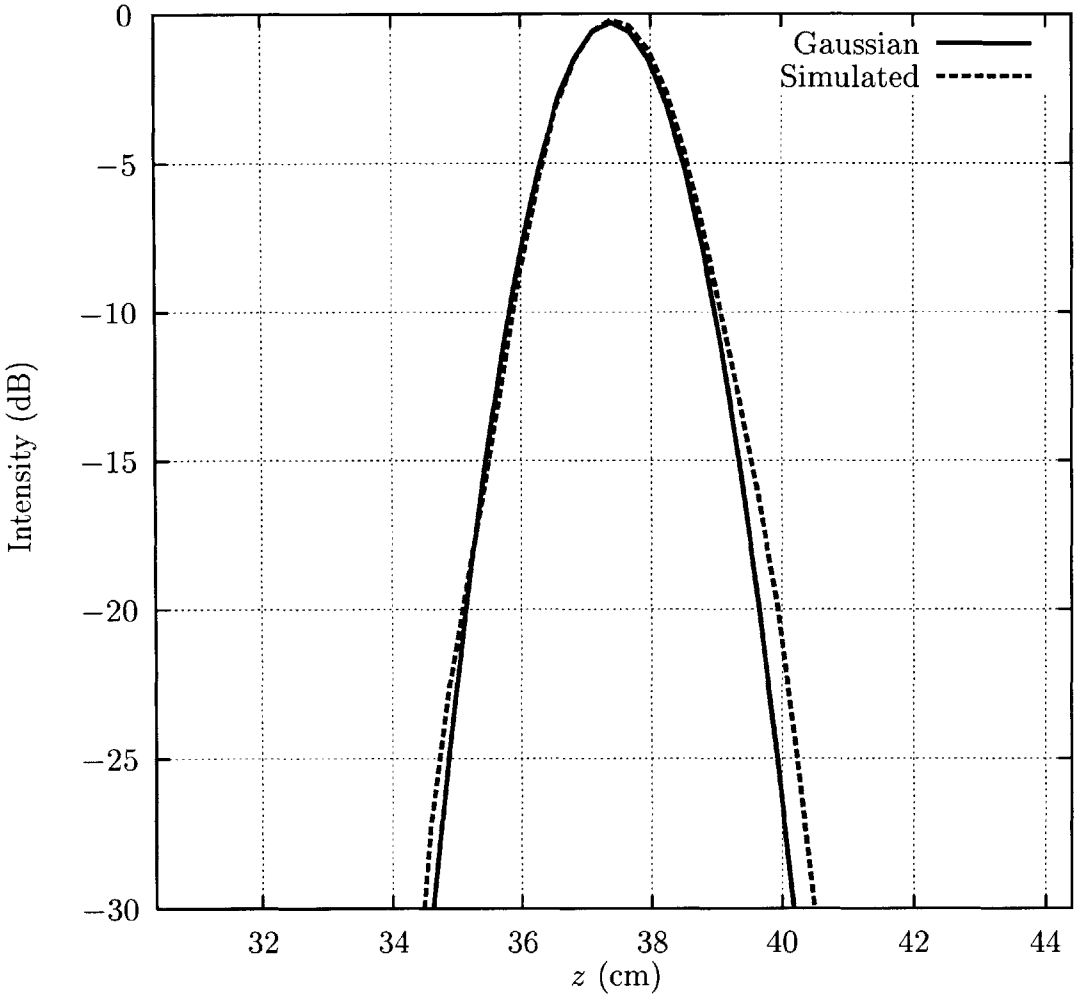

Figure 3-6: Simulated intensity over the window aperture along the z-axis. The window center is located at $z = 37.4$ cm.

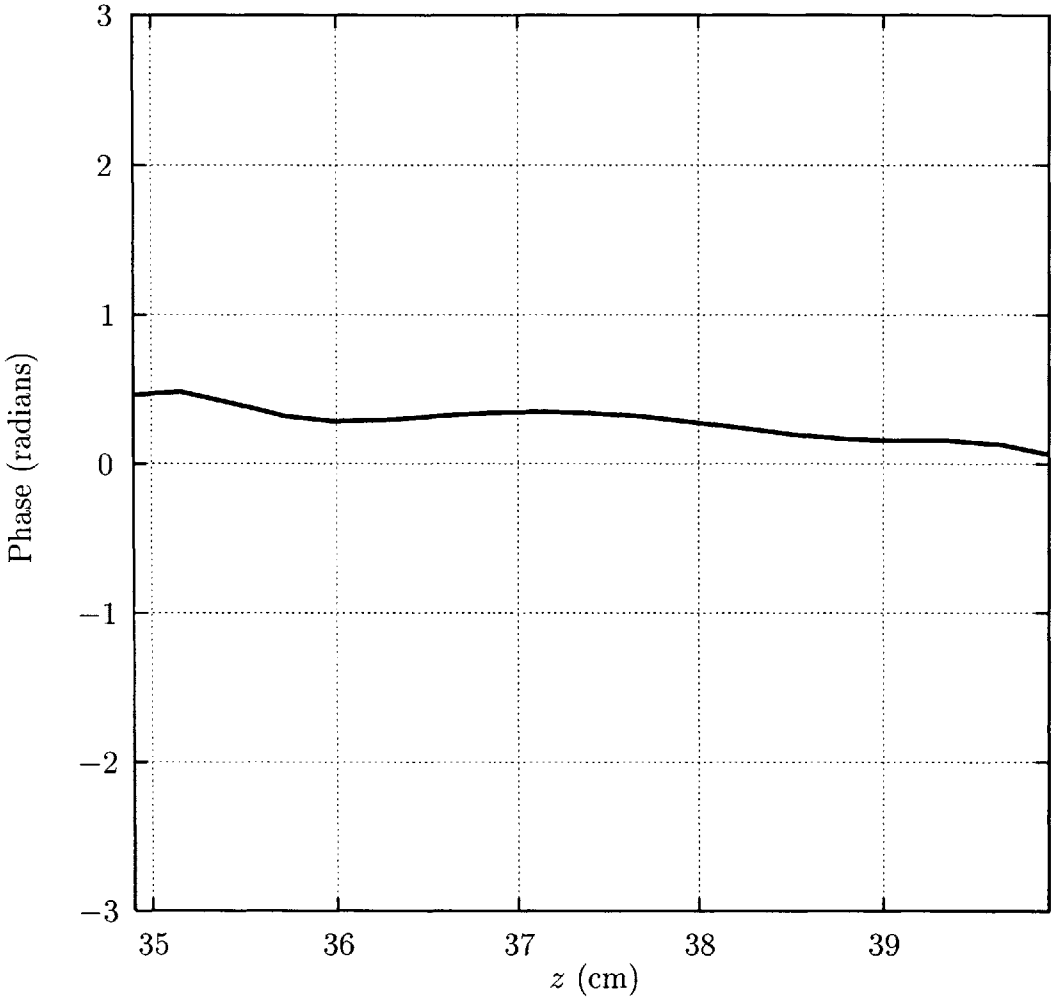

Figure 3-7: Simulated phase over the window aperture along the z-axis.

Gaussian beam — in both amplitude and phase — over the window aperture.

3.4 Discussion

We have presented a method for determining the shapes of a pair of phase-correcting surfaces to transform a given incident wave into a desired output radiation pattern. This phase-corrector approach allows us to use the phase retrieval algorithm in the synthesis problem, thus unifying the overall design approach.

Implicit in our formulation is the assumption that the incident and desired wave amplitudes will lead to a self-consistent phase solution. We know in the case of phase retrieval from intensity measurements that the measurements represent some physical wave that satisfies Maxwell's equations and thus is a solution to the wave equation; for mirror shaping, however, we have *imposed* two possibly-inconsistent amplitude distributions. Indeed, we see from the mode converter mirror design results above that the first shaped mirror does not produce an ideal Gaussian beam intensity profile at the surface of the second shaped mirror, but does produce a beam that is as close to Gaussian as possible while still being a valid wave solution in accord with the discussion at the end of Chapter 2.

Mirror four then transforms this incident wave into the Gaussian beam at the gyrotron window. As we see from the intensity profile at the window (Figure 3-5), the beam is not perfectly symmetric. This asymmetry is a continuing consequence of the above-noted inability of our approach to transform an arbitrary beam into an ideal Gaussian. Nevertheless, we have successfully produced — using only phase correction — a beam with amplitude and phase that are strongly Gaussian. Additionally, the simulated beam waist size and position agree with the specified parameters. These results provide preliminary support for our proposed approach. The next two chapters detail experimental results that further verify the efficacy of the design procedure.

Chapter 4

External Mode Converter Mirror Design: The Matching Optics Unit

In this chapter, we present the design of a pair of mirrors for use in an external mode converter, often called a Matching Optics Unit (MOU). The MOU mirrors will be used to transform the crescent-shaped microwave beam radiated by a 110 GHz gyrotron (discussed in Chapter 1) into a Gaussian beam suitable for injection into a 3.175 cm-diameter corrugated waveguide. The geometry of the MOU is shown in Figure 4-1. To distinguish this particular gyrotron and its accompanying external components from the gyrotron discussed in the next chapter, we will refer to the present gyrotron by its industrial name — S/N4. This gyrotron was built by Communications and Power Industries (CPI), Palo Alto, CA, and installed at General Atomics (GA), San Diego, CA. All of the experimental measurements described below were conducted at GA.

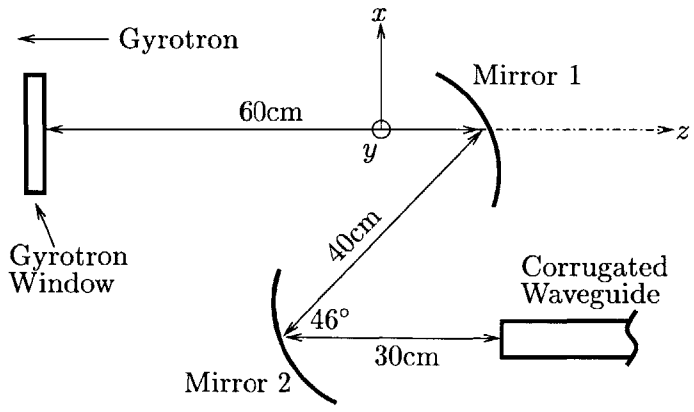

Figure 4-1: Top view of the matching optics unit geometry.

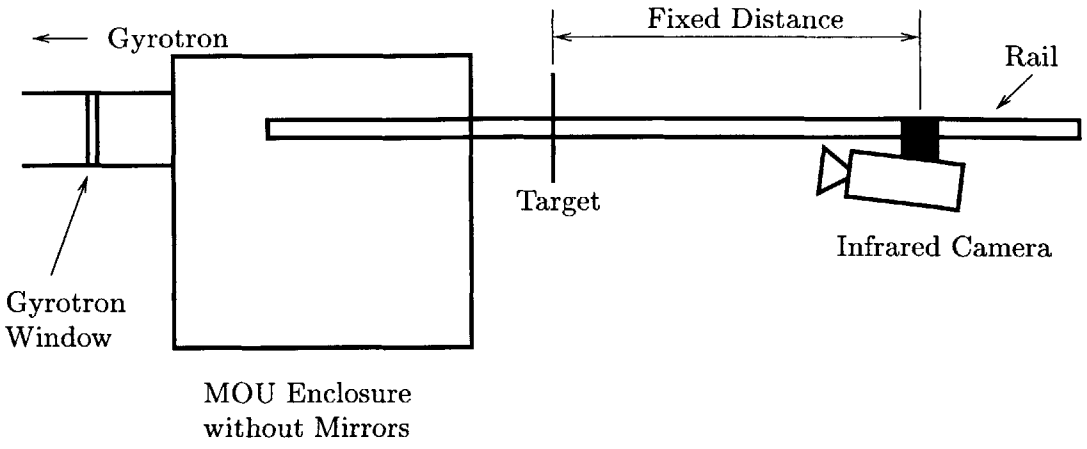

Figure 4-2: Top view of apparatus used for infrared camera measurement of the S/N4 gyrotron output microwave beam.

4.1 Incident Field Intensity Measurements

The mirror design approach outlined in Section 1.3 includes initial steps for shaping the beam radiated by the launcher with a pair of toroidal mirrors; here we skip those steps and begin the design process by measuring the field radiated by the gyrotron for direct use in reconstructing the phase of the wave according to Step 4 in Section 1.3. To make field intensity measurements of this high-power source, we used an Inframetrics SC1000 infrared camera to measure the beam heating profile across a paper target placed in the path of the microwave beam. The camera and target were mounted on a rail and moved in tandem to maintain a constant field-of-view for the camera on the target. To avoid damaging the camera, it was placed off the beam propagation axis. Figure 4-2 shows a schematic diagram of the measurement apparatus.

The gyrotron was operated for 600 μs pulse lengths with a repetition rate of 2.3s and produced several hundred kilowatts of microwave beam power. The infrared camera was controlled by a computer with data acquisition software that recorded multiple images over the duration of a gyrotron pulse. Measurements of the field profile were made at several consecutive planes oriented perpendicular to the direction of propagation of the gyrotron microwave beam. In order to use the measurements in the phase retrieval procedure and to provide a more intuitive graphical representation, all of the infrared camera measurements were converted from degrees Celsius to dB by subtracting a background temperature (determined as an average of the temperature data values lying within some ambient-temperature range) and normalizing the data

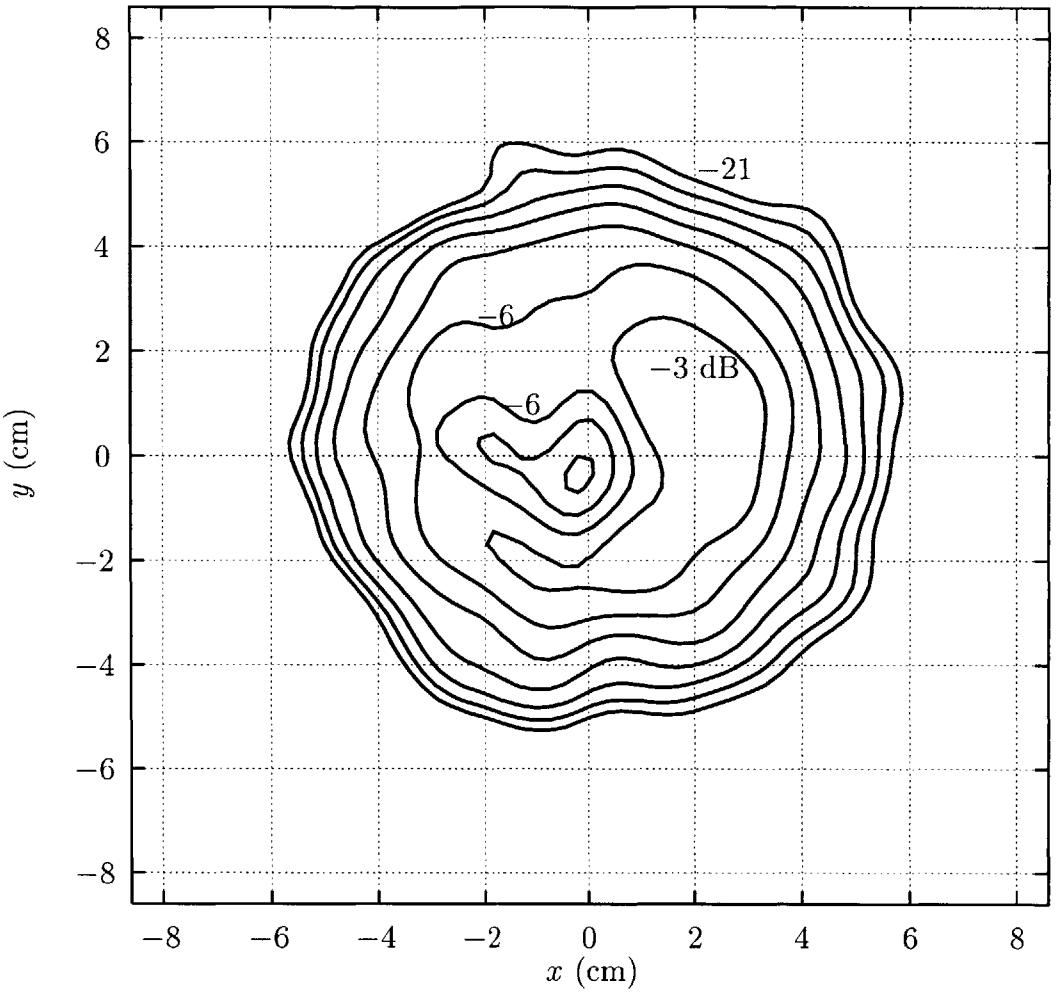

Figure 4-3: Measured field intensity on a plane located 34.6 cm from the gyrotron window. Contours of constant $|E_x|^2$ are at 3 dB intervals from peak; the -3 dB, -6 dB, and -21 dB curves are labeled.

to the peak temperature value on a given plane. The data were also smoothed to remove high-frequency pixel noise. A representative measurement is given in Figure 4-3, which shows the field intensity profile on a plane located 34.6 cm from the gyrotron window. Figure 4-4 likewise gives the measured intensity profile 99.6 cm from the window.

From these two figures, we can see that the crescent-shaped pattern at 34.6 cm from the window evolves into a beam with a dominant Gaussian component and a smaller beamlet, as evident at 99.6 cm in Figure 4-4. This field behavior implies that the beam exiting the gyrotron has a Gaussian component with modest amounts of power in higher-order modes. Since our phase retrieval approach is known to work well for Gaussian beams, we can expect good phase retrieval from these data. Also,

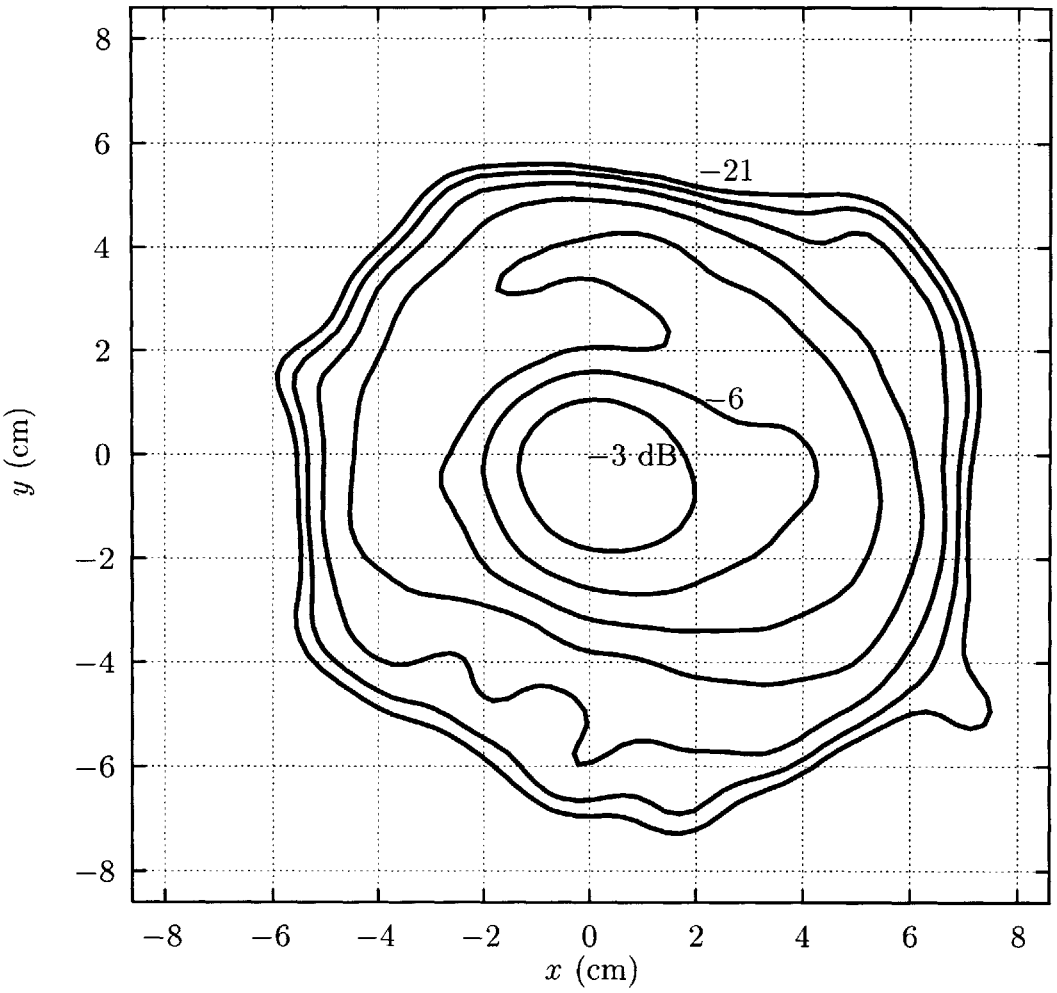

Figure 4-4: Measured field intensity on a plane located 99.6 cm from the gyrotron window. Contours of constant $|E_x|^2$ are at 3 dB intervals from peak; the −3 dB, −6 dB, and −21 dB curves are labeled.

the measurement planes are separated by 65 cm, or 240λ, and they have sufficiently different field patterns to permit an accurate field reconstruction per our discussion in Section 2.5.

4.2 Phase Retrieval and Mirror Shaping

The measured field intensities at 34.6 cm and 99.6 cm were used in the phase retrieval algorithm to reconstruct the field structure of the gyrotron output beam. The data were spaced over a 128-point $\times$ 128-point square grid with a side length $L = 17.2$ cm. The initial phase guess was a flat phase, and 125 iterations were necessary to reconstruct the phase of the beam. The reconstructed field was then propagated to the position of the first mirror at 60 cm from the gyrotron window for use as the incident field in the mirror shaping procedure. This computed incident field is shown in Figure 4-5.

We can check the accuracy of the reconstruction by comparing the computed fields at the first mirror plane with the measured fields at 64.6 cm given in Figure 4-6. Although this measurement plane is located 4.6 cm beyond the mirror plane, it is adequate for comparison because the beam does not evolve appreciably over the 17λ distance between the two planes. However, we note that the measured data in Figure 4-6 have been corrupted by heat rising on the target. This effect is apparent from the smearing of the contour curves in the upper half plane for intensity values less than -9 dB. Further evidence of this corruption comes from contrasting this measurement to those at 34.6 cm and 99.6 cm (Figures 4-3 and 4-4, respectively). On those two planes, the curves are nearly circular and do not exhibit the elongation in the $+y$-direction at the 64.6 cm plane. Such an elongation would require the beam to spread and then contract as it propagates from 34.6 cm to 99.6 cm, which is a non-physical beam behavior.

The primary source of this measurement error was a lack of adequate triggering of the camera in sync with the gyrotron pulse. The infrared camera software took images of the target equally spaced in time with no reference to when the microwave beam actually existed. A delay on the order of milli-seconds (the pulse length is < 1 ms) is sufficient to allow conduction of heat through the paper target and also convection across the target surface. The final data were chosen as the best from the available set, but this essentially random process proved unsatisfactory. Future infrared camera measurements, including those of the final output beam presented in Section 4.3, benefit greatly from a synchronized trigger, and do not suffer from the

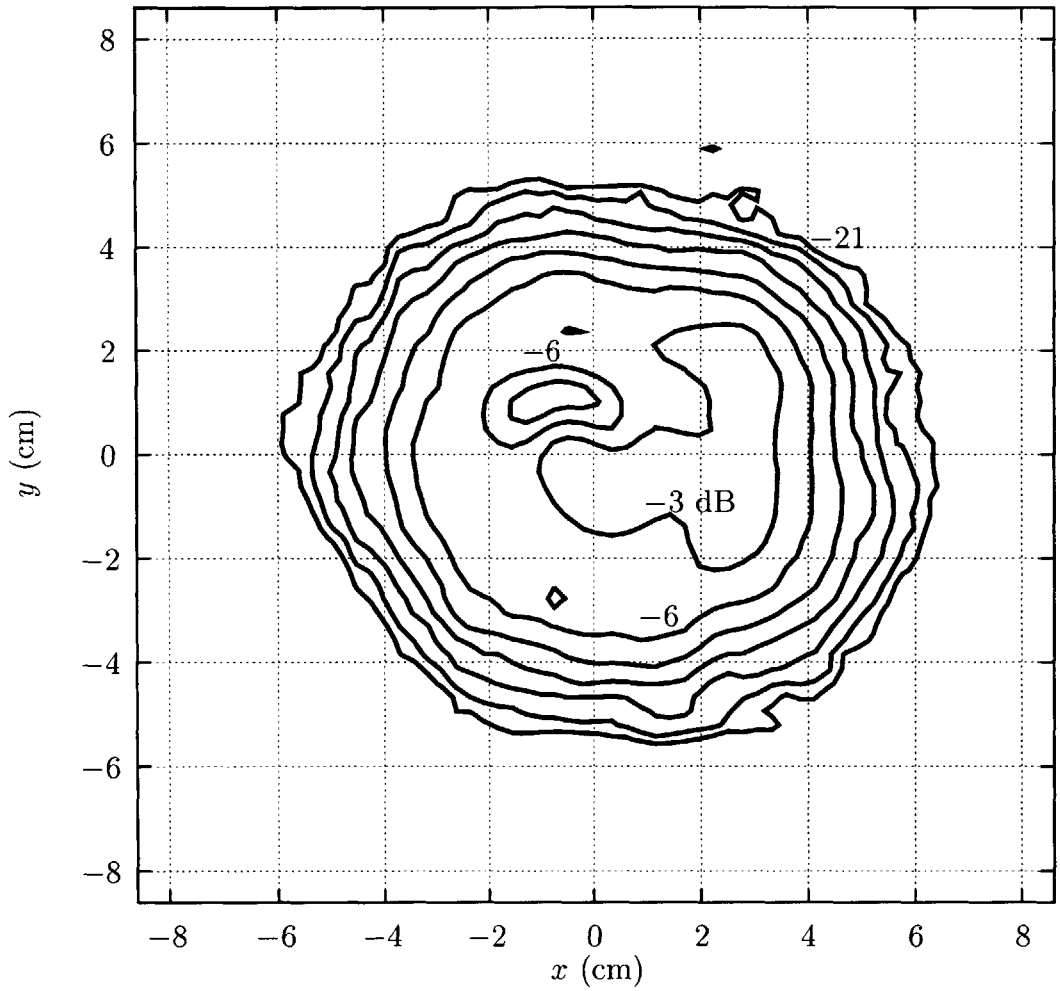

Figure 4-5: Simulated field intensity on a plane located 60 cm from the gyrotron window. Contours of constant $|E_x|^2$ are at 3 dB intervals from peak; the −3 dB, −6 dB, and −21 dB curves are labeled.

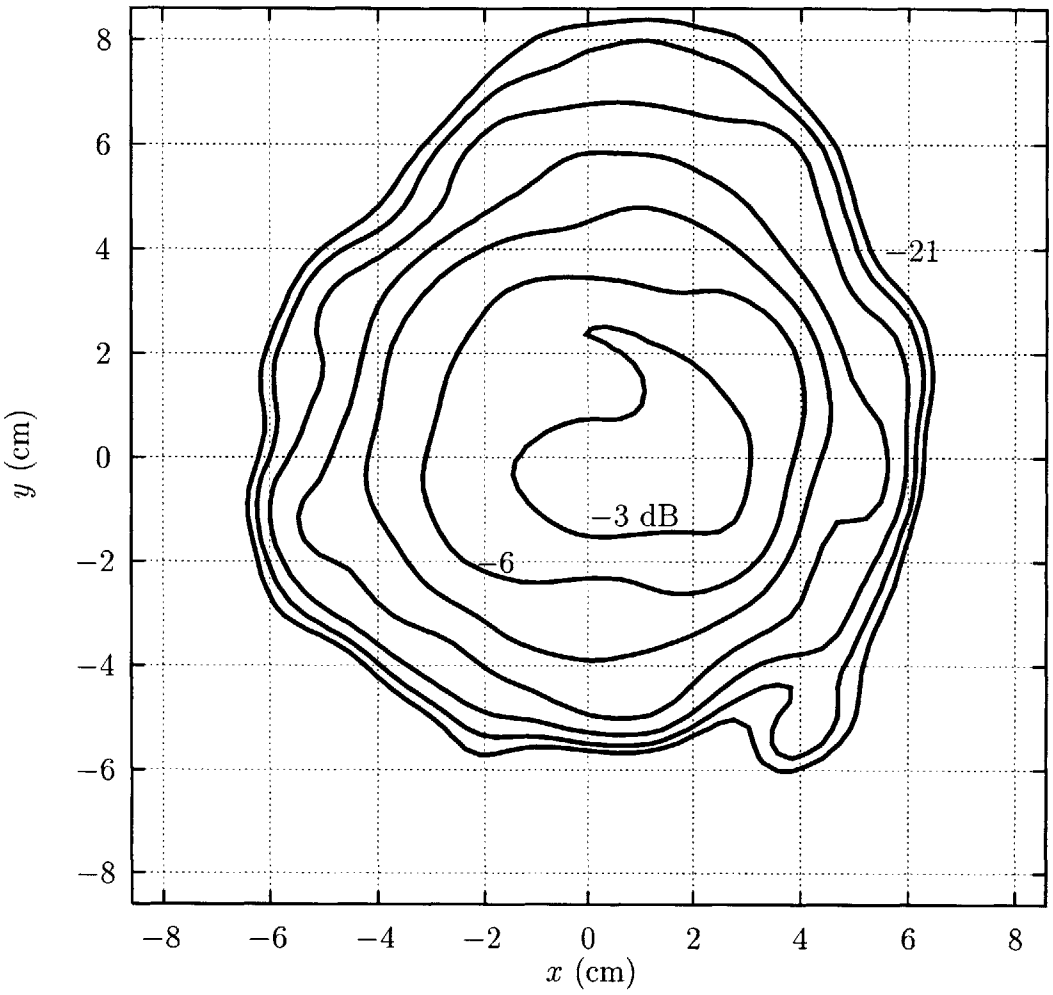

Figure 4-6: Measured field intensity on a plane located 64.6 cm from the gyrotron window. Contours of constant $|E_x|^2$ are at 3 dB intervals from peak; the −3 dB, −6 dB, and −21 dB curves are labeled.

heat rising problem.

In spite of the data corruption, we can still qualitatively access the accuracy of our phase retrieval. Comparing Figure 4-5 and Figure 4-6, we see that the reconstructed field profile generally agrees with the measured field. Notably, the upward tail on the -3 dB curve appears in the reconstruction, and the -6 dB and -9 dB curves have approximately the same size and shape. The shape of the -3 dB curve in the reconstruction differs somewhat from the measured intensity, but since the measured data on this plane were smeared by heat rising, some of the details visible in the reconstructed fields may have been washed out in the measurements.

The geometry of the MOU is shown in Figure 4-1. The first mirror is located 60 cm from the output window and the second mirror is 30 cm from the aperture of the corrugated waveguide. The mirrors are tilted 23° and have a face-to-face separation distance of 40 cm. The desired output beam of this system is a Gaussian beam with a waist of 0.95 cm. This waist size corresponds to $0.6a$, where a is the waveguide radius, and 99.6% of the beam power falls within the waveguide aperture. The chosen waist size also provides optimal coupling to the fundamental HE_{11} mode of the corrugated guide [25].

We follow the procedure described in Chapter 3 for shaping the surfaces of the mirrors. The incident field, shown in Figure 4-5, was computed from the reconstructed fields, and the desired field amplitude and phase on the surface of mirror two is found by back-propagating the specified Gaussian beam from the waveguide aperture using the analytic expression (2.12).

Using this pair of field profiles, we reconstruct the self-consistent phase from the field intensities and determine the phase-correcting functions according to the phase differences (3.1) and (3.2). The phase difference functions are then transformed to real space via (3.7) to form the actual mirror surfaces; the surfaces are shown in Figure 4-7. In Figure 4-7(a), the wave is incident from below, and in Figure 4-7(b), the wave is incident from above.

We see that the mirror surface profiles are predominantly spherical. This result is expected given that the gyrotron output beam is known to be strongly Gaussian from our reconstruction of the fields on the first mirror surface. On the first mirror surface (Figure 4-7(a)), there is a small perturbation to the spherical surface in the form of a bump that advances the phase in the region of the center of the beam to produce a Gaussian beam at the surface of the second mirror, as specified by the mirror shaping routine.

The mirror surfaces were simulated in the physical optics code introduced in Sec-

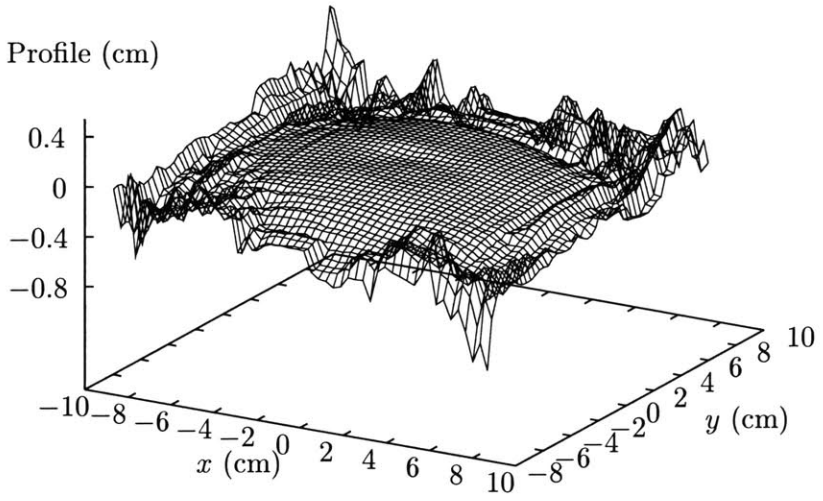

(a) First shaped mirror surface profile.

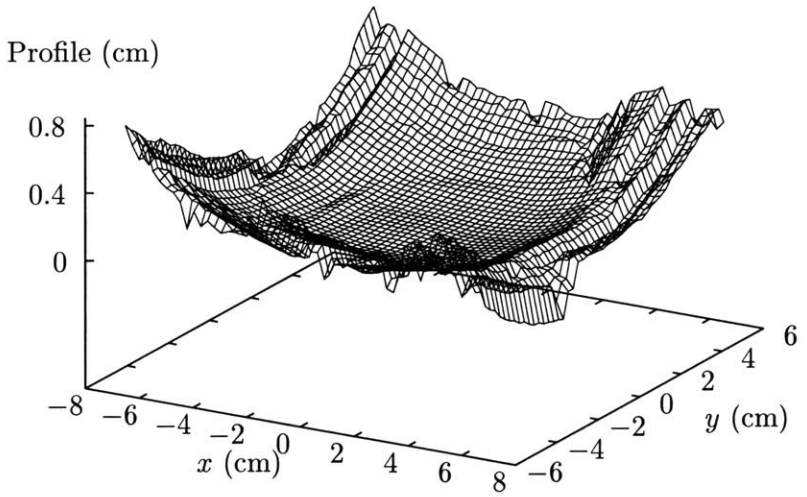

(b) Second shaped mirror surface profile.

Figure 4-7: Shaped mirror profiles for the S/N4 Matching Optics Unit. The profile depth scale has been exaggerated for contrast.

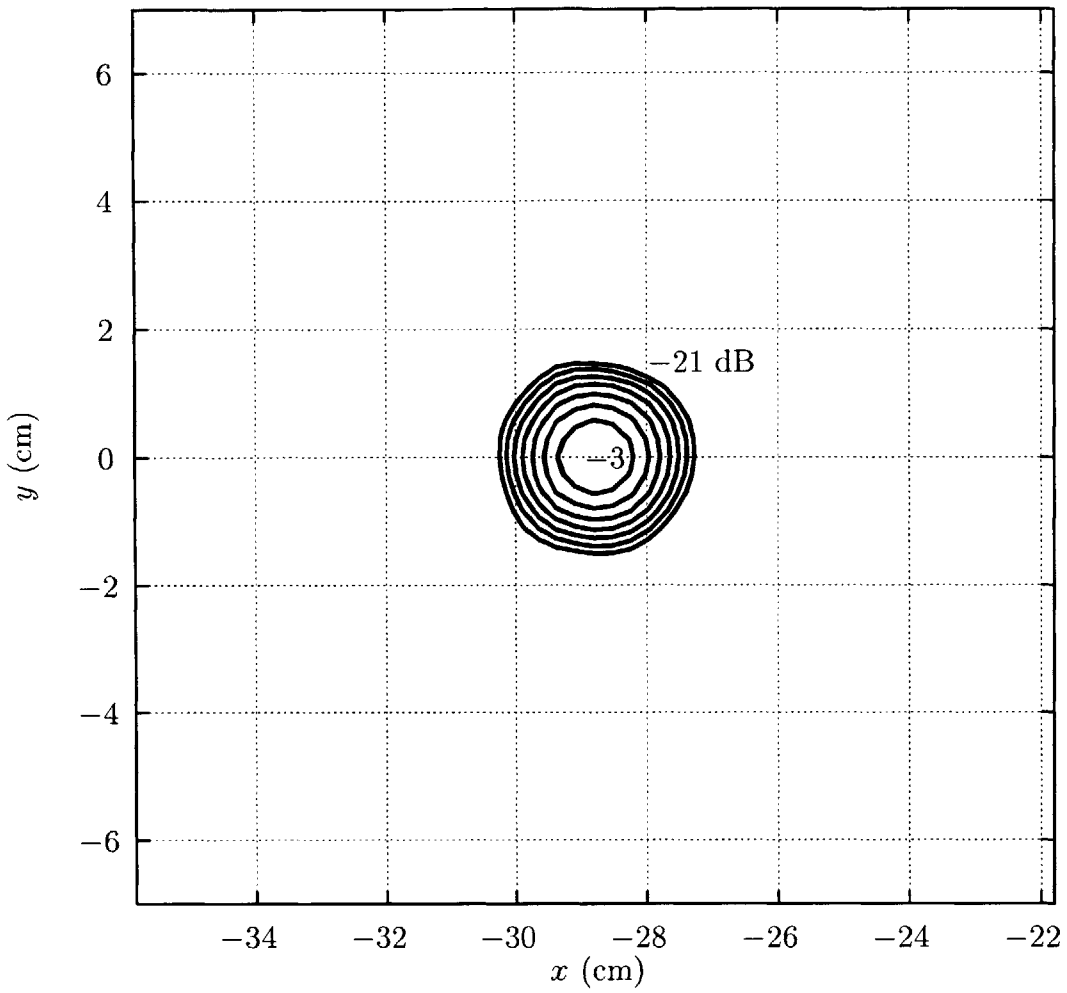

Figure 4-8: Simulated field intensity at the waveguide aperture. Contours of constant $|E_x|^2$ are at 3 dB intervals from peak; the −3 dB and −21 dB curves are labeled.

tion 2.4.4. The field over the reconstruction plane at 34.6 cm was radiated through the two-mirror system to the waveguide aperture. The simulated field intensity at the waveguide aperture is shown in Figure 4-8 and the corresponding phase along the x axis is shown in Figure 4-9. From these two figures we clearly see that the simulated output field of the MOU is a Gaussian beam in amplitude and phase. The fraction of beam power incident on the aperture is 99.5%. We are now ready to construct the mirror set for experimental validation of the design.

4.3 Experimental Results

The mirror surface shapes shown in Figure 4-7 were machined into solid copper using a numerically-controlled milling machine at Communications and Power Industries.

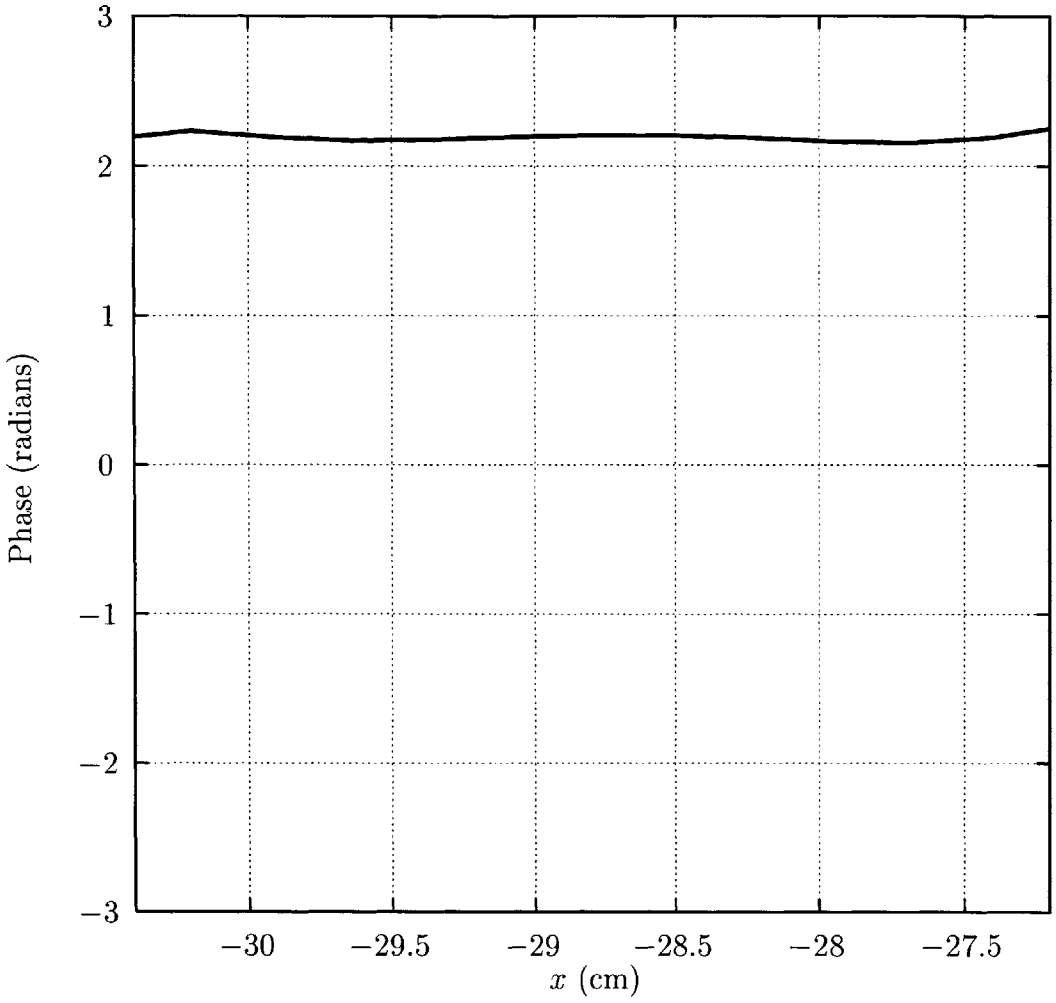

Figure 4-9: Simulated phase at the waveguide aperture along the x-axis.

The rough edges of the mirrors, where the power is negligible, were smoothed to a constant value prior to machining. The mirrors were installed in the S/N4 gyrotron MOU at General Atomics and infrared camera measurements were made at the position of the waveguide aperture and at several planes beyond the aperture. In all of the following measurements, the plane center in x is located, in the MOU geometry, at $x = -28.8$ cm.

Figure 4-10 shows the field intensity profile, from infrared camera measurements, at the waveguide aperture[1]. The beam appears to be well-focussed, but does not have a perfect Gaussian shape. The elongation in the $+y$ direction most likely arises because the microwave beam from the gyrotron has a beamlet in that region, as shown in Figure 4-4. The power in the beamlet is being directed into the main beam, but at the plane of Figure 4-10, remnants of the beamlet remain. Figure 4-11 gives a cut along the x axis through the measured data, and compares the measured intensity to that of an ideal Gaussian beam with a waist of 0.95 cm (the design waist size).

The measured beam has a Gaussian-like intensity profile, but the waist (the -8.68 dB point) is larger than design by approximately 4 mm. This larger beam radius corresponds to approximately 94.5% of the beam power falling within the waveguide aperture. We also see that the beam is not centered at $x = 0$; this offset can be corrected by tilting the second mirror in the MOU.

The measured beam intensity pattern at a plane located 10 cm after the aperture plane is given in Figure 4-12. At this position, the beam has a well-focussed, highly-symmetric Gaussian profile. In fact, Figure 4-13 confirms that the beam not only has an excellent Gaussian profile, but the waist size is the desired 0.95 cm. The smaller waist size allows 96.5% of the beam power in the waveguide aperture.

The field intensity pattern at 30 cm after the waveguide aperture plane is given in Figure 4-14, and this measurement confirms the Gaussian-like nature of the beam.

We saw from Figures 4-12 and 4-13 that the waist appears to occur at the plane located 10 cm past the waveguide aperture. To better quantify this observation, we can use the measured intensity profiles in the phase retrieval algorithm to find the phase of the MOU beam. We recover the phase from the intensity measurements located at the waveguide aperture, 10 cm past the aperture, and 30 cm past the aperture with 50 iterations and a flat initial phase guess. Figure 4-15 gives the reconstructed phase along the x-axis in the plane of the waveguide aperture. The curved phase indicates that the beam focus is somewhere beyond this plane; indeed,

[1]The arc contours to the right of the beam are images of the edge of the waveguide mounting flange port.

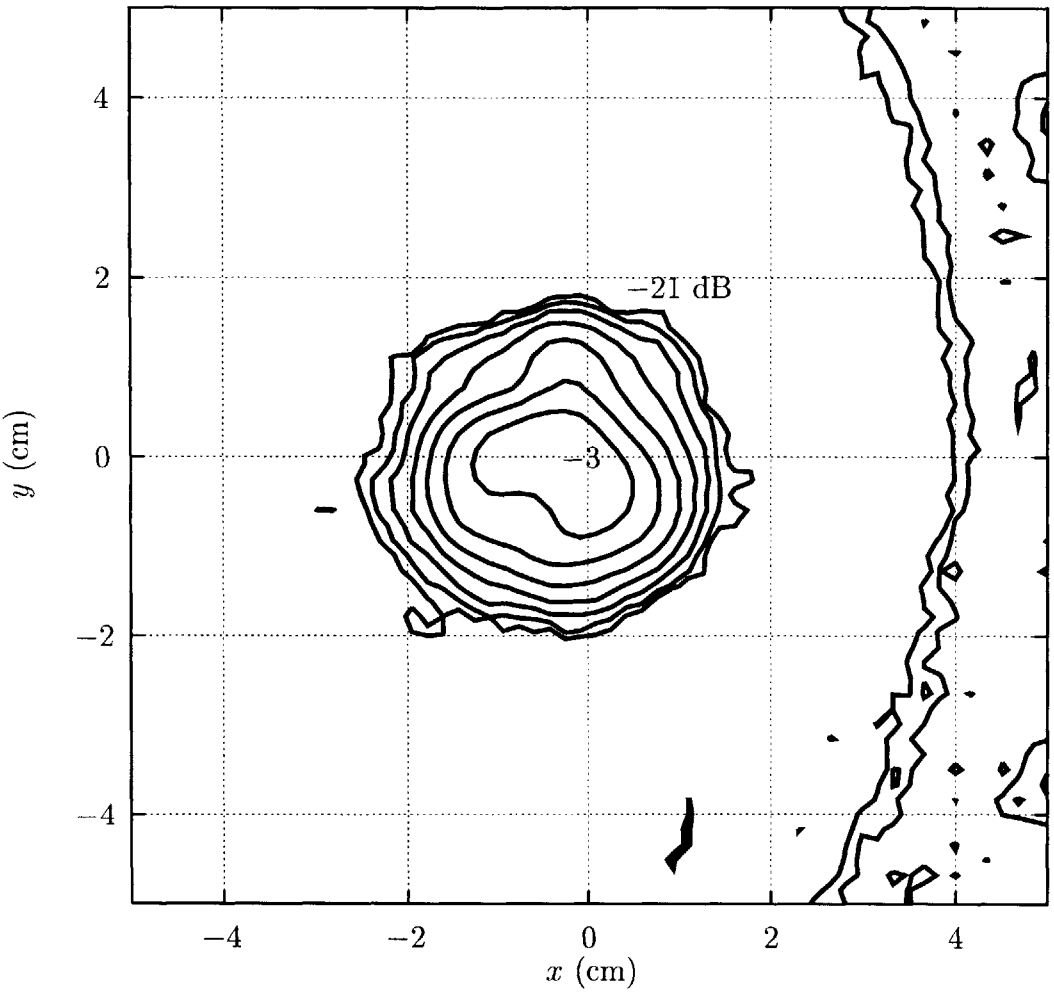

Figure 4-10: Measured field intensity at the waveguide aperture plane (30 cm from the second MOU mirror). Contours of constant $|E_x|^2$ are at 3 dB intervals from peak; the −3 dB and −21 dB curves are labeled.

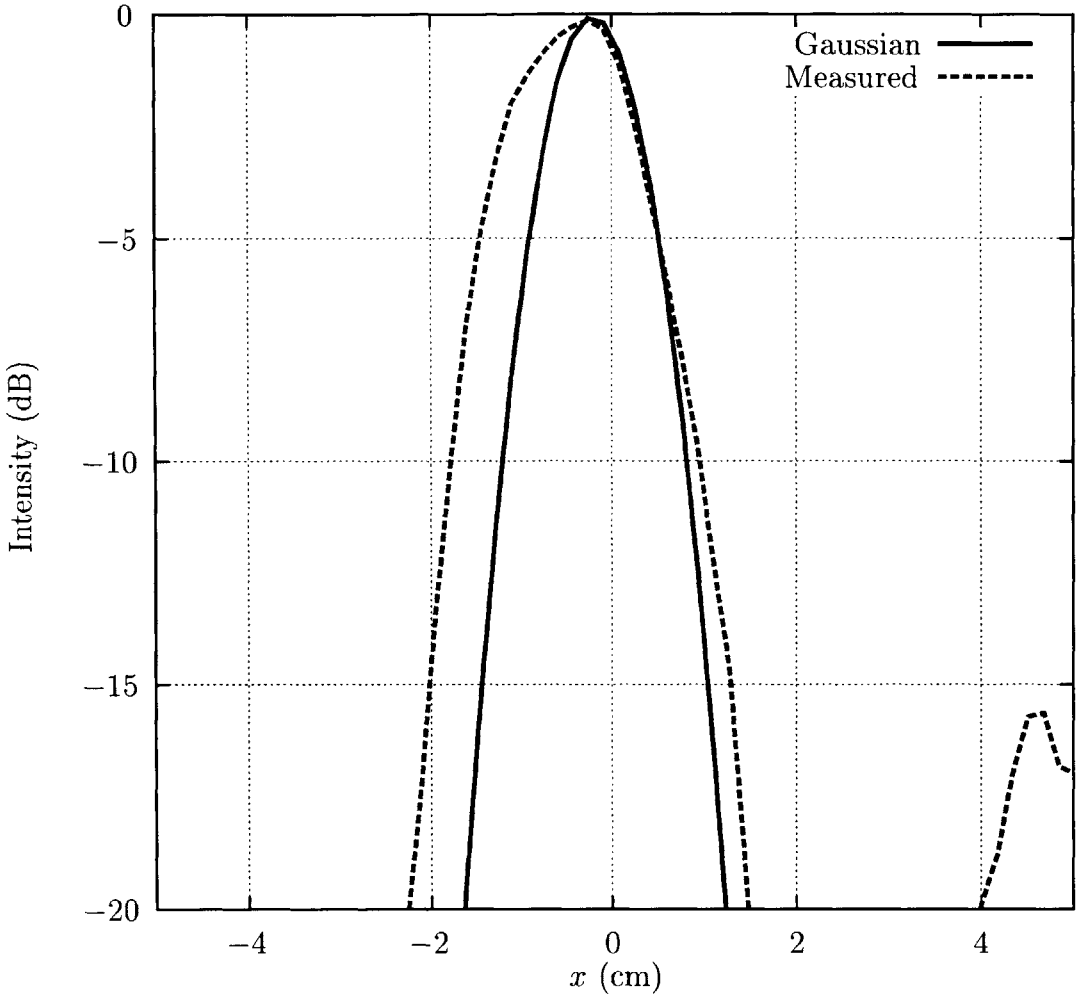

Figure 4-11: Ideal Gaussian with a 0.95 cm waist radius (solid) and measured (dashed) field intensity along the x-axis in the waveguide aperture plane.

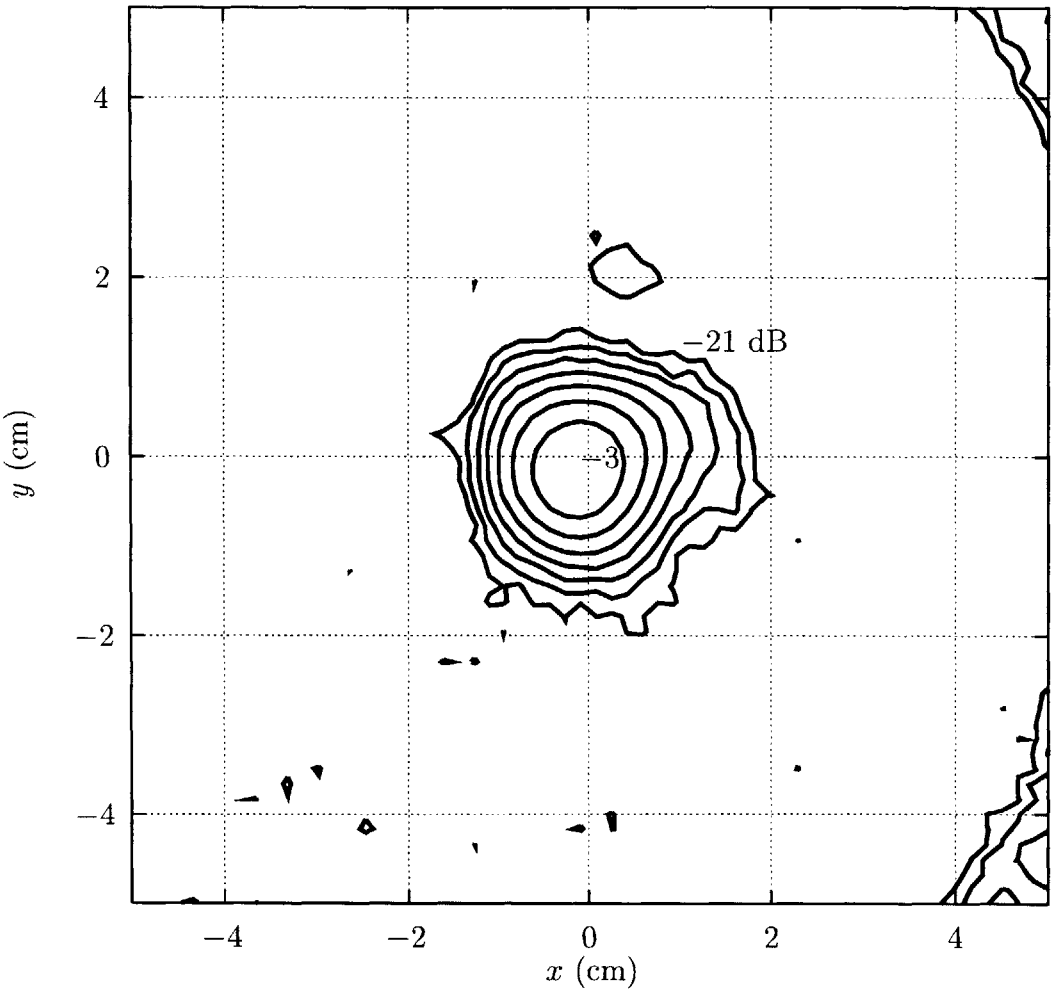

Figure 4-12: Measured field intensity 10 cm after the waveguide aperture plane (40 cm from the second MOU mirror). Contours of constant $|E_x|^2$ are at 3 dB intervals from peak; the −3 dB and −21 dB curves are labeled.

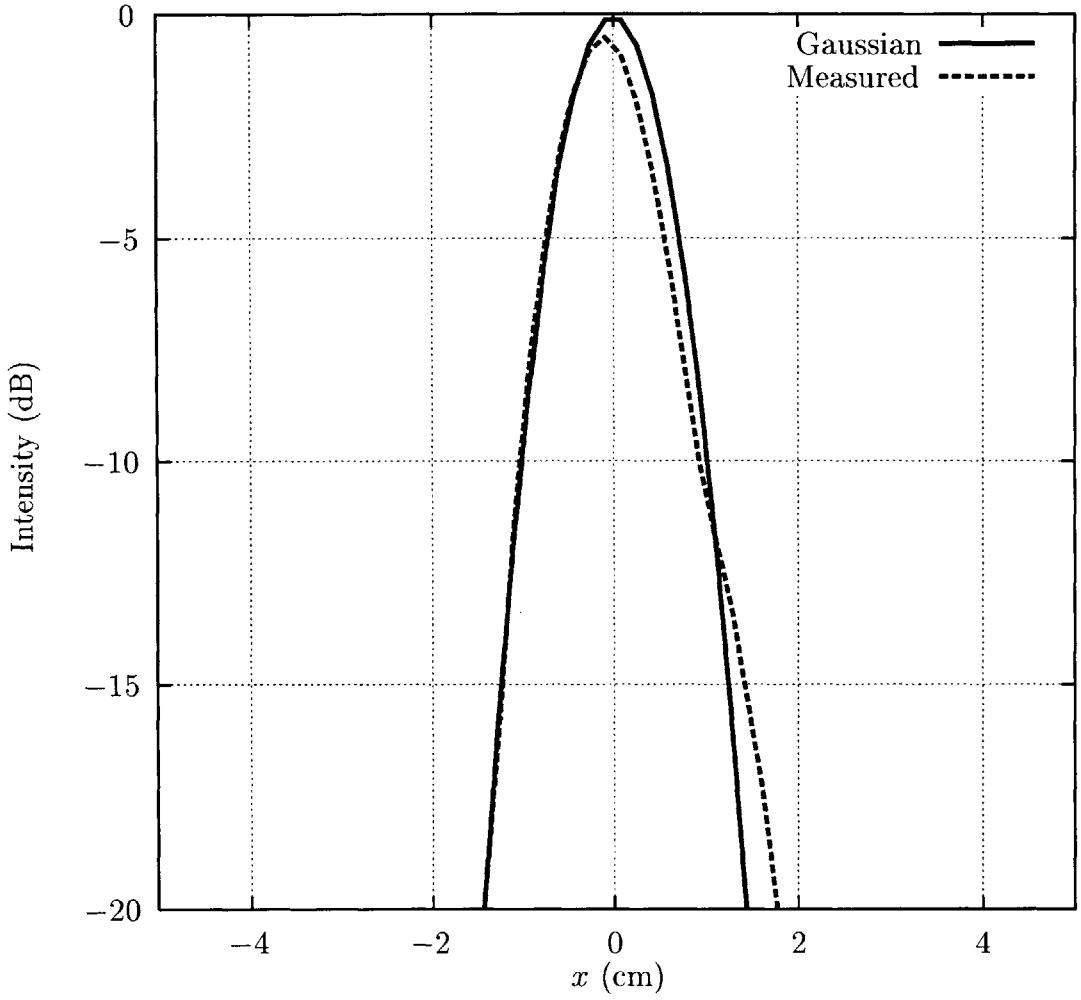

Figure 4-13: Ideal Gaussian with a 0.95 cm waist radius (solid) and measured (dashed) field intensity along the x-axis in the plane located 10 cm from the waveguide aperture.

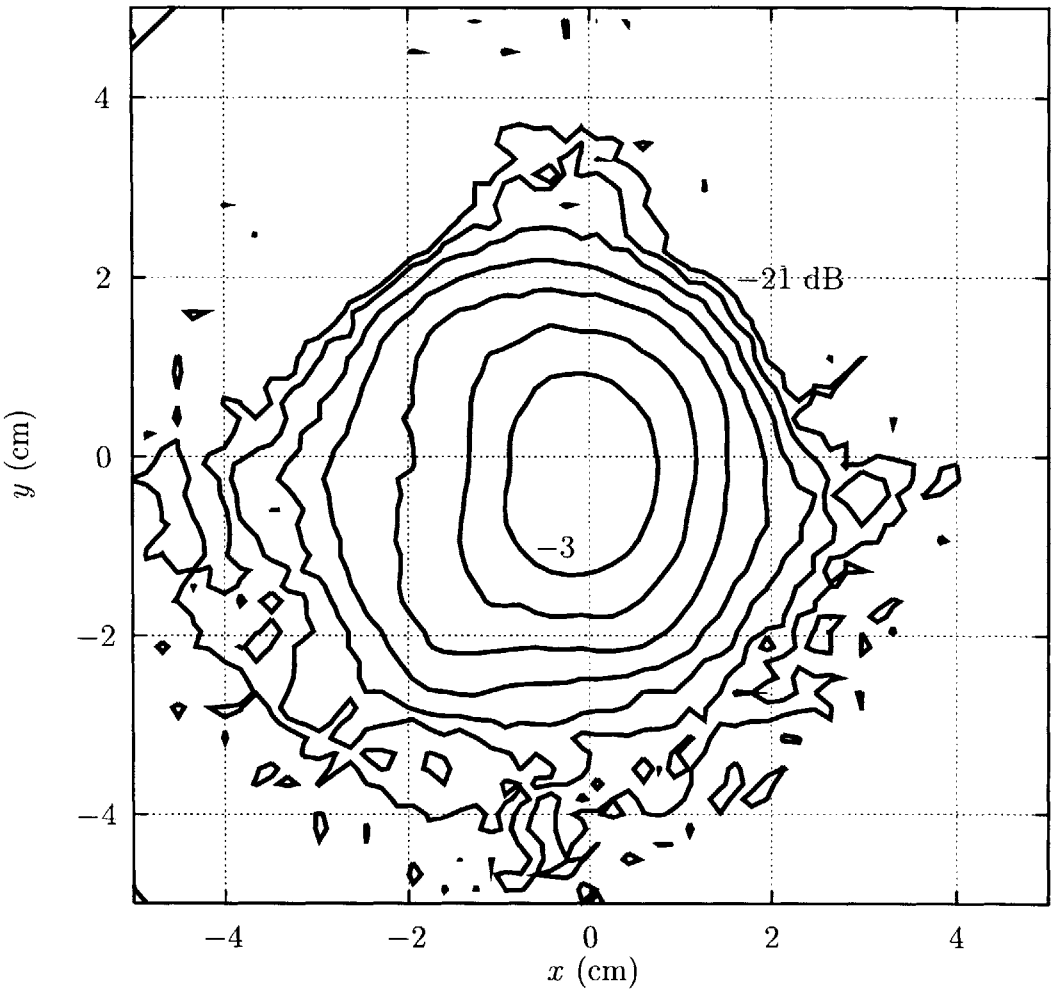

Figure 4-14: Measured field intensity 30 cm after the waveguide aperture plane (60 cm from the second MOU mirror). Contours of constant $|E_x|^2$ are at 3 dB intervals from peak; the −3 dB and −21 dB curves are labeled.

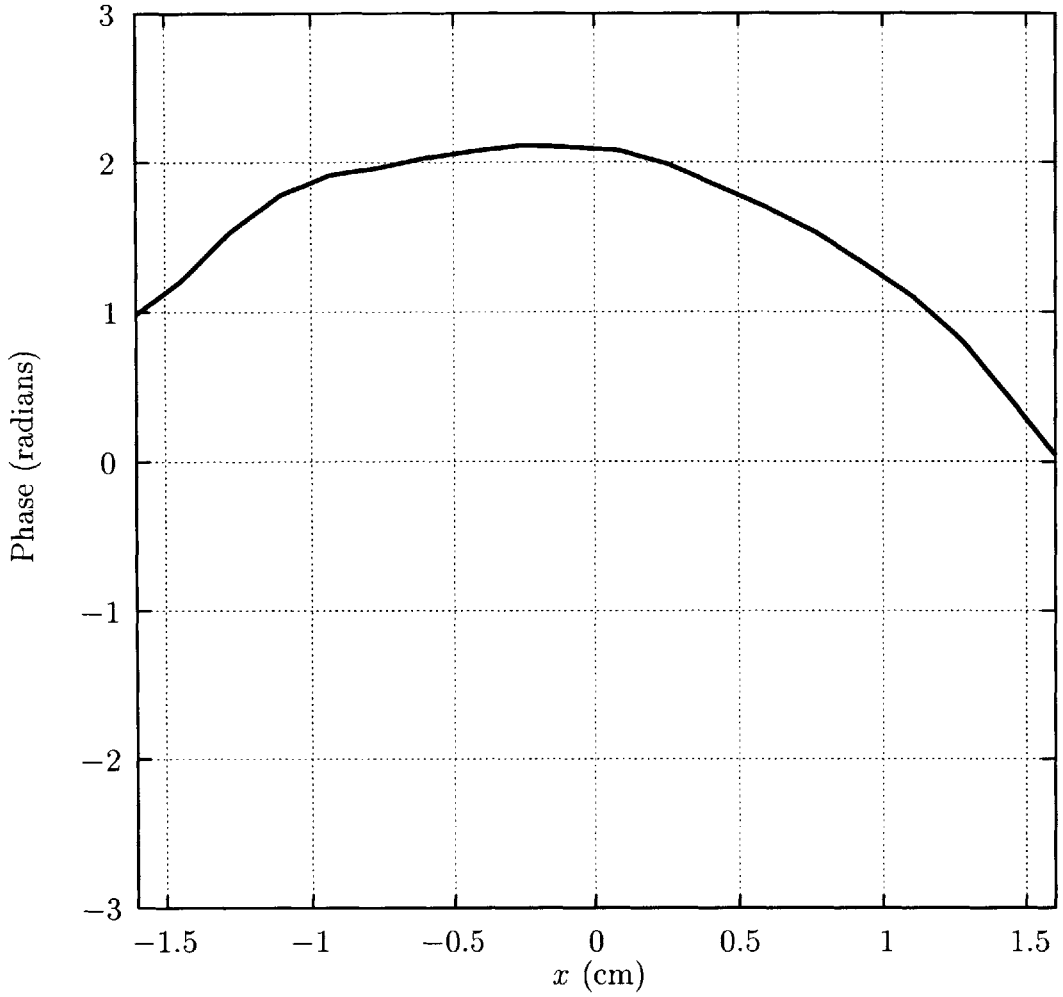

Figure 4-15: The reconstructed phase along the x-axis in the plane of the waveguide aperture.

we already suspect that the minimum waist occurs 10 cm after the aperture plane.

The reconstructed field at the aperture was propagated 10 cm to the measurement plane of Figure 4-12 and the phase along x in that plane is given in Figure 4-16. The phase is, as we expected, flat at this position. There is a slight tilt in the phase that appears because the beam is propagating at an angle, moving from $-x$ to $+x$, as seen from the shifting geometric beam centers in Figures 4-10, 4-12, and 4-14.

4.4 Discussion

The matching optics unit described in this chapter provides the first experimental validation of the phase retrieval and mirror shaping approaches developed in the previous chapters. The design required a pair of phase-correcting mirrors to transform

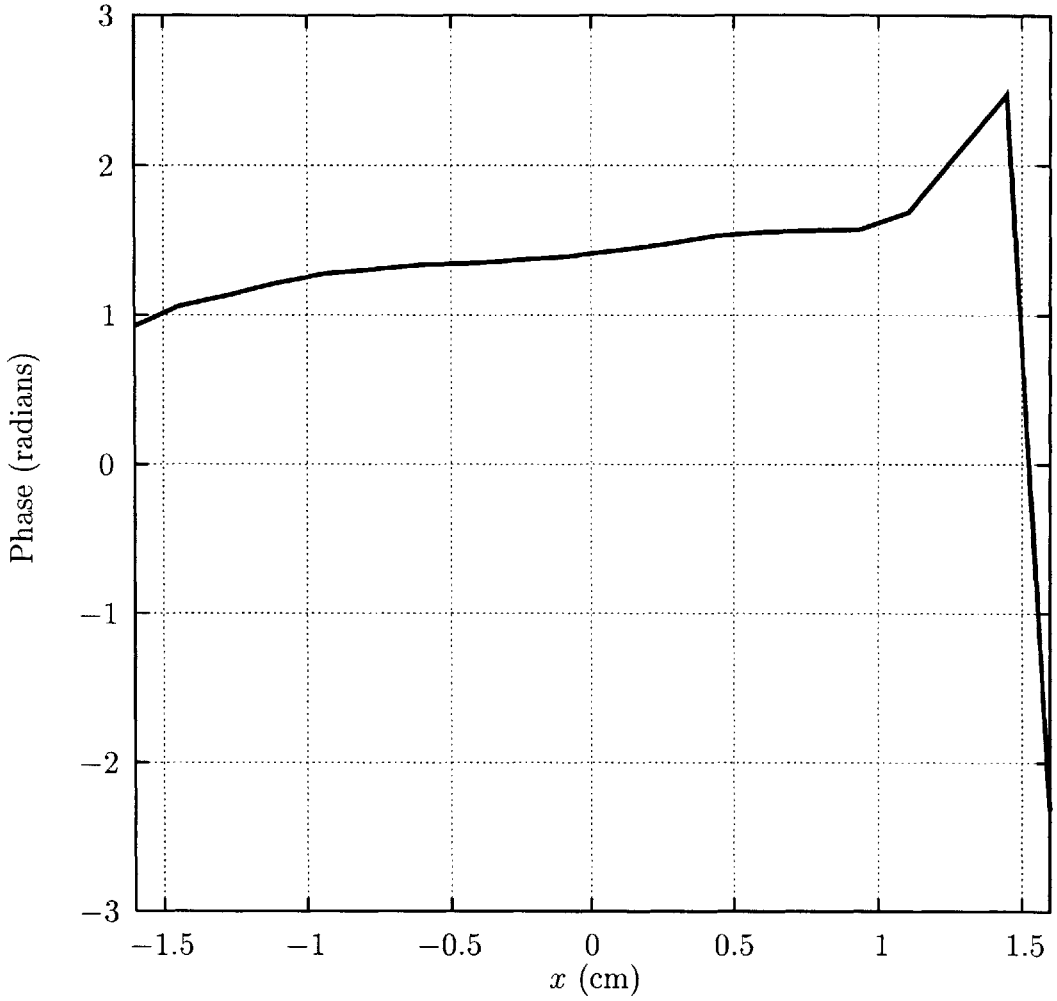

Figure 4-16: The reconstructed phase along the x-axis in the plane located 10 cm from the waveguide aperture.

the crescent-shaped gyrotron output microwave beam into an ideal Gaussian beam suitable for injection into a corrugated waveguide.

We began by making infrared camera measurements of the gyrotron microwave beam and discovered that most of these measurements were corrupted by heat rising on the target. This measurement error is clearly evident in the oblong, inconsistent shape of the intensity contours. Additionally, data corruption manifests itself when we attempt to perform a three-plane phase retrieval on these data. As shown in Section 2.4.3 and discussed at the end of Chapter 2, non-physical amplitude data cause the phase retrieval algorithm to diverge. Using any three-plane combination of the infrared camera measurements leads to a diverging error function (2.42), so we resort to using the two planes located at 34.6 cm and 99.6 cm from the window since they appear to be the least influenced by the heat rising measurement error. We then used the measurements over the plane at 64.6 cm as a check on our results, and we showed reasonable agreement between the measured and reconstructed intensity profiles on that plane.

Our mirror shaping approach, including the phase unwrapping algorithm mentioned in Section 3.2, led to smooth, largely spherical mirror shapes as expected since the beam from the gyrotron is strongly Gaussian. However, we know the beam is not an ideal Gaussian beam, and the surface of the mirrors are perturbed from the spherical in order to collect the non-Gaussian power and focus it into the main beam.

Measurements of the output of the MOU confirm that the mirrors transform the gyrotron crescent-shaped beam into a nearly-ideal Gaussian, but these measurements also show that the beam focus is displaced 10 cm from design. The power incident on the waveguide aperture is 94.5% of the total power in the beam, and 10 cm past the aperture the power ratio is 96.5%. These values are 5% and 3%, respectively, less than the ideal 99.6%. The later focus of the beam along with the lower-than-expected aperture power are most likely the result of phase error in the field reconstruction caused by the intensity measurement errors discussed above.

We note that although our Gaussian beam focus is displaced, the quality of the Gaussian beam is very good in both amplitude and phase. The positioning of the focus at 40 cm from the second mirror as opposed to 30 cm is not, from a practical standpoint, a serious matter. The corrugated guide can be moved transversely, or sections of guide can be added or removed, to align the mouth of the guide with the true focal spot of the beam. In fact, the actual position of the aperture is located 40 cm from the second MOU mirror.

In spite of the non-ideal nature of the output beam, the results of this experi-

mental study are encouraging. We were able to transform a rather complicated beam structure from the gyrotron into a fundamental Gaussian beam with good amplitude and phase characteristics. The limitation of the current design appears to be the accuracy of the initial field intensity measurements used in the phase retrieval. We will show in the next chapter that better intensity measurements generate a more accurate solution.

Chapter 5

Internal Mode Converter Mirror Design

This chapter presents the design of a pair of mirrors for a gyrotron internal mode converter. The application involves retrofitting the last two mirrors (M3 and M4 in Figure 1-3) of the existing mode converter in a 1 MW, 110 GHz gyrotron. This mode converter was described in Section 1.1 and also formed the basis for the mirror shaping benchmark of Section 3.3. The work in Section 3.3 was done in anticipation of the current design specifications, where we want to shape mirrors three and four to produce a Gaussian beam at a 5-cm-diameter single-disk diamond window that replaces the original 10-cm-diameter double-disk sapphire window (see Figure 1-4) on the gyrotron. The specified beam minimum waist is 1.52 cm and should occur at the window aperture, providing a flat phase over the window. This waist size corresponds to a theoretical transmission of 99.6% of the power in the microwave beam through the window aperture. This high transmission efficiency is necessary to prevent power absorption near the edge of the window, which is brazed to the outer housing of the gyrotron. Since this particular gyrotron (the S/N3 gyrotron, not to be confused with the S/N4 gyrotron of the previous chapter) is designed to operate in a continuous wave (CW) mode, the braze is potentially susceptible to melting if the microwave power incident near the edge of the window is appreciable. These requirements of circular beam shape, flat phase, and high transmission efficiency at the window are stringent, and they provide the most rigorous test thus far of our mirror design procedure.

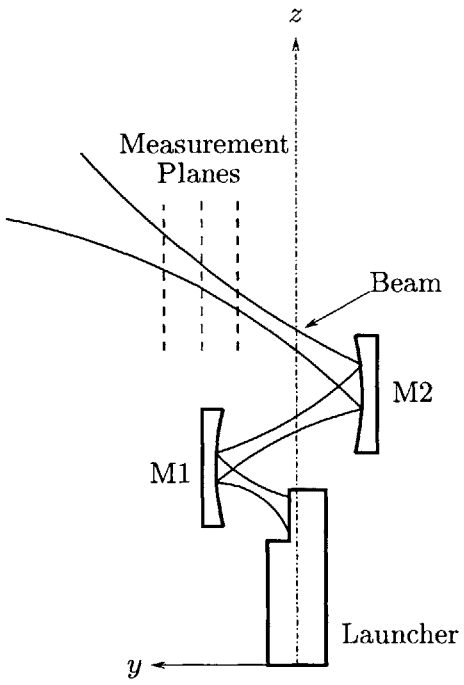

Figure 5-1: Schematic of scan geometry for the rigid launcher-toroidal mirror feed structure.

5.1 Feed Field Measurements

The first two mirrors in the mode converter were previously designed as toroidal (doubly-curved) surfaces based on simulated fields from the launcher, obviating the need in this application for Steps (1) – (3) in Section 1.3. The pre-existing launcher and toroidal mirrors form a rigid structure whose radiated field we measure according to Step (4).

The feed field intensity measurements were performed at Communications and Power Industries (CPI) using a three-axis motorized scanner built by the University of Wisconsin [6]. The receiving horn was an open-ended waveguide mounted on the scanner and fed to a heterodyne receiver. The launcher and first two mirrors were placed external to the gyrotron tube and the scanner was oriented to make planar scans as shown in Figure 5-1.

The launcher was excited by a Gunn diode source whose output was transformed into the $TE_{22,6}$ mode by a coaxial mode transducer. The mode purity of this transducer is estimated to be approximately 99%; a detailed discussion of mode purity in a similar transducer designed for the $TE_{15,2}$ mode is given in [26].

We performed measurements over nine planes near the position of the third mirror,

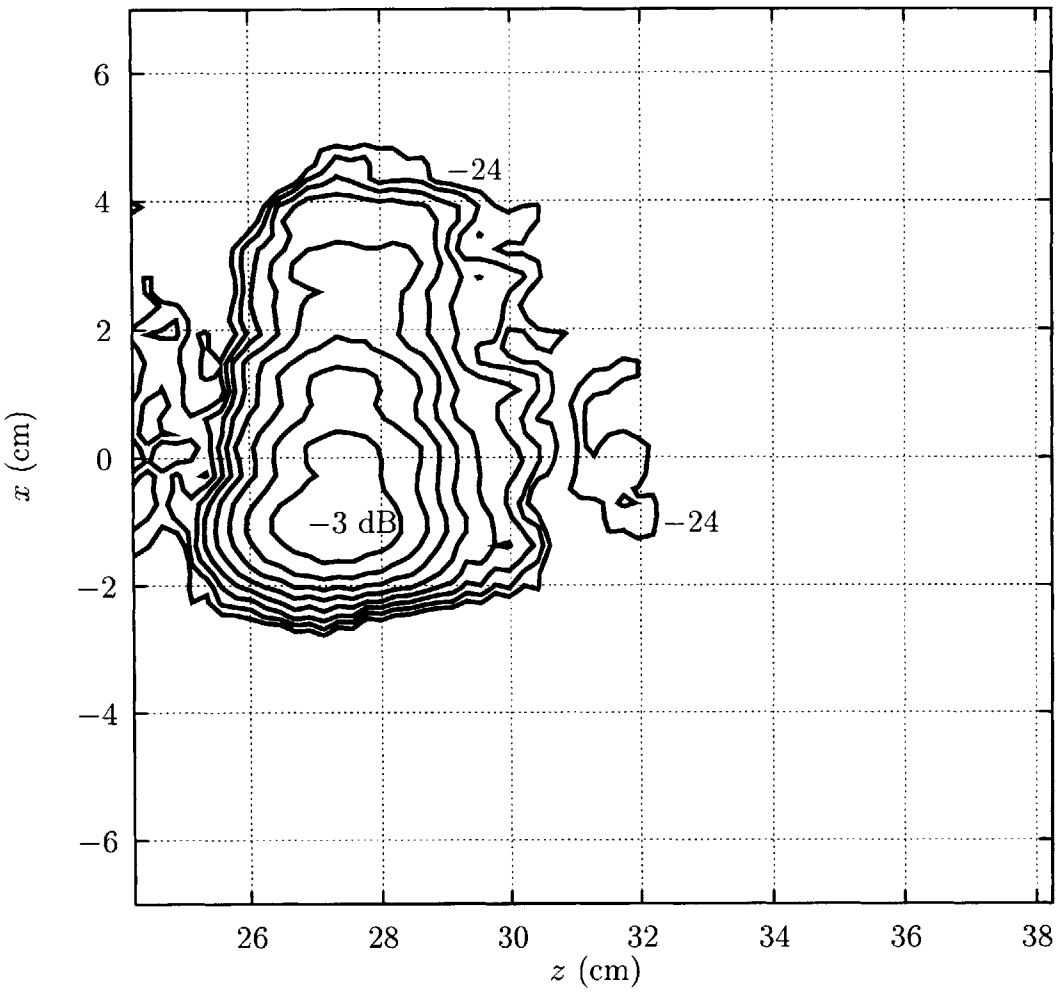

Figure 5-2: Measured field intensity over a plane at the mirror three position. Contours of constant $|E_x|^2$ are at 3 dB intervals from peak; the -3 dB and -24 dB curves are labeled.

as shown schematically in Figure 5-1. The planes are 14 cm $\times$ 14 cm with a 64 point $\times$ 64 point sampling grid that corresponds to a sampling density of 0.8λ. Figure 5-2 shows the measured field intensity on the plane of the third mirror, and Figure 5-3 shows the measured field intensity 11.9 cm from the third mirror plane.

The beam is propagating paraxially along a line 25° off the y-axis, out of the page, and has < -25 dB cross-polarization, indicating the scalar phase retrieval is suitable for this case. Furthermore, the beam shape changes significantly over the measurement range — from Figure 5-2 to Figure 5-3 —, so despite our relatively close plane spacing (on the order of tens of wavelengths) we can still expect an accurate field reconstruction according to the discussion in Section 2.5. Figures 5-4 and 5-5 show the field intensity measurements over the remaining seven measurement planes,

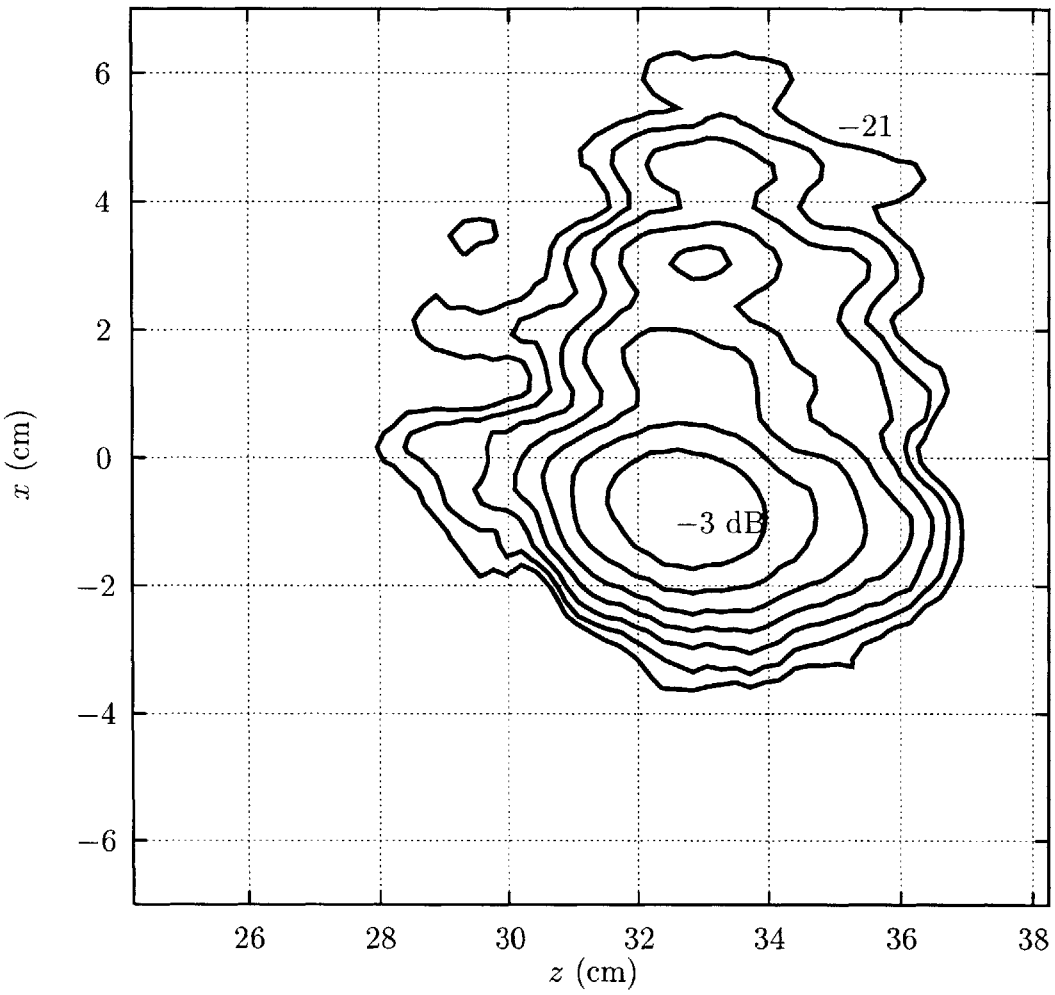

Figure 5-3: Measured field intensity on a plane located 11.9 cm in y from the mirror three position. Contours of constant $|E_x|^2$ are at 3 dB intervals from peak; the -3 dB and -21 dB curves are labeled.

and we see more clearly the evolution of the beam as it propagates.

5.2 Phase Retrieval

The measurements detailed in Section 5.1 were interpolated onto 128 point $\times$ 128 point grids to provide a 0.4λ grid spacing in order to avoid half-wavelength undersampling numerical artifacts in the phase retrieval. In addition, we modified the beam shape and position to temporarily create a beam propagating normal to the measurement (or observation) planes. Specifically, the profile of the beam was contracted by a factor $\cos\theta$ in z (θ is the incidence angle with respect to the plane normal) to account for the beam distension over the measurement planes, and the geometric centers of the beams were aligned along a common propagation axis. Such a transformation relieves the phase retrieval algorithm of retrieving both the nominal phase structure and phase tilt of the beam. Oblique beam propagation is accomplished by adding a phase tilt a posteriori to the nominal phase structure determined by the phase retrieval.

The phase was retrieved in 500 iterations with three measurement planes located approximately 25λ apart. The reconstructed field was propagated to a plane located 15 cm before the mirror three plane, and this field was then used in the physical optics code (see Section 3.3) to verify the accuracy of the reconstruction. Figure 5-6 shows the results of propagating this reconstructed field back to the mirror three plane. Comparing this field intensity pattern to the measured pattern at the same location in Figure 5-2 indicates that both the shape and position of the reconstructed wave closely match the measured field profile.

In Section 1.2, we showed the difference between the measured and theoretically-predicted intensities at the mirror three plane. We can now compare the reconstructed phase to the theoretically-predicted phase gain a greater appreciation for the differences between theory and experiment. Figure 5-7 shows the theoretically-predicted and reconstructed phase on a plane at the mirror three position. As in the case of the intensities, the differences in phase are not strong — the general shapes are the same — but we see that along the x-direction, the reconstructed phase varies more slowly than the theory phase, and along z the reconstructed phase varies faster. These observed differences in both intensity and phase ultimately result in the non-ideal radiation pattern at the window, as demonstrated in the next section.

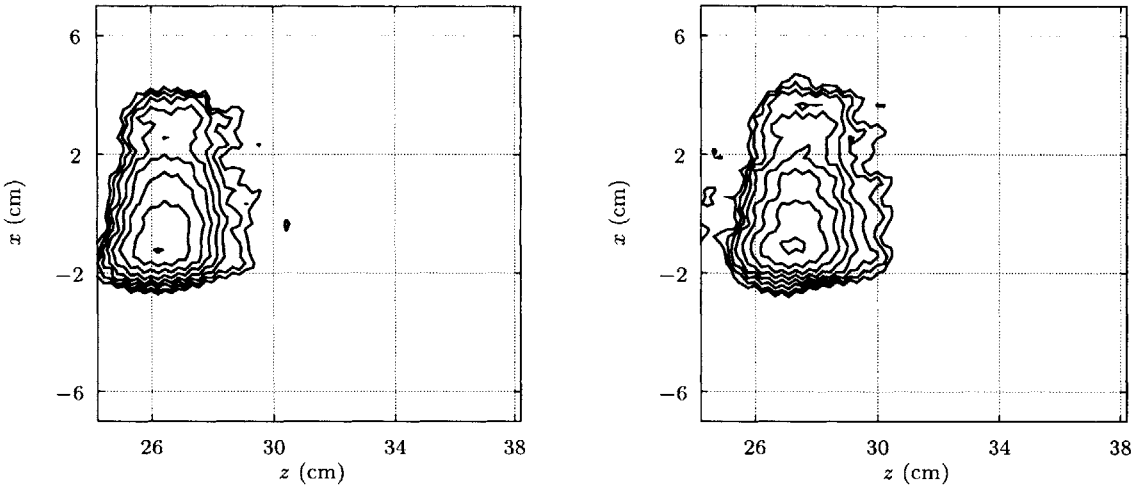

(a) $y_d = -2.1$ cm

(b) $y_d = -0.1$ cm

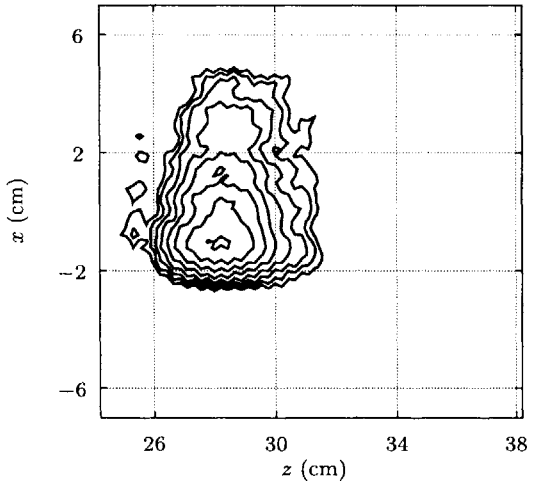

(c) $y_d = 1.9$ cm

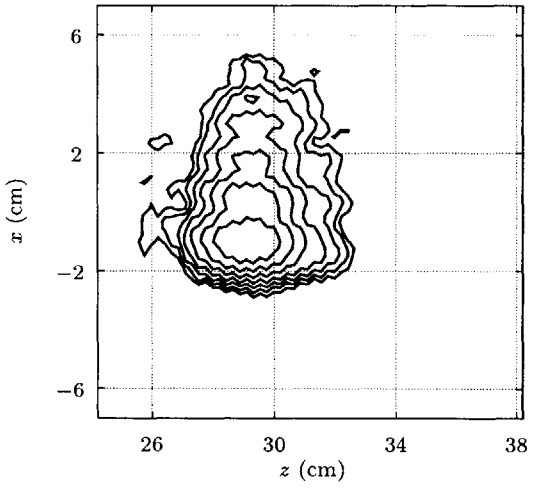

(d) $y_d = 3.9$ cm

Figure 5-4: Measured field intensity on planes with increasing distance from the mirror three position. Each sub-figure caption gives the displacement y_d with respect to the mirror three plane. Contours of constant $|E_x|^2$ are at 3 dB intervals from peak.

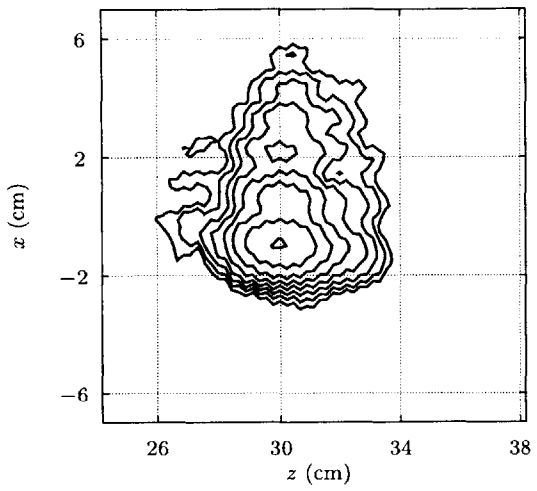

(a) $y_d = 5.9$ cm

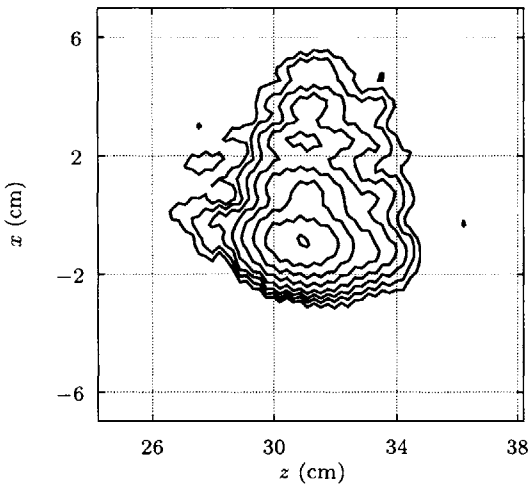

(b) $y_d = 7.9$ cm

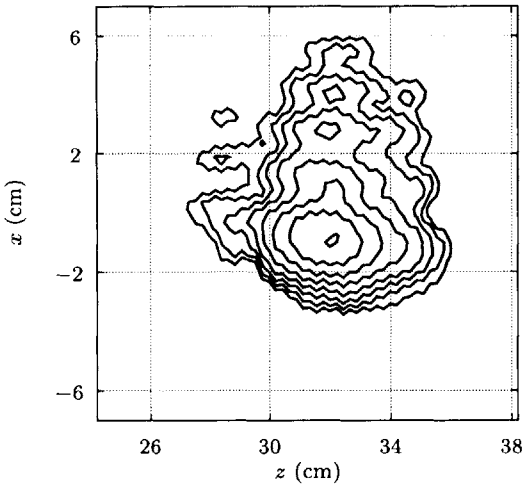

(c) $y_d = 9.9$ cm

Figure 5-5: Measured field intensity on planes with increasing distance from the mirror three position. Each sub-figure caption gives the displacement y_d with respect to the mirror three plane. Contours of constant $|E_x|^2$ are at 3 dB intervals from peak.

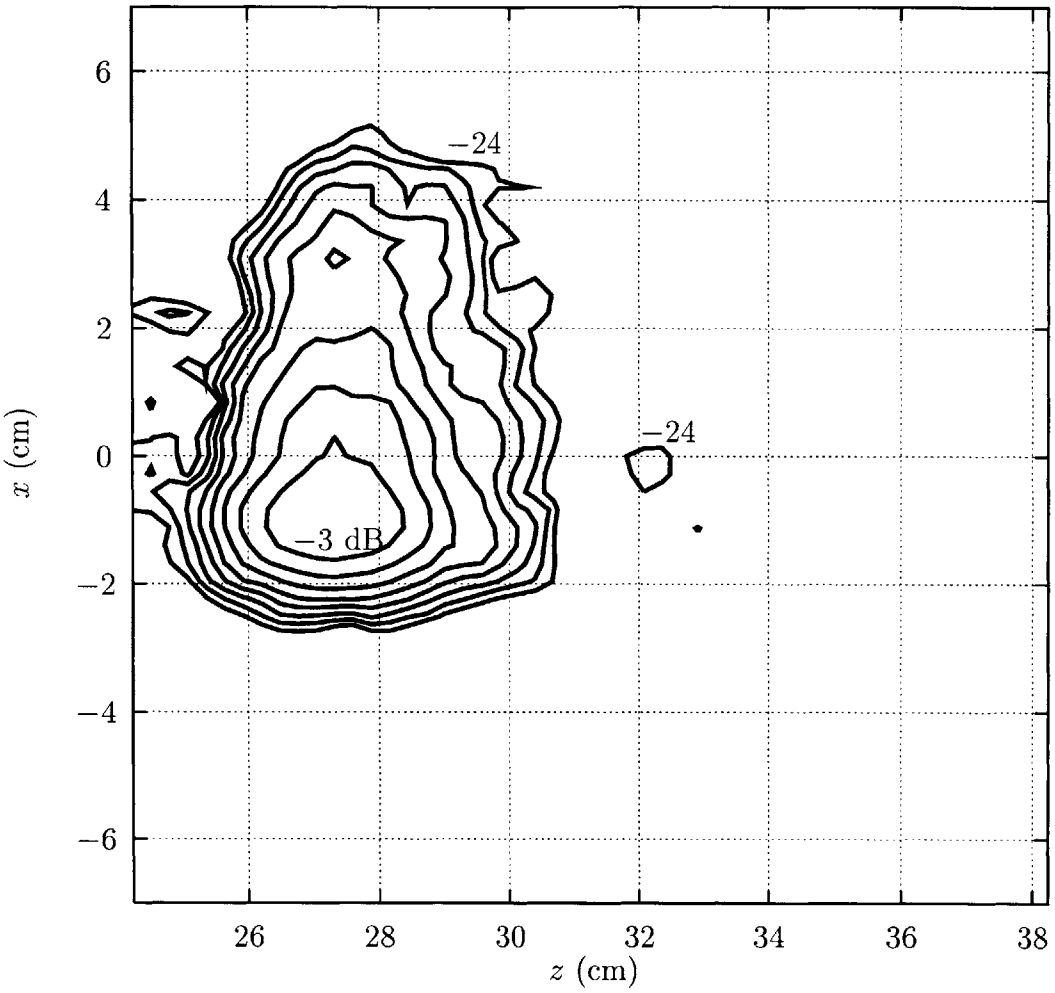

Figure 5-6: Simulated field intensity on the mirror three plane computed from reconstructed fields. Contours of constant $|E_x|^2$ are at 3 dB intervals from peak; the -3 dB and -24 dB curves are labeled.

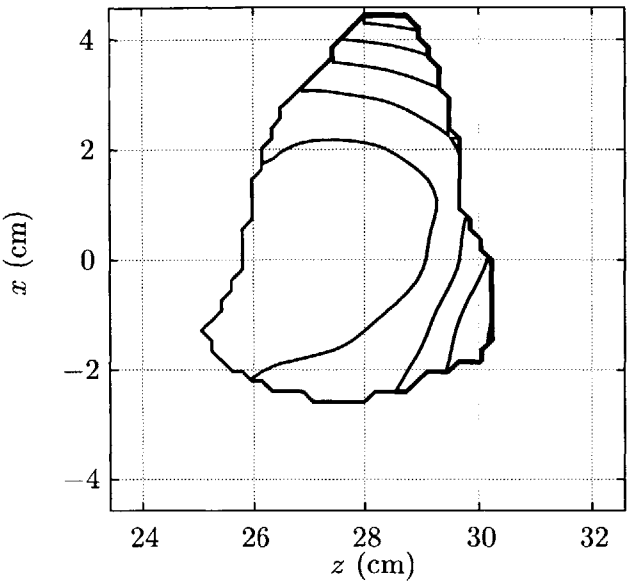

(a) Theoretically-predicted phase.

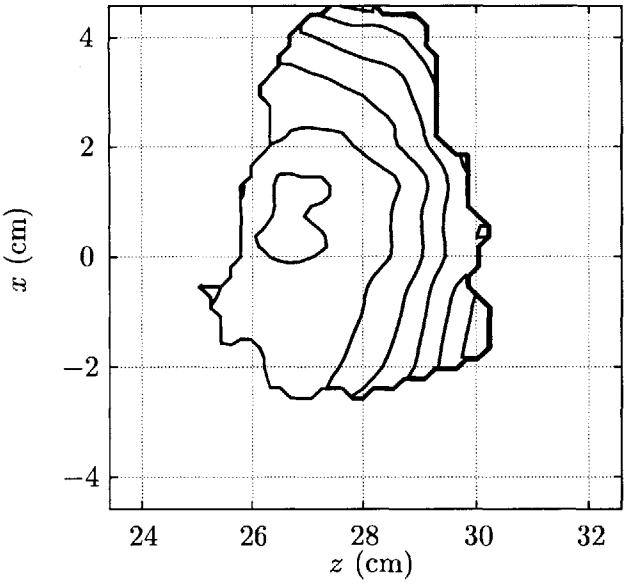

(b) Reconstructed phase.

Figure 5-7: Theoretically-predicted and reconstructed phase on the mirror three plane. Contours of constant phase are at 1 radian increments.

5.3 An Aside: Mode Converter Analysis

In developing our approach to mode converter mirror shaping based on intensity measurements, we implicitly assumed that the discrepancies between the theoretically-predicted and measured gyrotron microwave beams were caused by waveguide elements before the last two mirrors in the system. We showed in Chapter 1 (Figures 1-9 and 1-8) that the measured field incident on the third mirror does indeed differ from the field predicted by theory, but we have not ruled out the possibility that mirrors three and four are an additional source of the observed differences.

Now that we have the reconstructed *measured* fields incident on mirror three, an interesting exercise is to simulate those fields with the original mirrors three and four and compare the simulated output beam with measurements. We can then, at least qualitatively, make an estimate regarding the relative influence of mirrors three and four on the discrepancy between the measured and theoretically-predicted gyrotron beam.

Figure 5-8 shows the resulting field intensity profile at the plane of the 10-cm-aperture sapphire window after propagating the reconstructed beam computed in Section 5.2 through the original mirror three-mirror four transmission line. The crescent shape observed in experiments (see Chapter 1 and Figure 1-7) is clearly evident in this simulated case, demonstrating that the fields incident on mirror three are sufficiently different from those predicted by theory to account for the distortion in the gyrotron output microwave beam[1]. With this knowledge and the successful design reported in Chapter 4, we can proceed with some confidence that correcting the measured fields following mirror two inside the mode converter will produced the desired Gaussian beam on the output window.

5.4 Mirror Shaping and Simulation

We shaped a pair of mirrors using the procedure described in Chapter 3 with the reconstructed field from Section 5.2 as the incident wave, $A_1 e^{i\phi_1}$, and the desired 1.52-cm-waist Gaussian back-propagated to mirror four as output, $A_2 e^{i\phi_2}$.

One important aspect of the mirror shaping procedure not mentioned in Chapter 3

[1]Here we have compared the field profile from the S/N4 gyrotron with simulations using reconstructed fields from measurements of the S/N3 gyrotron internal mode converter. Although these two mode converters are physically different, they were constructed from the same design using identical fabrication techniques. The actual differences between the two mode converters are known, from earlier cold-test measurements, to be negligible.

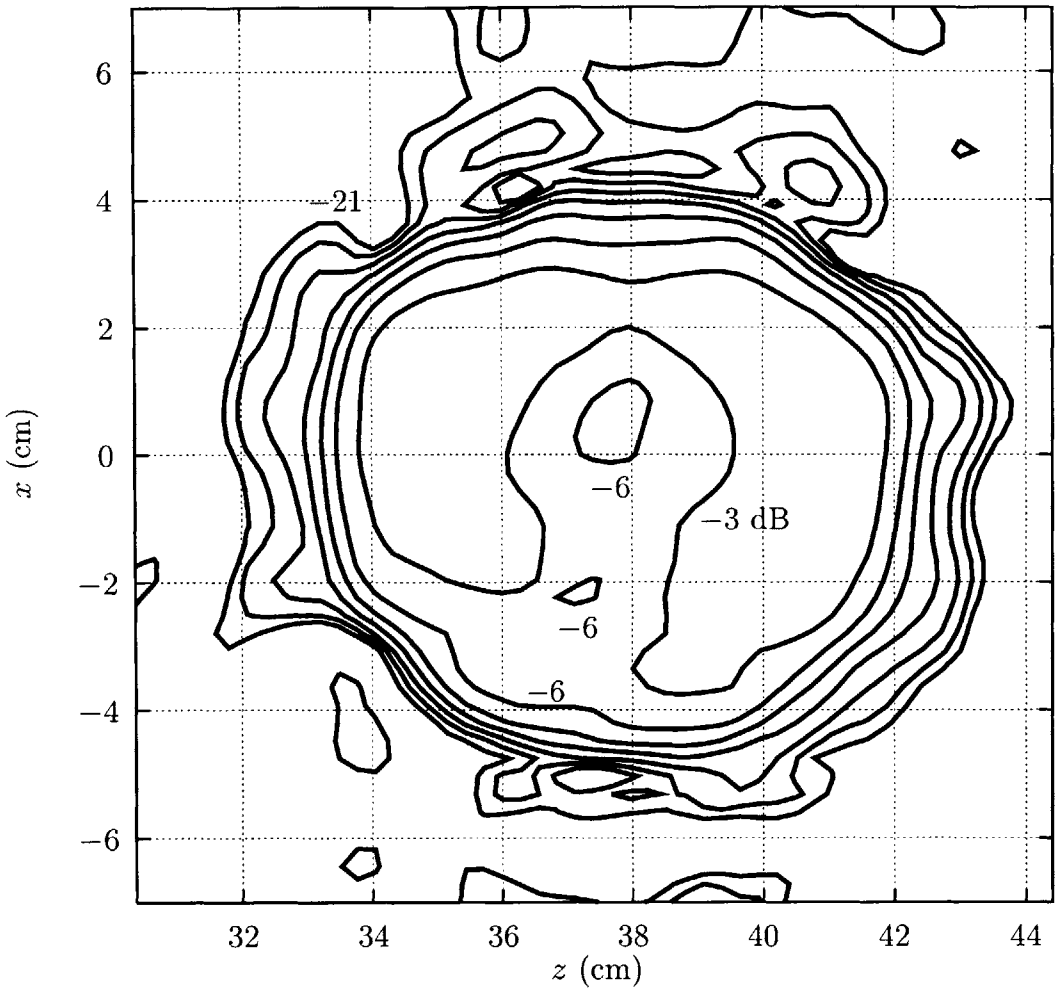

Figure 5-8: Field intensity on the 10-cm-aperture window computed from reconstructed fields at the mirror three position. Mirrors three and four used in the simulations are the original mode converter mirrors designed to produce a uniform field profile on the window. Contours of constant $|E_x|^2$ are at 3 dB intervals from peak; the −3 dB, −6 dB, and −21 dB curves are labeled.

is the fact that the physical sizes of the actual mirror surfaces must be taken into account in the shaping if the measurement plane is considerably larger than the mirror aperture. For instance, the third mirror (M3 in Figure 1-3) is limited in z — along the tube axis — to approximately 8.5 cm; this dimension is large enough to intercept both the main beam and the -24 dB sidelobe in Figure 5-2, but it is significantly more narrow than the observation plane. To account for the smaller size of the physical surface, we simply set all field amplitudes outside of the surface perimeter to zero. The benefit of incorporating the final mirror dimensions in the shaping procedure becomes apparent if we consider instead the case of using the whole observation plane in the design and then forming the surface boundary afterwards. The result is that our assumed field over the entire observation plane will be truncated by a rectangular window whose pulse width is the physical width of the mirror. The radiated field reveals this windowing as the familiar convolution of the desired field pattern with a sinc function, which leads to unwanted sidelobes.

The final mirror surface shapes are shown in Figure 5-9. For the third mirror, the beam is incident from below. Physically, we see that the elongation in the x-direction of the pattern in Figure 5-2 will be focussed into the main portion of the beam by the sharp curvature evident for $x > 0$ in the mirror's profile. The random surface fluctuations around the edge of the mirror arise because the phase in that negligible-amplitude region is indeterminate. The beam radiated from the third mirror propagates to the fourth mirror (from above), also shown in Figure 5-9. The surface is strongly spherical to focus the incident wave into the desired Gaussian beam at the window aperture.

The mirrors were simulated in the physical optics code using the reconstructed fields after mirror two as the initial field distribution. The simulated field intensity pattern on the window, shown in Figure 5-10, is in fact the desired Gaussian beam. Integrating the power over the observation plane reveals that 99.5% of the beam power will pass through the aperture as compared to 99.6% for an ideal Gaussian with a waist size of 1.52 cm in the 5 cm aperture. Figure 5-11 compares the intensity profile of the desired Gaussian beam to the simulated beam. The simulated beam exhibits a nearly-ideal Gaussian profile with a waist size of 1.55 cm — 0.03 cm larger than the 1.52 cm design. The sidelobe to the right of beam, on the $+z$ side, corresponds to unrecovered sidelobe power originally generated by the feed, as seen in Figure 5-2.

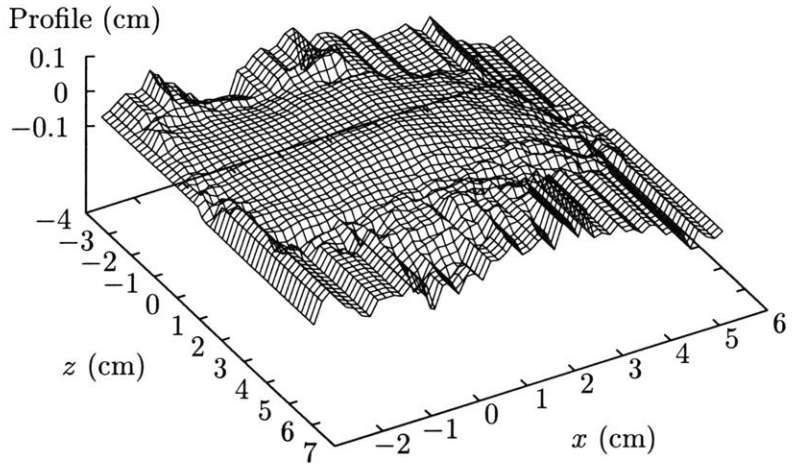

(a) First shaped mirror (mirror three) surface profile.

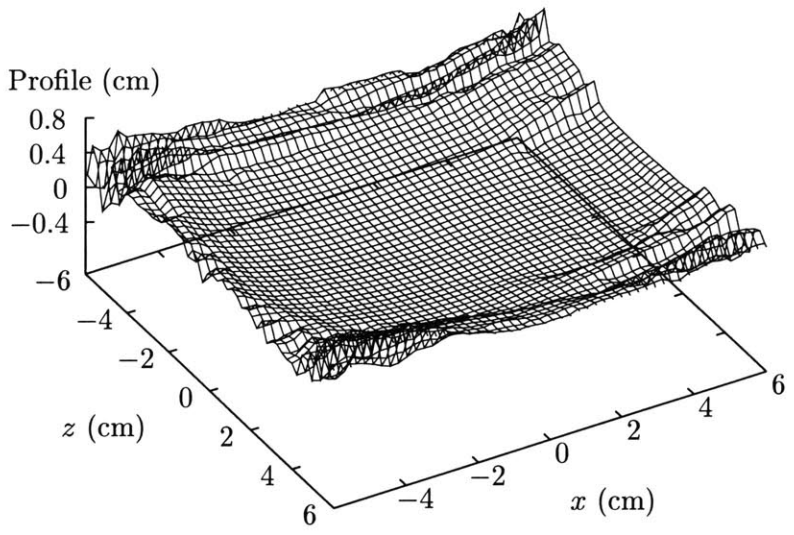

(b) Second shaped mirror (mirror four) surface profile.

Figure 5-9: Shaped mirror profiles. The profile depth scale has been exaggerated for contrast.

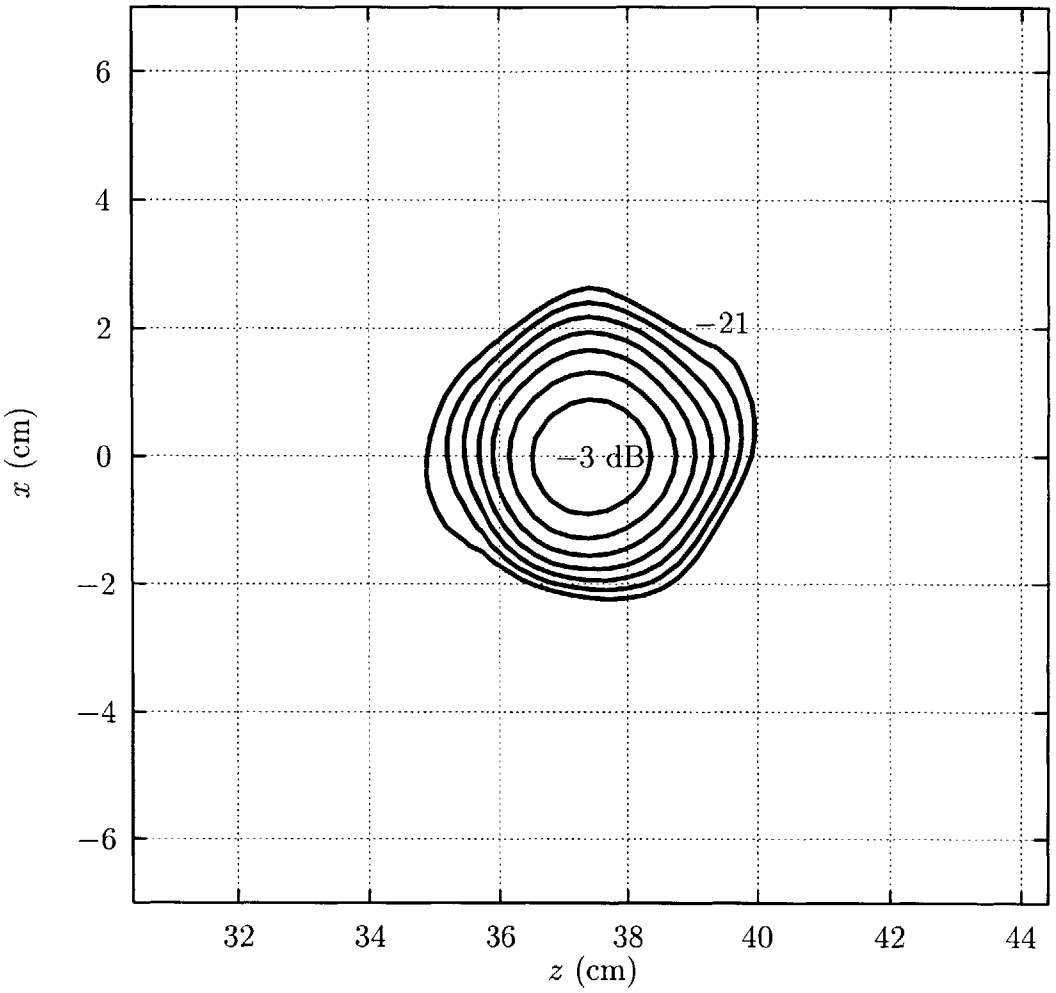

Figure 5-10: Simulated field intensity on the window plane. The window center is at $z = 37.4$ cm, $x = 0$ cm. Contours of constant $|E_x|^2$ are at 3 dB intervals from peak; the -3 dB and -21 dB curves are labeled.

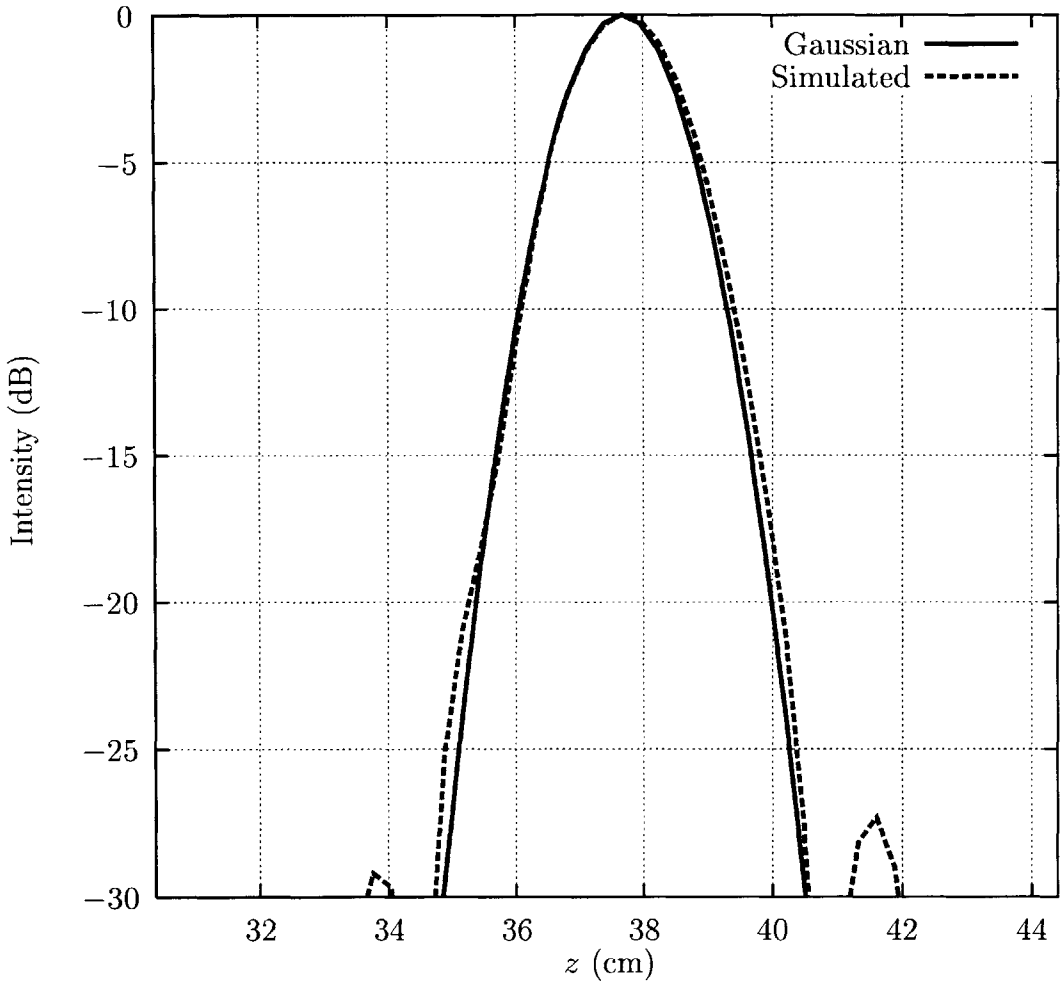

Figure 5-11: Desired Gaussian (solid) and Simulated (dashed) beam intensities along the z-axis at the window plane. The window center is at $z = 37.4$ cm.

5.5 Experimental Results — Cold Tests

The shaped mirrors were fabricated from solid copper and mounted on the feed structure for cold-test measurements of the output field. Using the same source/receiver arrangement from the feed field intensity scans (Section 5.1), we measured the output field intensity before, on, and after the window plane. Figure 5-12 shows the field pattern on the window plane. The measured beam is a well-formed Gaussian with a size, shape, and position that agree well with the simulated beam in Figure 5-10. The cross-polarized component is approximately 30 dB below the peak of the main polarization, confirming our assumption of a scalar field. The measured beam is slightly elliptical with a waist size in z of 1.6 cm and a waist size in x of 1.7 cm. The larger beam waist of 1.7 cm amounts to only a 0.66λ deviation in beam radius from design. An ideal Gaussian beam with these waist parameters will transmit 99% of the beam power through the 5 cm window aperture; due to the presence of some low sidelobe power, the integrated value for the measured data is 98.5%. This value is acceptable for high power gyrotron operation, and represents a 1% error in the design. This close agreement of measured beam waist size and transmitted power to the specified design parameters indicate that our mirror shaping approach works very well.

To further examine the Gaussian quality of the beam, we compare an ideal Gaussian intensity profile to that of the measured beam. The measured and theoretical intensity profiles along z are given in Figure 5-13. We note the measured beam has an excellent Gaussian profile that matches the ideal beam over the range of appreciable intensity. The -21 dB sidelobe to the right of the main beam appears because the sidelobe incident on the third mirror (see Figure 5-2) is not fully reflected into the main beam. This sidelobe may be unrecoverable because it is propagating at a different angle than the main beam, most likely the result of spurious mode radiation from the launcher.

The Gaussian nature of the beam can also be verified by considering the evolution of the wave profile with distance. Figure 5-14 shows the beam intensity contours on a plane located 60 cm from the window aperture. The field is Gaussian with a waist size of 3.9 cm in both x and z; the theoretical waist size (assuming a minimum waist at the window of 1.6 cm) is 3.6 cm. This 0.3 cm divergence in beam size over the 60 cm (220λ) propagation distance is practically negligible, and we see that the measured beam behaves as a nearly-ideal Gaussian beam.

We have shown explicitly, using the measured field intensities, that the output beam is a well-formed Gaussian with parameters close to those of the design. We

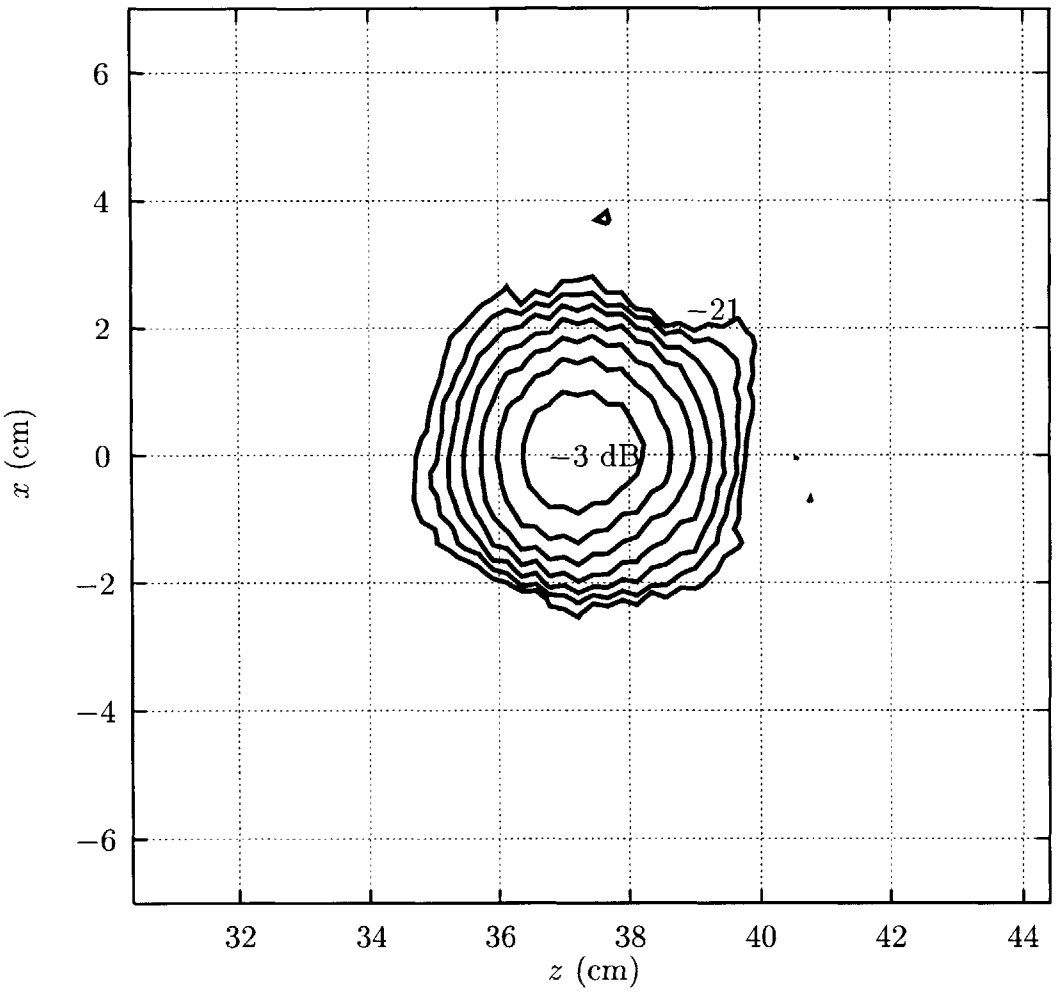

Figure 5-12: Measured field intensity on the window plane. The window center is at $z = 37.4$ cm, $x = 0$ cm. Contours of constant $|E_x|^2$ are at 3 dB intervals from peak; the -3 dB and -21 dB curves are labeled.

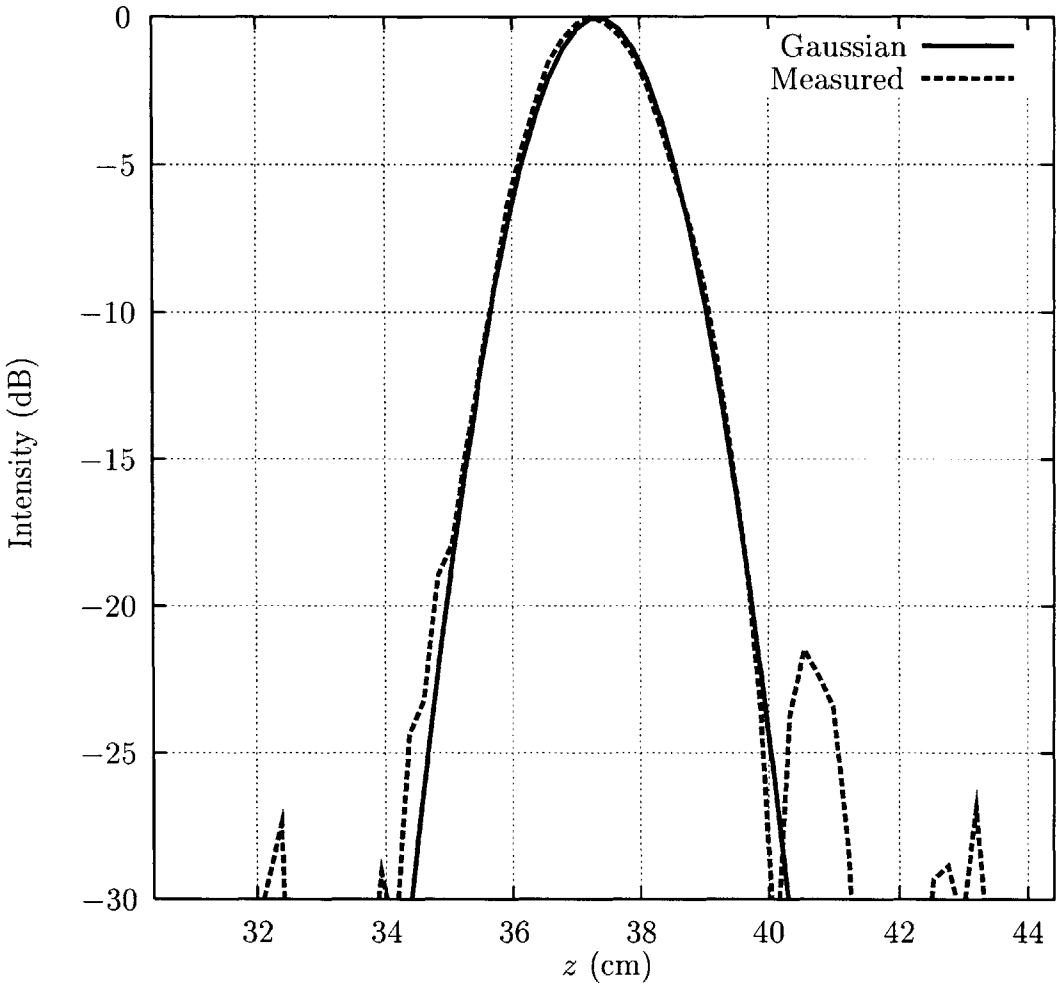

Figure 5-13: Gaussian beam with a z-waist of 1.6 cm (solid) and measured beam (dashed) intensity along the z-axis of the window plane. The window center is at $z = 37.4$ cm.

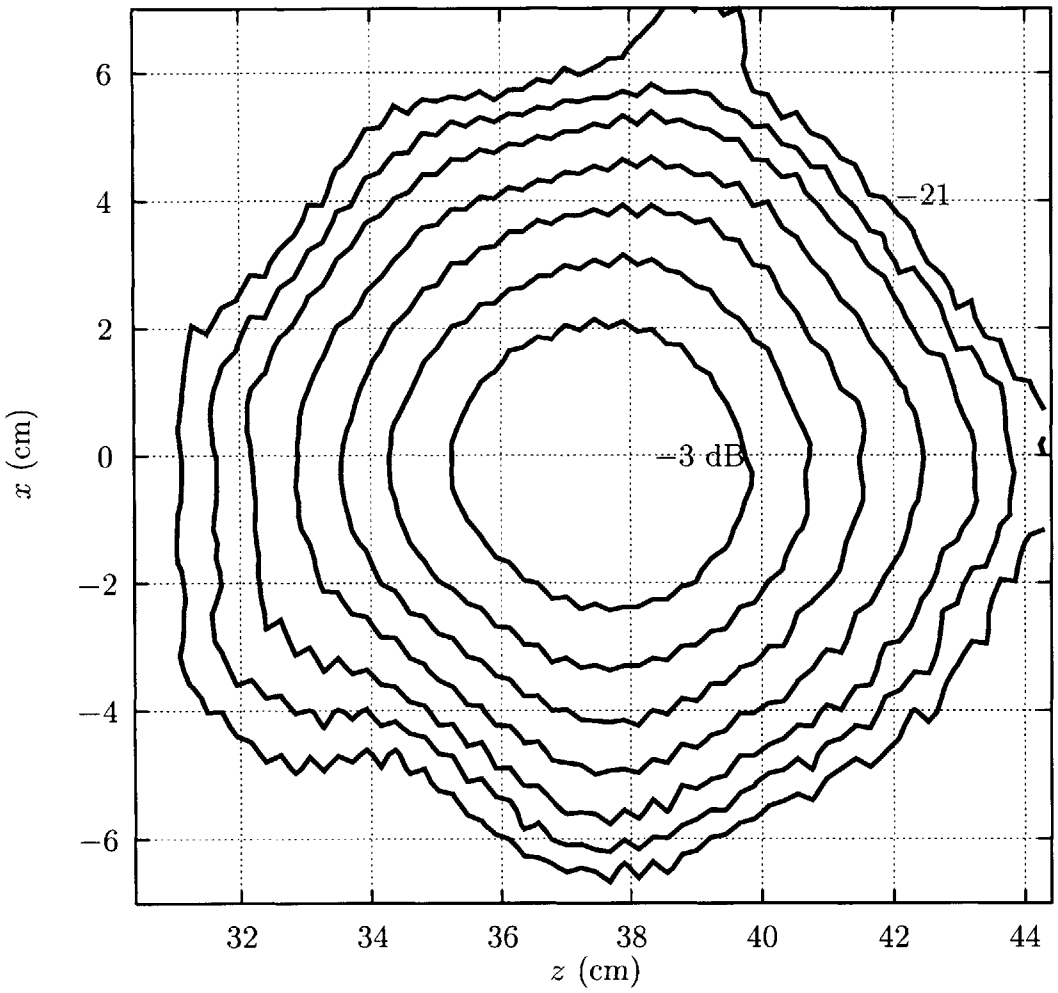

Figure 5-14: Measured field intensity 60 cm from the window plane. Contours of constant $|E_x|^2$ are at 3 dB intervals from peak; the -3 dB and -21 dB curves are labeled.

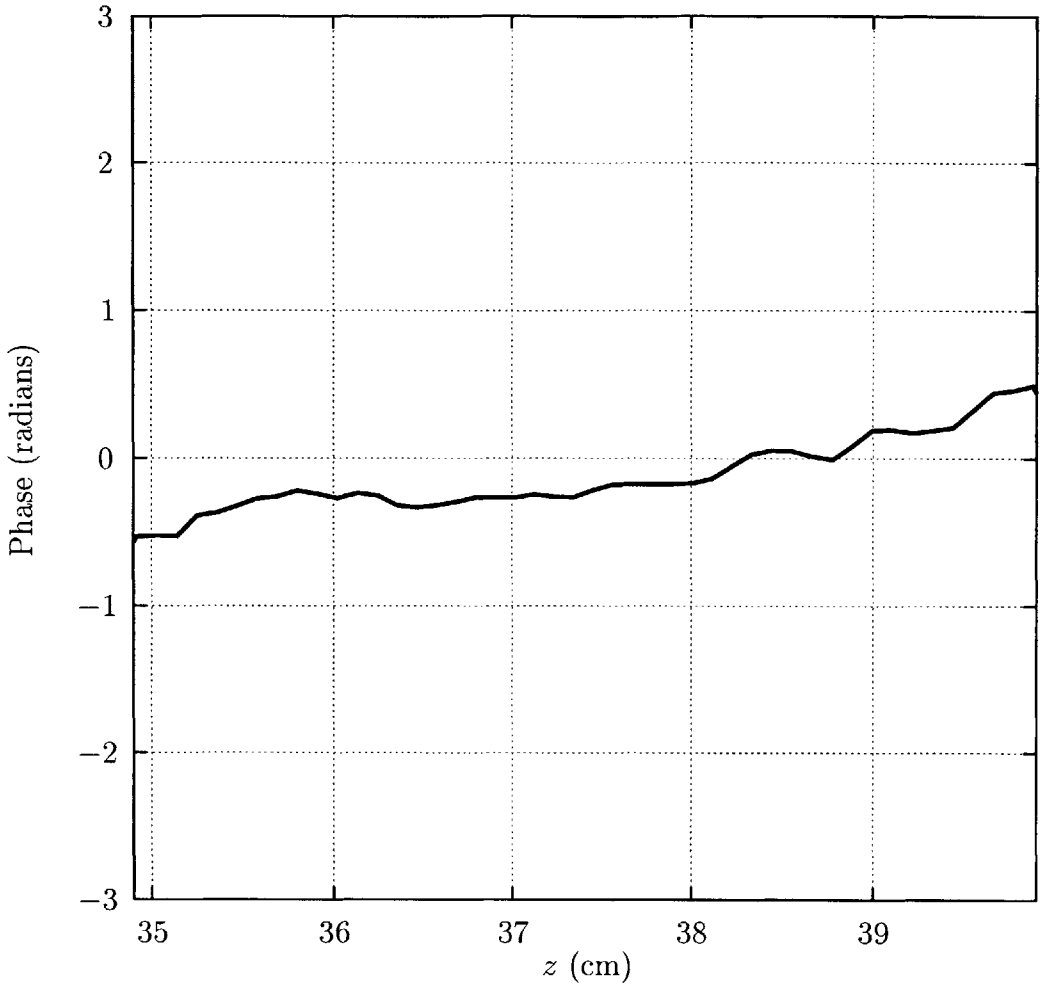

Figure 5-15: Reconstructed phase of the measured beam over the window aperture along the z-axis.

can extend the data analysis by employing the phase retrieval algorithm to round out the study. With input field intensities on planes located 10 cm before, at, and 40 cm beyond the window position in y, we retrieved the phase over the window aperture, and this phase is shown in Figure 5-15 along the z-axis. Since the design Gaussian beam has its minimum waist at the window, we expect the phase there to be flat. This is indeed the case for the reconstructed output field phase of Figure 5-15. The mild slope in the phase arises because the beam is propagating at an angle of 0.2° in the $y - z$ plane, which leads to a small beam-center offset in z (see Figure 5-14).

5.6 Experimental Results — Hot Tests

The complete mode converter was assembled and placed inside the gyrotron for hot, or high-power, testing with the diamond window. The first series of experiments were performed at CPI to determine the characteristics of the diamond window. The gyrotron tube was operated at 650 kW for 1.6 s pulse lengths and at 940 kW for 0.001 s pulse lengths with an average power of 50 kW. The diamond window performed well throughout the testing, indicating that the microwave beam is well-matched to the window aperture.

The gyrotron was next installed at General Atomics and infrared camera measurements of the output beam were performed as described in Chapter 4. Figure 5-16 shows intensity contours of an IR camera measurement 15.8 cm from the window. As we anticipate from the cold-test measurements, the gyrotron beam is a well-formed Gaussian with a slight ellipticity of about 5%. The beam continues to evolve with Gaussian behavior, as indicated in Figure 5-17, which shows the field intensity contours at 66.8 cm from the window. Figure 5-18 compares the waist expansion of this measured gyrotron beam to that of an ideal Gaussian beam. We see that for distances exceeding a meter, the beam maintains a good Gaussian profile with a waist expansion that closely matches the ideal. Based on these measurements and analysis of the cold test measurements, we can conclude that the shaped mirrors accurately transform the field pattern in the mode converter to the desired pattern on the output window.

5.7 Discussion

We have presented in this chapter a comprehensive analysis, design, and experimental study of a quasi-optical, internal mode converter for a high-power gyrotron. The required field radiated by the mode converter was tightly-constrained by the diamond window, whose thermal properties and edge-cooled configuration leave small margin for error in the power profile of the beam.

We initiated the design by measuring the electric field profile over several consecutive planes following the second mirror. The measurements were performed at low power with a heterodyne receiver that offered higher precision and much better dynamic range than the infrared camera reported in Chapter 4. Additionally, all of the data from this measurement set were useful, in contrast to the infrared camera measurements in the previous chapter, most of which suffered corruption from heat

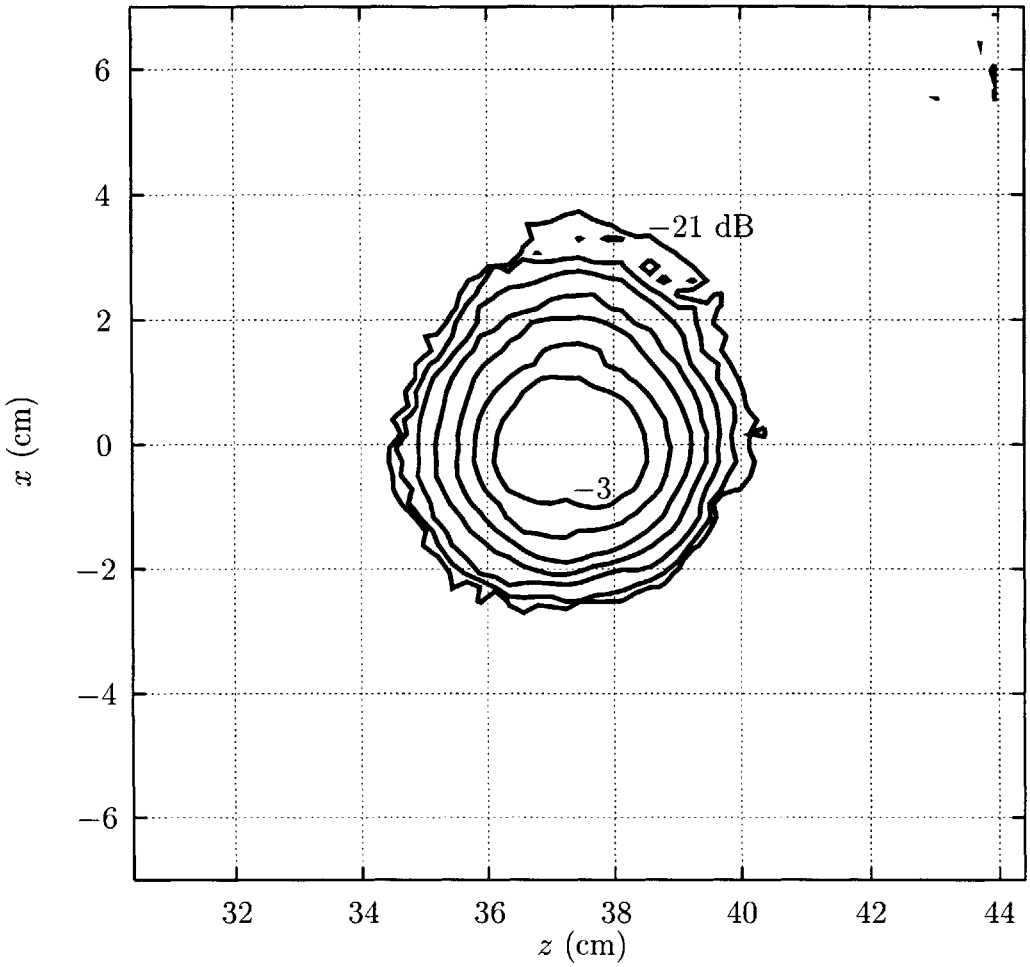

Figure 5-16: Infrared camera measurement of the S/N3 gyrotron output beam at a distance of 15.8 cm from the diamond window. Contours of constant $|E_x|^2$ are at 3 dB intervals from peak; the −3 dB and −21 dB curves are labeled.

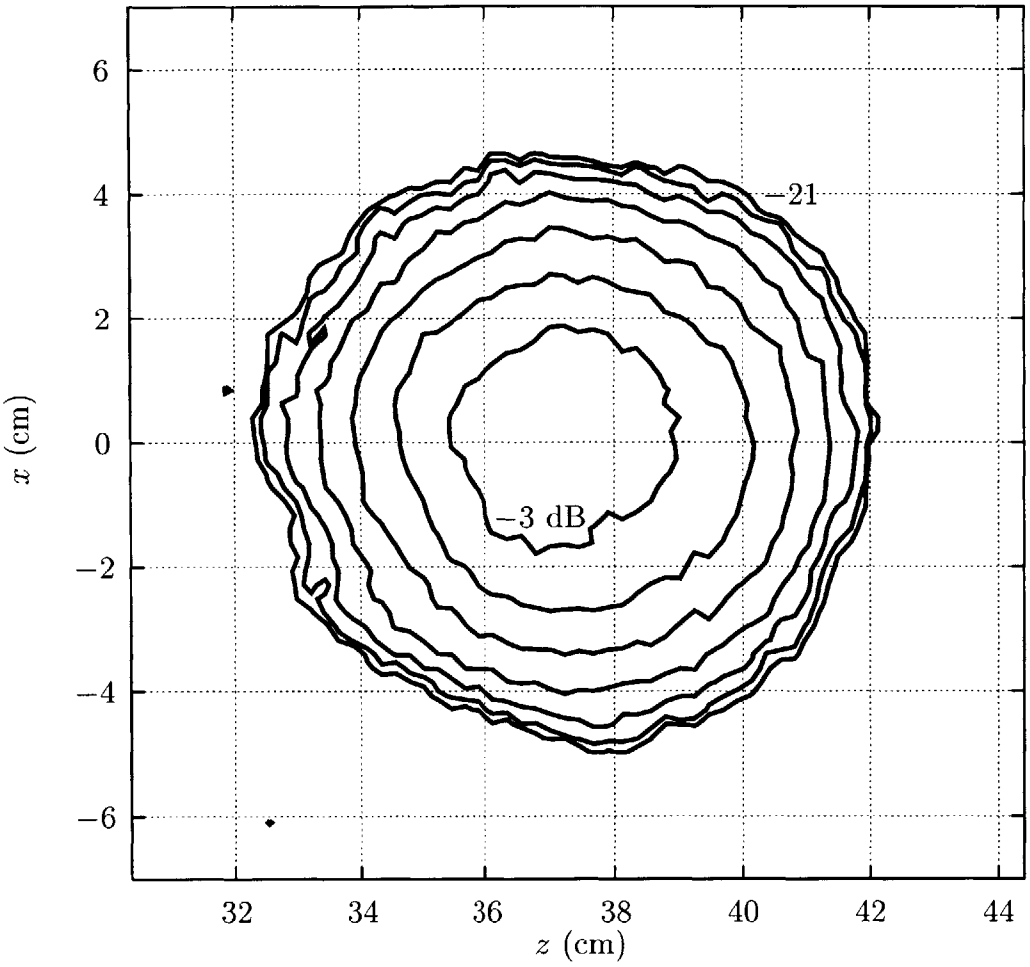

Figure 5-17: Infrared camera measurement of the S/N3 gyrotron output beam at a distance of 66.8 cm from the diamond window. Contours of constant $|E_x|^2$ are at 3 dB intervals from peak; the −3 dB and −21 dB curves are labeled.

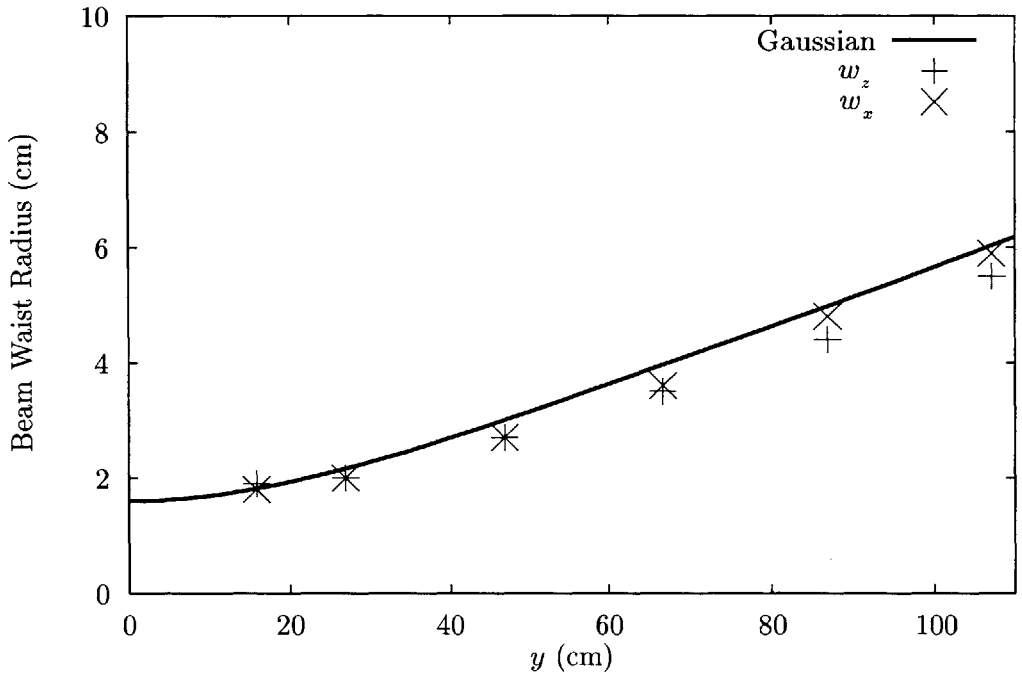

Figure 5-18: Expansion of the S/N3 gyrotron output beam along the direction of propagation (y in the mode converter coordinate system; see Figure 1-3) in cm from the gyrotron window. The solid line is an ideal Gaussian beam with $w_0 = 1.6$ cm at $y = 0$. Infrared camera measurements of the beam give the waist radius in x ($\times$) and z (+).

rising on the target. Given these factors, we expected to produce a better result for this internal mode converter experiment.

The phase of the wave was retrieved from intensity measurements over three planes using a phase retrieval geometry similar to that described in the mode converter example of Section 2.4.4. In this case, however, we discovered the expediency of orienting the measurement planes, via a simple coordinate transformation in one dimension, such that the beam is propagating perpendicularly to the planes. This approach allows the phase retrieval algorithm to find the nominal phase structure of the wave without the burden of an additional phase tilt. Adding the phase tilt after the field reconstruction proved valid; propagating the tilted wave to a measurement plane showed good agreement between the reconstructed intensity and measured intensity.

This reconstructed field was used to analyze the original mode converter configuration that was designed to produce a uniform power profile over a 10-cm-aperture window. The final simulated field on the window had a crescent-shaped non-uniformity that resembles the profile observed in measurements. This result reveals that the launcher and first two mirrors are the primary source of disagreement between theory and experiment, and it indicates that our proposed design approach for correcting the fields after the second mirror should fully account for the actual fields in the mode converter.

A pair of phase-correcting mirrors were shaped according to the procedure developed in Chapter 3 to transform the fields after the second mode converter mirror into an ideal Gaussian beam with a minimum waist radius of 1.52 cm that occurs at the 5-cm-aperture diamond window. These mirrors were simulated with a physical optics code (see Section 2.4.4), which confirmed that the final radiated wave is indeed a Gaussian beam with the desired specifications. In the process of verifying the design, we discovered the importance of shaping the mirrors with the physical dimensions of the mirrors in mind. In doing so, we essentially account for power that exists on the measurement plane but does not intercept the actual mirror surface. Hence, we avoid sidelobe formation that arises from the inherent windowing function of the finite-sized mirror aperture.

The mirror surface profiles were machined in solid copper, and the mirrors were mounted on the mode converter external to the tube for cold test measurements of the radiation pattern. The measured electric field patterns at the window aperture plane and at following planes show that the radiated beam is strongly Gaussian, with a waist size in z (the gyrotron axis) of 1.6 cm and a waist in x of 1.7 cm. These waist sizes are slightly larger than the design specification of 1.52 cm, but even for

the larger dimension, the error amounts to only 0.66λ, and integrating the power over the aperture shows that 98.5% of the beam power propagates through the window. Additionally, the beam is centered on the window, and this beam position property is at least as critical to efficient beam transmission as beam waist size.

Other characteristics of the radiated beam were also examined, including expansion of the beam beyond the window and the phase of the beam. These parameters confirmed the nearly-ideal Gaussian behavior of the wave. Furthermore, the mode converter was placed inside the gyrotron for high-power operation, and infrared camera measurements of the field intensity were made that show the beam evolves as a Gaussian beam. These results represent the first successful application of mirror shaping based on measured field intensity to the design of gyrotron internal mode converters.

Chapter 6

Conclusion

6.1 Summary

This work has presented the systematic development of a new approach to gyrotron mode converter mirror design based on intensity-only measurements. The method uses an iterative phase retrieval algorithm to reconstruct the full field structure of a wave from a given set of intensity measurements. A mirror shaping routine, also derived from the phase retrieval algorithm, then provides a pair of phase-correcting surfaces to transform the reconstructed incident wave into a desired radiated wave.

We formulated an iterative algorithm that retrieves the phase given intensity measurements on two or more arbitrary measurement planes. We also gave a proof of convergence for the algorithm in the case of measurements planes in the object and Fourier domains. This proof provides insight into the fundamental principal of the algorithm; namely, that at each iteration, substituting the measured amplitudes for the computed values amounts to weighting the solution at each pass of the algorithm to draw the computed amplitudes closer to the measured amplitudes. We explored this weighting concept within the context of our particular choice of using a plane wave expansion to represent the fields, and argued that the algorithm will attempt to find a solution that is as close to the measured values as possible while still being physically meaningful. The plane wave expansion also allows us to write the plane-to-plane propagation operator in terms of Fourier transforms or, in the case of discretely-sampled data, the Fast Fourier transform. Using a numerical implementation of the phase retrieval algorithm based on the FFT, we reconstructed a Gaussian beam for several illustrative examples and showed that the algorithm could reproduce the Gaussian beam amplitude and phase to high accuracy. We also demonstrated with numerical examples that the rapid computation afforded by the FFT is invaluable for

performing an accurate reconstruction of a wave, which may take several hundred iterations.

The phase retrieval algorithm was then extended to the problem of shaping a pair of phase-correcting surfaces that transform an incident wave into a desired radiated wave. We utilized the phase retrieval approach to form a set of self-consistent phases that connect the incident and radiated amplitudes, then we defined our phase correcting surfaces to match the incident and radiated phases with their respective self-consistent phases. This phase corrector approximation holds for surfaces on which the wave amplitude and polarization is not strongly influenced by the surface; this approximation holds for the current quasi-Gaussian beams of interest. The third and fourth mirrors in a four-mirror gyrotron internal mode converter were shaped based on simulated incident fields using the proposed design approach to produce a 1.5 cm waist Gaussian beam at the gyrotron window. The mirror profiles were simulated in a physical optics code that demonstrated the validity of the design. The computed output field is a Gaussian beam in both amplitude and phase that shows excellent agreement with the specified output field. This encouraging result demonstrates that, for our quasi-optical applications, shaping the mirrors as phase-correctors via the phase retrieval algorithm is a very effective method for mirror design.

The mirror design approach based on phase retrieval from intensity measurements was first applied to shaping mirrors for a gyrotron matching optics unit, which transforms the gyrotron microwave beam into a Gaussian beam for injection into a corrugated waveguide. The intensity profile of the gyrotron beam has a nonuniform, crescent shaped pattern (Figure 1-7) that evolves as the superposition of a dominant Gaussian beam and another apparent beamlet. The mirror surfaces direct the beamlet into the main beam, and infrared camera measurements of the MOU output show that the beam is nearly Gaussian in the vicinity of the waveguide aperture. The beam waist appears to occur 10 cm beyond the design position; this result is most likely caused by phase error in the reconstruction due to corrupted measured intensity. In spite of the measurement limitations, the mirrors focus 94.5% of the beam power into the waveguide aperture, and at the ture position of the beam waist minimum 96.5% of the beam power is directed into the waveguide.

The next application of our mirror design approach involved shaping the surface profiles of the last two mirrors in a four-mirror gyrotron internal mode converter. The pair of shaped mirrors were required to transform the incident field radiated from the second mirror in the mode converter into a Gaussian beam on the gyrotron window. The Gaussian beam waist size at the window was specified to be 1.52 cm, which

ideally allows 99.6% of the beam power to pass through the 5 cm clear aperture of the edge-cooled diamond window. The launcher and first two mirrors from the mode converter were mounted external to the gyrotron and intensity measurements of the field radiated by the second mirror were made over several consecutive planes. These intensity patterns were then used in the phase retrieval algorithm to reconstruct the field incident on the first shaped mirror. As an aside, we used this reconstructed wave to analyze the original mode converter mirrors in an effort to understand the source of the differences between the computed and measured window fields. We found that the primary cause of the observed discrepancy is in fact the field following the second mirror.

A pair of phase-correcting mirrors were then shaped to transform the reconstructed field after the second mirror into the specified Gaussian beam on the gyrotron diamond window. Simulation of the mirrors in the independent physical optics code showed they produce the desired Gaussian beam profile at the window plane. The mirrors were machined into solid copper and mounted on the mode converter external to the tube for low power measurements of the radiated field. The mirrors produced a high-quality Gaussian beam with a waist along the tube axis of 1.6 cm and a transverse waist of 1.7 cm. Integrating the power in the beam over the 5 cm clear aperture of the diamond window showed that 98.5% of the power is transmitted through the aperture. Additional measurements of the beam beyond the window plane along with phase retrieval confirmed the strong Gaussian nature of the wave and verified that the waist of the beam occurs at the window, as specified in the design parameters. The mode converter was then placed inside a 1 MW gyrotron, and infrared camera measurements of the output beam were made. These intensity patterns agree with the cold test measurements, demonstrating that our mirror design approach provides the accurate and precise transformation of the gyrotron electromagnetic radiation required for efficient high-power operation.

6.2 Future Work

The design method described and validated in this thesis continues to evolve both in technique and applications.

As a purely mechanics aspect, we can improve some of the post-processing routines needed to define the mirror surfaces. The phase unwrapping algorithm mentioned in Section 3.2, while applicable to our reasonably-smooth phase functions, fails for more complicated phase structure. A modification of the current phase-tracing approach or

a different algorithm, such as a polynomial approximation, may lead to better phase unwrapping. In some cases, the final physical mirror surfaces need to be smoothed (in contrast to our surfaces that required smoothing only around the unimportant edges). A two-dimensional curve fit or filtering in terms of spatial Fourier components could be used to smooth the metallic surfaces. We are currently developing alternative approaches to phase unwrapping and surface smoothing.

Our original mirror design proposal included steps for shaping the first two mirrors in a four-mirror internal mode converter based on analytic fits to measured intensity. Both the MOU and internal mode converter studies presented in this thesis did not include these steps; each design began immediately at the phase retrieval/mirror shaping stage. An important addition to the current body of work is a full mode converter design with the first two mirror shapes optimized to the measured (rather than computed) launcher fields.

The 170 GHz gyrotron at MIT is one such project, where the actual field radiated by the launcher is substantially different from the theoretically-predicted field [27]. Also, the 170 GHz frequency is 50% larger than the frequency we have dealt with in the reported experiments, and the higher frequency represents a sampling challenge to both our measurement equipment and computing resources. For this mode converter, the first mirror has been designed according to our proposed method using a Gaussian fit to measurements of the launcher field. Further measurements of the mode converter field and design of the remaining mirrors is an ongoing effort.

MIT is also collaborating with the electron cyclotron heating group of Japan's Large Helical Device (LHD). Their 84 GHz gyrotrons use a Vlasov launcher and a pair of focusing mirrors to direct the microwave power out of the gyrotron. The radiated wave has a more complicated field structure than the beams we have discussed in this thesis, and the configuration of the microwave transmission system requires large incidence angles on the matching optics unit mirrors. Such beam behavior requires very accurate measurements and may violate some of the approximations we have made in defining our mirrors as strictly phase-correcting surfaces. Novel mirror design methods rooted in our basic procedure are being investigated to account for these effects [28].

We have also explored the possibility of using our fast phase retrieval/mirror synthesis algorithm for real-time reflector compensation in the Haystack radio telescope operating at millimeter wavelengths [29]. A deformable sub-reflector, whose surface is controled by a set of actuators, could compensate for gravitational and thermal deformations of the main reflector, providing improved resolution [30, 31].

Bibliography

[1] S. N. Vlasov, L. I. Zagryadskaya, and M. I. Petelin, "Transformation of a whispering gallery mode, propagating in a circular waveguide, into a beam of waves," *Radio Engineering and Electronic Physics*, vol. 12, no. 10, pp. 14 – 17, 1975.

[2] M. Abramowitz and I. A. Stegun, eds., *Handbook of Mathematical Functions with Formuals, Graphs, and Mathematical Tables.* New York: Dover Publications, 1965.

[3] G. G. Denisov, A. N. Kuftin, V. I. Malygin, N. P. Venediktov, D. V. Vinogradov, and V. E. Zapevalov, "110 GHz gyrotron with built-in high-efficiency converter," *International Journal of Electronics*, vol. 72, no. 5 and 6, pp. 1079–1091, 1992.

[4] M. Blank, K. Kreischer, and R. J. Temkin, "Theoretical and experimental investigation of a quasi-optical mode converter for a 110-GHz gyrotron," *IEEE Transactions on Plasma Science*, vol. 24, no. 3, pp. 1058–1066, 1996.

[5] H. A. Haus, *Waves and Fields in Optoelectronics.* Englewood Cliffs, NJ: Prentice-Hall, 1984.

[6] J. A. Lorbeck and R. J. Vernon, "A shaped-reflector high-power converter for a whispering-gallery mode gyrotron output," *IEEE Transactions on Antennas and Propagation*, vol. 43, pp. 1383 – 1388, Dec. 1995.

[7] K. Felch, M. Blank, P. Borchard, T. S. Chu, J. Feinstein, H. R. Jory, J. A. Lorbeck, C. M. Loring, Y. M. Mizuhara, J. M. Neilson, R. Schumacher, and R. J. Temkin, "Long-pulse and CW tests of a 110-GHz gyrotron with an internal, quasi-optical mode converter," *IEEE Transactions on Plasma Science*, vol. 24, no. 3, pp. 558–569, 1996.

[8] D. R. Denison, T. Kimura, M. A. Shapiro, and R. J. Temkin, "Phase retrieval from gyrotron near-field intensity measurements," in *Conference Digest – Twenty-second International Conference on Infrared and Millimeter Waves*, pp. 81 – 82, 1997.

[9] D. R. Denison, M. A. Shapiro, and R. J. Temkin, "Reflector antenna shaping from feed field intensity measurements," in *Conference Digest – USNC/URSI National Radio Science Meeting*, p. 258, 1998.

[10] P. C. Clemmow, *The Plane Wave Spectrum Representation of Electromagnetic Fields.* Oxford: Pergamon Press, 1966.

[11] J. A. Kong, *Electromagnetic Wave Theory.* New York: Wiley Interscience, second ed., 1990.

[12] J. C. G. Lesurf, ed., *Selected Papers on Gaussian Beam Mode Optics for Millimeter-Wave and Terahertz Systems.* Bellingham, WA: SPIE Optical Engineering Press, 1993.

[13] B. Z. Katsenelenbaum and V. V. Semenov, "Synthesis of phase correctors shaping a specified field," *Radio Engineering and Electronic Physics*, vol. 12, pp. 223 – 230, 1967.

[14] R. W. Gerchberg and W. O. Saxton, "A practical algorithm for the determination of phase from image and diffraction plane pictures," *Optik*, vol. 35, no. 2, pp. 237 – 246, 1972.

[15] A. P. Anderson and S. Sali, "New possibilities for phaseless microwave diagnostics. Part 1: Error reduction techniques," *IEE Proceedings*, vol. 132, Pt. H, pp. 291 – 298, Aug. 1985.

[16] J. R. Fienup, "Phase retrieval algorithms: A comparison," *Applied Optics*, vol. 21, no. 15, pp. 2758 – 2769, 1982.

[17] A. V. Oppenheim and R. W. Schafer, *Discrete-Time Signal Processing.* Englewood Cliffs, NJ: Prentice Hall, 1989.

[18] W. H. Press, S. A. Teukolsky, W. T. Vetterling, and B. P. Flannery, *Numerical Recipes in Fortran: The Art of Scientific Computing.* New York: Cambridge University Press, second ed., 1992.

[19] B. Y. Kinber, "On two-reflector antennas," *Radio Engineering and Electronic Physics*, vol. 6, pp. 914 – 921, June 1962.

[20] V. Galindo, "Design of dual-reflector antennas with arbitrary phase and amplitude distributions," *IEEE Transactions on Antennas and Propagation*, vol. AP-12, pp. 403 – 408, July 1964.

[21] V. Galindo-Israel, R. Mittra, and A. G. Cha, "Aperture amplitude and phase control of offset dual reflectors," *IEEE Transactions on Antennas and Propagation*, vol. AP-27, Mar. 1979.

[22] A. A. Bogdashov, A. V. Chirkov, G. G. Denisov, D. V. Vinogradov, A. N. Kuftin, V. I. Malygin, and V. E. Zapevalov, "Mirror synthesis for gyrotron quasi-optical mode converters," *International Journal of Infrared and Millimeter Waves*, vol. 16, no. 4, pp. 735 – 744, 1995.

[23] G. G. Denisov, A. V. Chirkov, D. V. Vinogradov, V. I. Malygin, A. A. Bogdashov, V. I. Belousov, N. L. Alexandrov, and V. E. Zapevalov, "Phase corrector synthesis and field measurements for gyrotron quasi-optical wave beams," in *Conference Digest – Twentieth International Conference on Infrared and Millimeter Waves*, pp. 483 – 484, 1995.

[24] Y. Hirata, Y. Mitsunaka, K. Hayashi, and Y. Itoh, "Wave-beam shaping using multiple phase-correction mirrors," *IEEE Transactions on Microwave Theory and Techniques*, vol. 45, pp. 72 – 77, Jan. 1997.

[25] L. Rebuffi and J. P. Crenn, "Radiation patterns of the HE_{11} mode and gaussian approximations," *International Journal of Infrared and Millimeter Waves*, vol. 10, no. 3, pp. 291 – 311, 1989.

[26] C. P. Moeller, "A coupled cavity whispering gallery mode transducer," in *Conference Digest – Seventeenth International Conference on Infrared and Millimeter Waves*, pp. 42 – 43, 1992.

[27] T. Kimura, *Experimental Study of a 1 MW, 170 GHz Gyrotron Oscillator.* PhD thesis, Massachusetts Institute of Technology, 1997.

[28] M. A. Shapiro, D. R. Denison, and R. J. Temkin, "Mirror corrector shaping for 84 GHz gyrotron used at LHD," in *To appear: Conference Digest – Twenty-fourth International Conference on Infrared and Millimeter Waves*, 1999.

[29] R. P. Ingalls *et al.*, "Upgrading the Haystack radio telescope for operation at 115 GHz," *Proceedings of the IEEE*, vol. 82, pp. 742 – 754, May 1994.

[30] J. Antebi *et al.*, "A deformable subreflector for the Haystack radio telescope," *IEEE Antennas and Propagation Magazine*, vol. 36, pp. 19 – 27, June 1994.

[31] A. Greve, J. W. M. Baars, J. Peñalver, and B. LeFloch, "Near-focus active optics: An inexpensive method to improve millimeter-wavelength radio telescopes," *Radio Science*, vol. 31, no. 5, pp. 1053 – 1065, 1996.